NOTICE

The quality of this microfiche is heavily dependent upon the quality of the original thesis submitted for microfilming. Every effort has been made to ensure the highest quality of reproduction possible.

If pages are missing, contact the university which granted the degree.

Some pages may have indistinct print especially if the original pages were typed with a poor typewriter ribbon or if the university sent us a poor photocopy.

Previously copyrighted materials (journal articles, published tests, etc.) are not filmed.

Reproduction in full or in part of this film is governed by the Canadian Copyright Act, R.S.C. 1970, c. C-30. Please read the authorization forms which accompany this thesis.

THIS DISSERTATION
HAS BEEN MICROFILMED
EXACTLY AS RECEIVED

AVIS

La qualité de cette microfiche dépend grandement de la qualité de la thèse soumise au microfilmage. Nous avons tout fait pour assurer une qualité supérieure de reproduction.

S'il manque des pages, veuillez communiquer avec l'université qui a conféré le grade.

La qualité d'impression de certaines pages peut laisser à désirer, surtout si les pages originales ont été dactylographiées à l'aide d'un ruban usé ou si l'université nous a fait parvenir une photocopie de mauvaise qualité.

Les documents qui font déjà l'objet d'un droit d'auteur (articles de revue, examens publiés, etc.) ne sont pas microfilmés.

La reproduction, même partielle, de ce microfilm est soumise à la Loi canadienne sur le droit d'auteur, SRC 1970, c. C-30. Veuillez prendre connaissance des formules d'autorisation qui accompagnent cette thèse.

LA THÈSE A ÉTÉ
MICROFILMÉE TELLE QUE
NOUS L'AVONS REÇUE

UNIVERSITÉ D'OTTAWA
UNIVERSITY OF OTTAWA

DETERMINATION AND ANALYSIS OF THE $^{53}Cr^{3+}$ FINE AND HYPERFINE STRUCTURE PARAMETERS IN HYDRATED CRYSTALS FROM ELECTRON SPIN RESONANCE STUDIES

by

André Leclerc

A thesis submitted to the School of Graduate Studies in partial fulfilment of the requirements for the degree of Ph.D. in Physics

UNIVERSITY OF OTTAWA
OTTAWA, CANADA, 1976

Patri matrique.

ACKNOWLEDGMENTS

The author wishes to thank Dr. A. Manoogian for his guidance and collaboration in the course of this work. The author is also gratefull to Mr. Bei Wah Chan whose dexterous operation of the spectrometer was appreciated. Thanks are also due to the Ontario Government for financial assistance received during the course of this work.

STATEMENT OF ORIGINALITY

The following is a list of the work done in the course of this study which, to the best of the author's knowledge, has not been done previously.

1) Electron spin resonance of Cr^{3+} doped in TlGa and CsIn sulfate alums and in CsAl and CsGa selenate alums.

2) Electron-nuclear double resonance of $^{53}Cr^{3+}$ doped in TlGa and CsIn sulfate alums, in CsAl and CsGa selenate alums, and in the guanidinium salts GAlSH, GGaSH, GAlSeH and GGaSeH.

3) Classification of the alums, the guanidinium salts, and $AlCl_3.6H_2O$ according to their magnetic behavior, as determined in the resonance studies.

4) Separation of the fine and hyperfine structure parameters D,Q', A and B into their component parts due to crystal vibration and static distortion effects.

5) Measurement of the chromium Fermi contact term K' in the hydrated crystals.

6) Presentation of a model to explain the mechanism of the phase transitions which occur in many of the crystals.

ABSTRACT

Electron spin resonance (ESR) and electron-nuclear double resonance (ENDOR) measurements were carried out on trivalent chronium impurities doped in alums and guanidinium crystals. ESR was performed on the even and odd isotopes of chromium, while the odd isotope $^{53}Cr^{3+}$ enriched to 94% was used in the ENDOR studies. All the crystals were grown by slow evaporation of saturated solutions containing the particular salts. The chromium doped crystals were clear and contained no more than an estimated 0.01 wt% of Cr^{3+} impurities. Some ESR measurements were also done on concentrated chrome alums, in which case all the trivalent ions in the crystal were of chromium. All the magnetic resonance was done at X-band microwave frequencies ($\sim$ 9.4 GHz).

The common feature of all the crystals studied is that they contain trigonally distorted $Cr^{3+}.6H_2O$ magnetic complexes. By extending the measurements of the chromium fine and hyperfine structure parameters in such systems it is possible to obtain a picture of their general behavior. This is important if a successful analysis of the results is to be obtained. From the ESR measurements of the spin Hamiltonian zero-field splitting parameter D as a function of temperature, it is seen how the magnetic complexes in the various crystals are grouped into families. Individual families of magnetic behavior are obtained for

the Rb, Cs, Tl, NH_4 and K sulfate alums, the Cs selenate alums, and the guanidinium sulfate and selenate salts.

The ENDOR studies allow precise measurements to be made of the chromium spin Hamiltonian hyperfine structure parameters A, B, Q' and g_n'. Plots of A, B and Q' versus D for the various magnetic complexes, all measured at 4.2 K, produce graphs which exhibit laws of physical behavior for the crystals. These graphs are used as a starting point for the analysis of the data. A model is then presented for splitting the parameters D, Q', A and B into their constituent parts due to the effect of crystal static distortion and vibration, and the procedure is applied to all the trigonally distorted $Cr^{3+}.6H_2O$ magnetic complexes studied up until now. The analysis procedure allows the temperature dependence of the A, B and Q' parameters to be predicted. The chromium Fermi contact term in the hydrated crystals is also determined. An interesting feature of the split D vs. T curves is that the individual families of magnetic behavior are shown to be all related to each other in a particular way.

The splitting procedure is then used to obtain an explanation for the phase transitions occuring in the various salts. These occur at low temperature in the NH_4 and K alums, and at high temperature in the guanidinium salts. In particular, it is shown that the NH_4 and K chromic alums undergo phase transitions when the static trigonal distortion at the $Cr^{3+}.6H_2O$ magnetic sites changes sign. A similar effect is operative in the lightly doped crystals, but in these cases the octahedrally coordinated host trivalent ion likely plays the central role in the occurrence of the phase transitions.

TABLE OF CONTENT

page

page

LIST OF FIGURES

page

page

page

page

LIST OF TABLES

page

page

CHAPTER 1

INTRODUCTION

Electron-nuclear double resonance (ENDOR) measurements of $^{53}Cr^{3+}$ in hydrated crystals have been done previously by others in this laboratory on a few isolated salts, and the results for CsGa and RbGa sulfate alums, CsAl and RbAl sulfate alums, and $AlCl_3.6H_2O$ have been published.[1,2,3] The published results indicated a complexity of behavior that could not be explained from the limited data. It became apparent that more ENDOR measurements on similar such systems were necessary so that a general trend of behavior for trigonally distorted $Cr^{3+}.6H_2O$ magnetic complexes could be obtained. Moreover, in the course of the work it appeared that a key to the various magnetic behaviors lies in the plots of the D vs T curves, i.e., the temperature dependence of the chromium zero-field splitting parameter D. This parameter is measured using ordinary electron spin resonance (ESR), and such D vs T plots were obtained in the present work for all the $Cr^{3+}.6H_2O$ magnetic complexes considered. The ENDOR measurements were extended to the TlGa and CsIn sulfate alums, the CsAl and CsGa selenate alums, and the four isomorphic guanidinium salts, termed GAlSH, GGaSH, GAlSeH and GGaSeH.

No ENDOR work has been done previously on the chromium doped guanidinium salts.

Each alum crystal contains four non-equivalent, but otherwise identical, trigonally distorted chromium magnetic complexes, while each guanidinium crystal contains two different ones. Hence two sets of data are obtained from each guanidinium crystal, as against one for each alum. Alums have a special importance in this work because the $Cr^{3+}.6H_2O$ magnetic complexes in some of them are trigonally compressed, while in others they are trigonally extended. The results for the guanidinium salts are important because these crystals have in general a much larger zero-field splitting parameter D than do the alums. The results for $AlCl_3.6H_2O$ are important because this crystal has the smallest D value of the hydrated crystals considered. Hence resonance data obtained in all three types of crystal systems covers nearly the whole range of possible D values. Such a situation is required if a satisfactory analysis of the data is to be obtained.

Since the introduction of the spin Hamiltonian, it has generally been accepted that both crystal vibration and static distortion effects are involved in the make-up of the Hamiltonian parameters, but in practice only the static effect is considered most of the time. Some attempts have been made in the past to include the effect of crystal vibrations. Holms and McClure[4] studied the optical spectra of transition metal ions in hydrated crystals and showed the importance of crystal vibrations in

determining the transition strength of the spectral lines. They made measurements of band intensity as a function of temperature and plotted the corresponding integrated intensities. The temperature dependence of the integrated intensity suggested that a vibrational perturbation was responsible for the mechanism of the transition. Their intensity curves were then fitted to the oscillator strength function $f = f_o[1+ \exp(-\theta/T)]$, where f_o is the value of f at 0 K. In the case of Cr sulfate alum a reasonable fit was obtained with θ = 400 K.

Carlin and Walker[5] studied the optical spectra of Cr^{3+} in GAlSH and its isomorphs, in $AlCl_3.6H_2O$ and in NH_4Cr alum. Following Ballhausen[6], they fitted the temperature dependence of the integrated band intensities to an oscillator strength function of the form $f = f_o \coth(\theta/2T)$. A value of θ = 500 K was found for the $^4T_2$ band and 650 K for the $^4T_1$ band of chromium in GAlSH. A value of θ = 500 K was also found for the $^4T_2$ band of NH_4Cr alum, which is larger than the value of 400 K found by Holmes and McClure in their analysis of KCr alum.

Walsh[7] performed stress measurements on nickel fluosilicate crystals and observed the change in the zero-field splitting parameter D for Ni^{2+} by employing electron spin resonance. In the analysis of the results it was assumed that the contributions to the D parameter are due to the static distortion of the ligand atoms surrounding the Ni^{2+} ion, and the vibrational mechanism of the crystal. A plot of D vs T for Ni^{2+} measured at atmospheric pressure using ESR was an integral part of

the discussion. The functional form describing the lattice vibrational contribution to D was taken to be that of a system of Planck oscillators. The net measured D value at a given temperature was then taken to be a sum of the static and vibrational parts. Walsh attempted to fit his experimental results only in the high temperature region (200 - 300 K), where the D vs T curve is linear, and consequently he was unable to make definite conclusions regarding the behavior of nickel fluosilicate. Walsh[8] also performed stress measurements on Cr^{3+} in NH_4Al alum and KCo cyanide. The results were again analyzed in terms of crystal vibrational and static distortion effects, but an unsatisfactory fit was obtained with the pressure data because of the inhomogeneous elastic properties of the complex unit cell in these hosts. That is to say, the dimensions of the crystal unit cell do not scale linearly with pressure in the soft crystals, and so the theory cannot be successfully applied to the pressure results.

The hard crystals such as cubic MgO and ZnS provide a more favorable situation for pressure measurements, and they have been studied by Walsh et al.[9] For Mn^{2+} in MgO and ZnS and Fe^{3+} in MgO these authors were able to separate the relative effect of thermal expansion of the coordinated oxygen or sulfur octahedron from the cubic field splitting parameter a. In all cases the temperature dependence of this contribution is in the form of a quadratic function, with the most pronounced bend in the curves occurring below 200 K.

Shrivastava[10-13] has studied theoretically the effect of vibrations and static crystal distortion for a number of systems. The cubic field splitting parameter a of Mn^{2+} in MgO was separated into its component parts due to these two effects.[10] Here again the quadratic nature of the static crystal field is evident. The curve describing the temperature dependence of the vibrational contribution has the form of a hyperbolic cotangent. Shrivastava[12] was able to account for the ^{52}Cr, ^{53}Cr isotope effect of chromium impurities in axially symmetric sites in MgO in terms of the vibration of local impurity resonance modes. The vibrational contribution to the zero-field splitting parameter D of a given isotope was described by a function of the form $D = A \coth(\hbar\omega/2kT)$, where A is a constant and ω is the frequency of the impurity resonant mode. Shrivastava[13] has applied a Debye function to the D vs T curves of four alums to account for the temperature dependence of D due to vibrations. The D vs T curves consisted of at most four experimental points and the fit produced Debye temperatures of between 500 and 900 K in the crystals. It was concluded that the errors in the calculated parameters originate from the use of the Debye model.

Hartman et al.[14] performed precision relaxation measurements on Cr^{3+} impurities in MgO. They concluded that motions localized around each Cr^{3+} ion dominate the ground state relaxation. In particular, the motions were believed to be due to the CrO_6 complex. They were able to fit their experimental results quite well with a theory which suggests the importance of relaxation via the localized modes.

In the present study an analysis is made of the vibrational and static crystal distortion contributions to the $^{53}Cr^{3+}$ spin Hamiltonian parameters D, Q', A and B in trigonally distorted $Cr^{3+}.6H_2O$ magnetic complexes. An empirical approach is used to separate the parameters into their constituent parts due to the two types of contributions. The functional forms used for the contributions are based on the published experimental results described above. The analysis depends on the fact that experimental data are obtained for chromium magnetic complexes in many crystals and these are all considered together. The experimental results involve two types of data for the splitting procedure, namely plots of D vs T and Q' vs D, which cannot be analyzed separately but can be when taken together. Hence a method is developed to give a description of the vibrational and static crystal distortion contributions to the spin Hamiltonian parameters. This method is an alternative to that used in stress measurements which were found to be unsatisfactory for the types of crystals studied here. The results and method of the described analysis is then applied to alum crystals which undergo low T temperature phase transitions, and to the splitting of the Cr^{3+} A and B hyperfine parameters in the salts. The curves representing the temperature dependence of the vibrational and static parts of the various parameters present a new way of looking at the crystals.

CHAPTER 2

CRYSTALLOGRAPHY AND CRYSTAL DATA

2.1 The Guanidinium Salts

The chemical formula of guanidinium aluminum sulphate hexahydrate (termed GAlSH) is $C(NH_2)_3Al(SO_4)_2 \cdot 6H_2O$. The guanidinium cation $C(NH_2)_3^+$ is monovalent, the sulfate anion SO_4^{-2} is divalent, and the aluminum cation is trivalent. The isomorphs of GAlSH are obtained by replacing Al by Ga or S by Se, giving a total of four different crystals. The resulting combinations are listed in Table 2.1 along with the abbreviated symbols used to designate them. Some important crystallographic data are also listed with each entry in this table.

The crystallographic and dielectric studies of GAlSH and its isomorphs give a description of the structure and behavior of these crystals.[15-21] Geller and Booth[15] established from X-ray diffraction data that the crystal of GGaSH has a hexagonal structure with space group C_{3v}^2(P31m) and contains three formula units per unit cell. A diagram of the space group P31m is shown in Fig. 2.1(a). Schein et al.[16] have accurately determined the structure of GAlSH. A diagrammatic picture of this structure is given in Fig. 2.1(b). In this structure an $Al^{3+} \cdot 6H_2O$ complex is located at every three-fold axis site, and the same is true of the guanidinium complex.

TABLE 2.1 Isomorphs of GAlSH

Trivalent ion	S or Se	Chemical Formula	Abbreviation	Unit Cell a(Å)	Unit Cell c(Å)	Thermal expansion (10^{-6} deg.$^{-1}$) α_a	Thermal expansion (10^{-6} deg.$^{-1}$) α_c
Al^{3+}	S	$C(NH_2)_3Al(SO_4)_2.6H_2O$	GAlSH	11.745	8.592	10.05	92.80
Al^{3+}	Se	$C(NH_2)_3Al(SeO_4)_2.6H_2O$	GAlSeH	11.989	9.062	10.16	83.89
Ga^{3+}	S	$C(NH_2)_3Ga(SO_4)_2.6H_2O$	GGaSH	11.761	9.051	14.17	83.85
Ga^{3+}	Se	$C(NH_2)_3Ga(SeO_4)_2.6H_2O$	GGaSeH	12.020	9.144	12.07	71.16

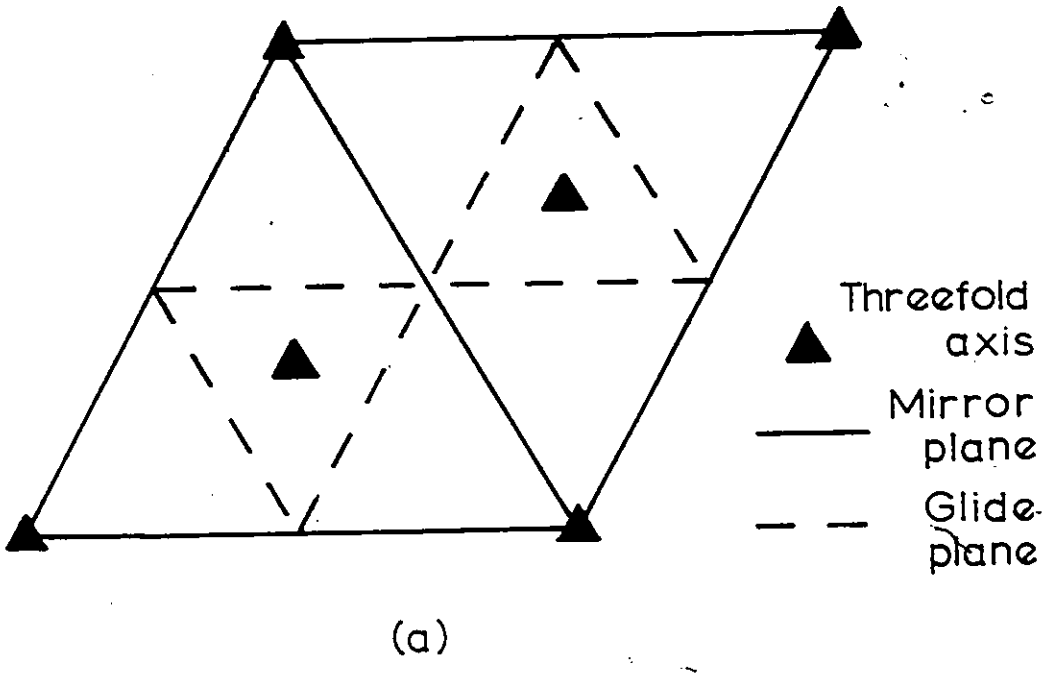

Fig. 2.1 (a) Diagram of P31m Space Group

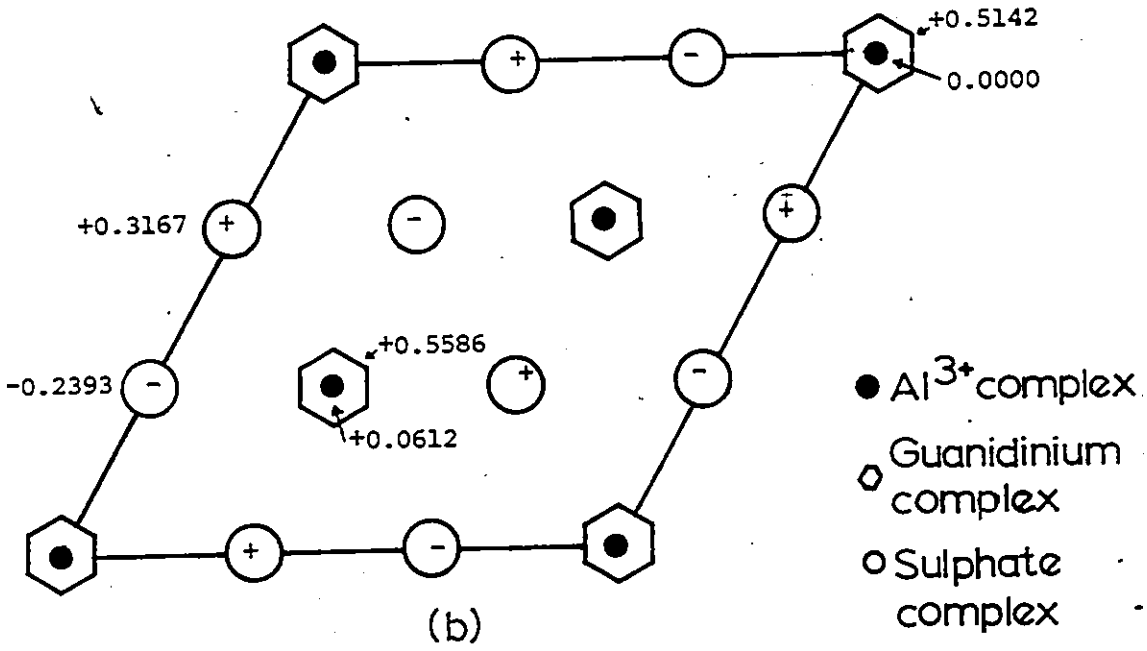

Fig. 2.1 (b) Structure of GAlSH looking down the C-axis. Heights are indicated in fraction of the lattice parameter C.

The sulfate groups are arranged so as to formaa hexagon around each $Al^{3+}.6H_2O$ complex. A more detailed structure is given in Fig. 2.2(a) and (b). Fig. 2.2(a) shows a map looking down the c axis of the two types of $Al^{3+}.6H_2O$ complexes that exist in a unit cell. The terms "corner" and "inside" refer to the aluminum positions at the ccorners or inside the unit cell of Fig. 2.1(b). There are twice as many equivalent inside complexes of $Al^{3+}.6H_2O$ as there are corner complexes. The point group symmetry of the corner complex is 3m while that of the inside complex is 3. The difference is due to the location of the H^+ ions of the waters in the complexes. Ions of the same type which lie in a plane normal to the crystal c axis are joined together by lines in Fig. 2.2. The lines are solid when the plane is above the Al^{3+} ion and broken when below it. For the corner complex, the H^+ ions of the water molecules located above the Al^{3+} ion all fall on the same plane, and the same is true for those located below it. For the inside complex they fall on two different planes. For simplicity the corner complex is designated by the number 1 while the inside complex is number 2. For example, the corner complex of GAlSH is designated by GAlSH(1).

The guanidinium structure is shown in Fig. 2.2(b)(i) and the sulfate structure is shown in Fig. 2.2(b)(ii). Half the sulfate groups point up the c axis and half point down.

The octahedron of waters surrounding each trivalent ion in the guanidinium salts is trigonally distorted by a slight compression along the crystal c axis. The amount of compression from octahedral symmetry at

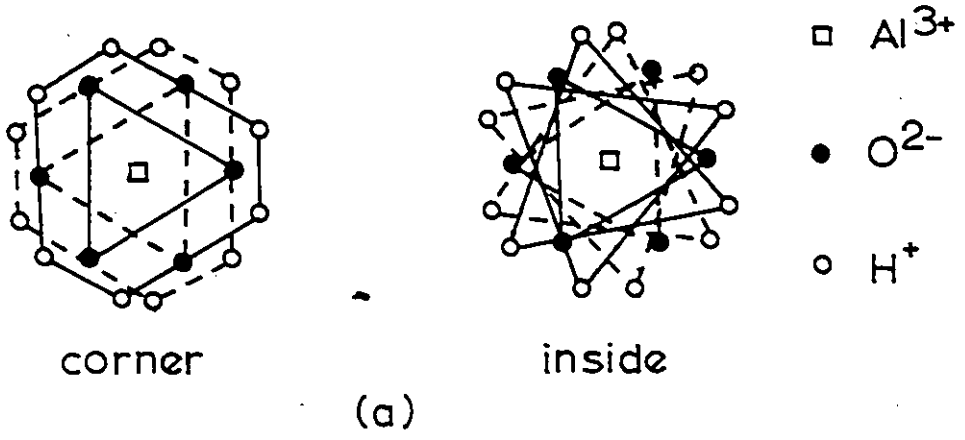

(a)

Fig. 2.2(a) Structure of Al^{3+} Complexes in GAlSH

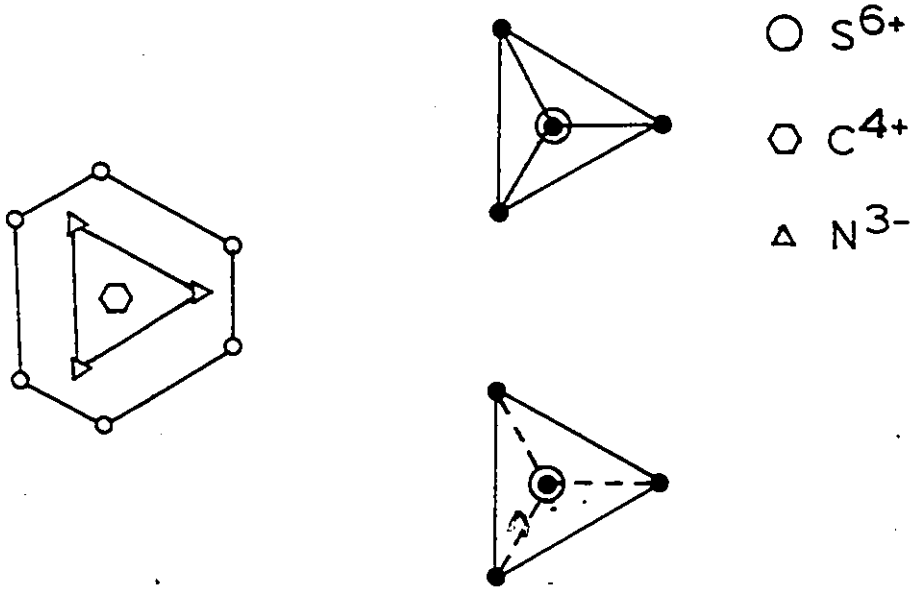

(b)

Fig. 2.2 (b) Structure of Guanidinium and sulfate Complexes in GAlSH

(i) Structure of the Guanidinium Complex

(ii) Structure of the Sulfate Complex

room temperature is 4% for the corner complex GAlSH(1) and 5% for the inside complex GAlSH(2). The trivalent ion is also somewhat displaced from the center of the octahedron.

The guanidinium salts were found to be ferroelectric[19,21] with the direction of spontaneous polarization being along the crystalcc axis. The polarization exists for all temperatures at which the crystals are stable. Holden et al.[21] found that the spontaneous polarization (P_s) versus the temperature (T) curves fall into two groups depending on whether sulfur or selenium is in the crystals, and that the polarizations increase with decreasing temperature. The selenates were found to have a larger value of P_s at all temperatures than do the sulfates. When Holden et al.[21] extrapolated their P_s curves to high T they predicted an upper limit of about 575 K for the Curie temperatures. An attempt to explain the ferroelectricity of GAlSH was made by Schein et al.[17] They proposed that c axis displacements of atomic positions which are not related by a center of symmetry, and are not compensated for by displacements in the opposite direction, are responsible for the ferroelectric properties. These conditions were found to hold for the trivalent ion complexes in the crystals.

The ESR of Cr^{3+} in GAlSH and its isomorphs has been studied by a number of authors.[22-25] None of these works contains a complete set of measurements of the zero-field splitting parameter D for all the magnetic complexes in the salts over the whole temperature range 4.2 - 297 K.

In fact no measurements are reported at 4.2 K, and this is the temperature where ENDOR measurements are made. For all temperatures where measurements are done, two nonequivalent magnetic complexes exhibiting axial symmetry about the c axis are found in each crystal. The ESR lines for one complex have twice the intensity of the other, indicating that the former is due to two equivalent magnetic complexes. This result is consistent with the crystallographic data described above, and the magnetic complexes correspond to the sites denoted there as (2) and (1). At all temperatures where measurements were done, complex (2) has a smaller D value than does complex (1). This is in spite of the fact that complex (2) has the greater percentage distortion from octahedral symmetry at room temperature. Actually the relationship between the magnitude of the measured D value and the size of the static distortion at the Cr^{3+} site has not been previously determined.

2.2 The Alums

The alums belong to the cubic system with space group $T_h^6(Pa3)$ and they exist in three types, termed α, β and γ, because of small differences in atomic arrangements. The general formula for the sulfate alums is $M^+M^{3+}(SO_4)_2 \cdot 12H_2O$ with four formula units per unit cell. M^+ and M^{3+} represent monovalent and trivalent cations, respectively. Each trivalent ion is surrounded by a nearly regular octahedron of water molecules. Other alums can be grown by replacing sulfur with selenium or tellurium.

However the production of crystals containing Se or Te is more difficult because the appropriate chemicals are not readily available. This is especially true in the present study on $Cr.6H_2O$ complexes where one wishes to dope the crystals with chromium.

In the X-ray crystallographic studies of Lipson and Beevers[26] and Lipson[27] it was shown that in the α type alums the [111] axis of the octahedron of water molecules surrounding an aluminum ion coincides with the [111] crystal axis, but the cubic axes of the octahedron are displaced from the cubic axes of the crystal by a rotation of approximately 9.5° about the [111] direction. The β alums were found to have perfectly regular groups of water molecules with the cubic axes of the octahedron being directed along the cubic axes of the crystal. In soda alum $NaAl(SO_4)_2.12H_2O$, which is the only known γ alum, the octahedron of waters surrounding an aluminum atom is rotated by approximately 40° about the crystal [111] direction. The water octahedron about an aluminum atom in this crystal was shown to form a perfect octahedron.

Lipson[27] attempted to classify the alums in terms of the size of the monovalent ion. The α structure was said to be represented by medium sized ions, β by larger ions, and γ by the small sodium ion. For example, RbAl and RbGa sulfate alums are of α type while CsAl and CsGa sulfate alums are of β type. Klug and Kieffer[28] compared X-ray structure factors of TlGa sulfate alum with those obtained in the Cs and Rb alums and concluded that TlGa alum was of β type. These authors

also concluded that the trivalent ion can also affect the alum type in some cases. In particular, their studies showed that RbCr alum is of β type. The types of sulfate alums of interest in this work are shown in Table 2.2. The ionic radii of pertinent ions are shown in Table 2.3.

The alum type is also influenced by the SO_4 cation ion arrangement in the crystals. In the β type alums the SO_4 group forms an almost perfect tetrahedron. The S^{6+} cation and one oxygen are on the [111] crystal axis with the oxygen being closest to the trivalent cation. In the γ type, the tetrahedron is slightly distorted and is oriented in the opposite direction to that of the β alums. A mixed situation exists in the α type alums with some of the tetrahedrons being oriented as in the β type and some as in the γ type. As the monovalent cation decreases in size, the fraction of tetrahedra oriented as in the γ type increases.[29] A further complication is introduced into the picture when the S^{6+} ion is replaced by Se^{6+}. As seen in the magnetic resonance results described below, the CsAl and CsGa selenate alums act like α type instead of β type as for the corresponding sulfate alums. In view of all these complexities, it should be mentioned at this point that the magnetic behavior of the crystals, as determined from the $Cr^{3+}.6H_2O$ magnetic complexes, is quite orderly. Moreover, it is found in the subsequent analysis that all the hydrated crystals containing trigonally distorted $Cr^{3+}.6H_2O$ magnetic complexes are related to each other in a

TABLE 2.2 Types of Sulfate Alums Formed for Various Combinations of Monovalent and Trivalent Cations.

MONOVALENT CATION.	TRIVALENT CATION. Al	Ga	Cr	In
Rb	α	α	β	α
Tl	β	β	β	β
NH_4	α	α	α	α
Cs	β	β	β	β
K	α	α	α	α

TABLE 2.3 Ionic Radii and Natural Atomic Masses.

Ion	Ionic Radius (Å)	Natural atomic mass (u)
Al^{3+}	0.51	26.9815
Cl^{1-}	1.81	35.453
Cr^{3+}	0.63	51.996
Cs^{1+}	1.67	132.905
Ga^{3+}	0.62	69.72
In^{3+}	0.81	114.82
K^{1+}	1.33	39.101
NH_4^{1+}	1.43	18.0386
O^{2-}	1.32	15.9994
Rb^{1+}	1.47	85.47
S^{6+}	0.30	32.064
Se^{6+}	0.42	78.96
Tl^{1+}	1.47	204.37

particular way. This feature includes the guanidinium crystals and also $AlCl_3.6H_2O$.

Bleaney[30] has determined from ESR studies that when ammonium and potassium sulfate alums are cooled, they undergo phase transitions at 81 and 160 K, respectively. The ESR spectra obtained below the transition temperatures in these crystals differed considerably from those obtained above the transitions. Chicault[31] studied the ESR spectrum of Cr^{3+} impurities in deuterated NH_4Al sulfate alum below the transition temperature, which he said occurred at 56 K, and observed twelve chromium magnetic complexes exhibiting rhombic symmetry. The Z axes of the magnetic complexes were found to make large angles with the crystal [111] directions. In the hydrated form of this salt O'Reilly and Tsang[32] observed the transition to occur at 71 K. Those authors also observed[32] a phase transition to occur in NH_4In sulfate alum at 127 K. Burns[33] studied the quadrupole moment of Al in KAl alum as a function of temperature and observed a phase transition to occur at 98 K in this salt. The analysis of the magnetic resonance results obtained in the present work enables an explanation to be made regarding the mechanisms of the various phase transitions.

2.3 $AlCl_3.6H_2O$

X-ray crystallographic studies by Andress and Carpenter[34] established the space group of aluminum chloride hexahydrate, $AlCl_3.6H_2O$,

to be $R\bar{3}c$. Buchanan and Harris[35] measured the lattice parameters in terms of a hexagonal unit cell and obtained the values $a = 11.827$ and $c = 11.895$ Å. The crystal is made of chains of the form $-Al(H_2O)_6^{3+} - 3Cl^- - Al(H_2O)_6^{3+} - 3Cl^- -$ running parallel to the c axis of the hexagonal unit cell. The Al^{3+} ion is situated at the center of the octahedron of waters, and along each chain alternate octahedra are rotated with respect to each other by 28° along their [111] direction which is along the crystal c direction. The ENDOR of $^{53}Cr^{3+}$ impurities in $AlCl_3.6H_2O$ was studied by Pack et al.[3] Only one type of chromium magnetic complex was found in the crystal.

2.4 Crystal Preparation

All the crystals were grown by slow evaporation at room temperature of a saturated solution of the constituent salts. In the lightly doped crystals a small amount of the Cr^{3+} ion is added to the solutions. The crystals produced are clear and nearly colorless. It was estimated that the crystals contained no more than 0.01 wt % of Cr^{3+} impurities. In the case of RbCr and CsCr sulfate alums, the chromium was mixed in the solutions in the correct stoichiometric amounts. These crystals were almost black in appearance. Two batches of each type of dilutely doped crystals were grown, one batch containing the chromium impurity in its natural isotropic abundance and the other containing $^{53}Cr^{3+}$ enriched to 94%. The latter is required when performing ENDOR

studies but either one can be used in the ESR studies since the same zero-field splitting D value is measured in each case. The $^{53}Cr^{3+}$ ion was obtained as $Cr_2(SO_4)_2$, which is nearly insoluble in water but is somewhat soluble in hot acid. The $Cr_2(SO_4)_2$ is dissolved in sulfuric acid for the sulfate crystals and in selenic acid for the selenate crystals. The method used to prepare the isomorphs of GAlSH was the same as that described by Carlin and Walker[5].

CHAPTER 3

THEORY

3.1 The ENDOR Technique

The ENDOR technique allows a direct measurement to be made of the hyperfine splittings of energy levels.[36,37] The hyperfine interaction is the interaction between a nucleus and the electrons surrounding it. An illustration of the technique can be obtained from the simple example shown in Fig. 3.1, which represents the case of a nucleus with nuclear spin I = 1/2 interacting with electrons with an effective spin of S = 1/2. At the lower part of the figure are shown the two expected ESR lines of energy $h\upsilon_1$. Both the direct and first derivative signals of the spectrum are shown. The hyperfine ESR lines are shown only partially resolved, as is typically the case. Even if the resonance lines were well resolved it is not possible to measure their separation with great precision using ordinary ESR.

To observe ENDOR the magnetic field is adjusted to the center of an ESR line and enough microwave power is applied to partially saturate the transition, i.e., to nearly equalize the population of the upper level with that of the lower. This causes a decrease in the ESR line intensity. An oscillator, which is coupled to the sample by two or three turns of wire, is then swept in frequency through the range corresponding to the spacings between the hyperfine lines at the given field position. When a nuclear resonance is achieved this causes an

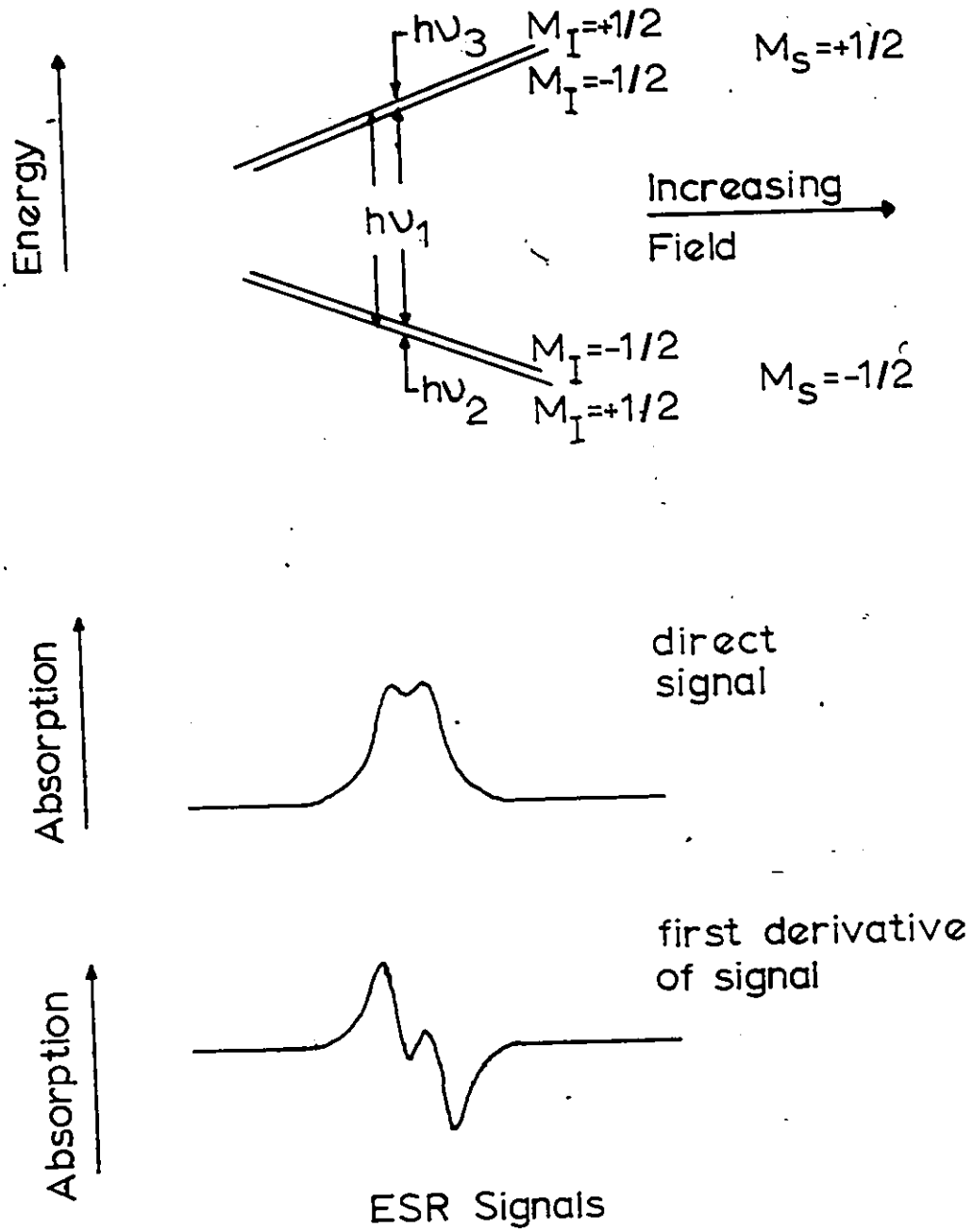

Fig. 3.1 Typical ESR Spectrum of a system for which

I = 1/2 and S = 1/2

unbalance in the spin populations of the ESR transition with a consequent increase in the ESR signal. The frequencies of the nuclear resonance transitions can then be read from a frequency counter which is also connected to the oscillator. For the example of Fig. 3.1, the frequencies ν_2 and ν_3 would be obtained. The ENDOR method gives an increase in the resolution of the nuclear levels by an amount equal to the ratio of the electronic to the nuclear magneton, which is a factor of about 10^3. ENDOR measurements can be made even if the ESR hyperfine structure is completely unresolved.

3.2 The Hamiltonian

The terms of the Hamiltonian describing the energy levels of the paramagnetic ion in the crystal can be written as:

$$\mathcal{H} = \mathcal{H}_1 + \mathcal{H}_2 + \mathcal{H}_3 + \mathcal{H}_4 + \mathcal{H}_5 + \mathcal{H}_6 + \mathcal{H}_7 + \mathcal{H}_8.$$

The various terms have been reviewed in the literature[38] and they are briefly discussed below. The nature of the terms are important in understanding the ESR and ENDOR data, and consequently the physical behavior of the crystals.

3.3 Kinetic Energy and the Coulomb Interaction

The Hamiltonian term $\mathcal{H}_1$ represents the kinetic energy of the electrons and the Coulomb interaction between them. It represents the

energy of the free atom and it is of the form

$$\mathcal{H}_1 = \sum_i \left(\frac{\vec{p}_i^2}{2m_o} - \frac{Ze^2}{r_i} \right) + \sum_{i<k} \frac{e^2}{r_{ik}} .$$

Here, $\vec{p}_i$ is the momentum of the i'th electron, m_o is its rest mass, r_i is the distance between the i'th electron and the nucleus, Z is the atomic number of the atom, and r_{ik} is the distance between the i'th and k'th electrons. The summation is over all the electrons in the atom. Hence, the first term of $\mathcal{H}_1$ represents the kinetic energy of the electrons, the second term represents the attractive Coulomb interaction between the nucleus and the electrons, and the third term represents the Coulomb repulsion between the electrons. $\mathcal{H}_1$ is usually the largest term in the general Hamiltonian, with a typical energy of the order 10^5 cm^{-1} ($\sim$ 10 eV). This order of energy falls in the optical region of the electromagnetic spectrum.

3.4 Crystal Field Interaction

$\mathcal{H}_2$ is that part of the Hamiltonian which describes the interaction energy of the electrostatic field of neighbouring atoms with that of the paramagnetic ion. It is usually termed the crystal field interaction and is given by

$$\mathcal{H}_2 = \sum_i e_i V(\vec{r}_i) ,$$

where $V(\vec{r}_i)$ is the electrostatic potential at the ion due to the ligands with which each electron i interacts. The size of this term may vary widely in magnitude, and it may be as large as 10^4 cm^{-1} ($\sim$ 1 eV). This order of energy falls in the optical region of the electromagnetic spectrum. In GAlSH its magnitude is of the order 2 X 10^4 cm^{-1} ($\sim$ 2 eV).

All the magnetic complexes studied in this work consist of a Cr^{3+} ion surrounded by an octahedral array of six water molecules subjected to a small trigonal distortion. The effect of a perfect octahedral array of charges on the chromium ground state can be found quite easily. In this case the octahedron may be considered as three mutually perpendicular electric dipoles, with one dipole being along each of the coordinate X, Y and Z axes. In this case the term $\mathcal{H}_2$ is given by the fourth order expression

$$\mathcal{H}_2 = D \sum_i (X_i^4 + Y_i^4 + Z_i^4 - (3/5)r_i^4),$$

where $\vec{r}_i$ is the vector from the center of the octahedron to the i'th electron. D is a constant given by $D = 35Ze/4a^5$, where a is half the height of the octahedron. A constant term also exists in $\mathcal{H}_2$ but it is omitted since it cannot be detected by ESR. The expression for $\mathcal{H}_2$ can be converted into orbital angular momentum operator equivalents as done by Stevens[38], which gives

$$\mathcal{H}_2 = Dq \{\frac{1}{20} [35L_Z^4 - 30L(L+1)L_Z^2 + 25L_Z^2 - 6L(L+1) + 3L^2 (L+1)^2] + \frac{1}{8} (L_+^4 + L_-^4)\} .$$

In this expression q is a constant given by $q = 2e\langle r^4\rangle/105$, where $\langle r^4\rangle$ is the average of the fourth power radius of the outer electrons of the central paramagnetic ion.

The free ion ground state of Cr^{3+} is $^4F_{3/2}$ with L = 3 and S = 3/2, and a degeneracy of (2S+1)(2L+1) = 28 with respect to the M_S and M_L values. When the energy operator $\mathcal{H}_2$ is applied to the ground state wave functions then the orbital levels are split by an amount 10 Dq and 8 Dq as shown in Fig. 3.2. The new ground state $^4S_{3/2}$ is an orbital singlet while the $^4P_{3/2}$ excited states are orbital triplets. Each orbital state remains four-fold degenerate with respect to M_S. The effect of a slight trigonal distortion of the octahedron is also shown in Fig. 3.2. Its effect is to split each of the excited $^4P_{3/2}$ states into an orbital singlet and doublet.

3.5 Spin-Orbit Interaction

$\mathcal{H}_3$ refers to the spin-orbit interaction and is given by

$$\mathcal{H}_3 = \sum_{i,j} \lambda_{ij} \vec{\ell}_i \cdot \vec{s}_j ,$$

where $\vec{\ell}_i$ is the orbital angular momentum of the i'th electron, $\vec{s}_j$ is the spin angular momentum of the j'th electron, and λ_{ij} is the coupling constant between the electrons. The summation is over all the electrons in the atom. With respect to the ground state wave functions produced by the interaction $\mathcal{H}_1$, the spin-orbit interaction can be written as

$$\mathcal{H}_3 = \lambda \vec{L} \cdot \vec{S},$$

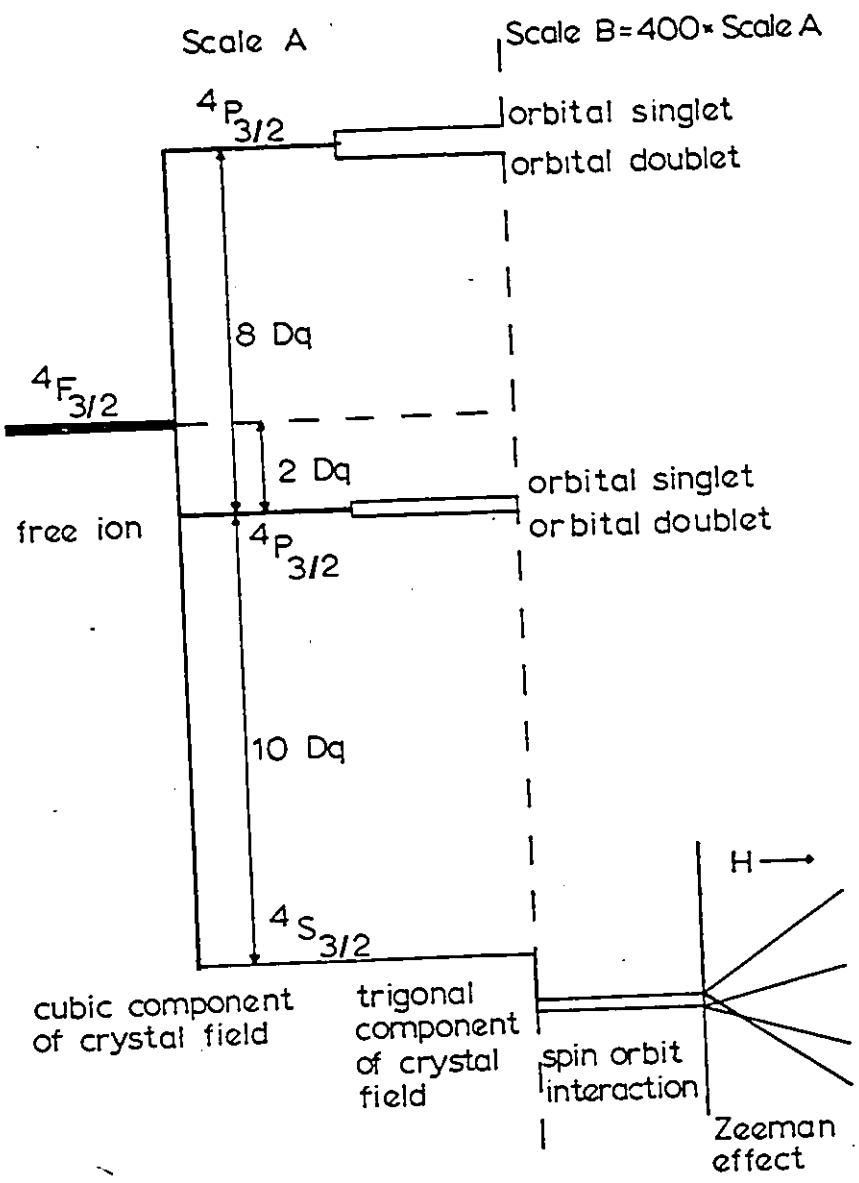

Fig. 3.2 Energy Level Diagram of Cr^{3+} in a Trigonally Distorted Octahedron.

where $\vec{L}$ is the free ion orbital angular momentum and $\vec{S}$ is its spin angular momentum. In general, the magnitude of $\mathcal{H}_3$ depends on the value of the coupling constant λ and the free ion ground state, but it is usually of the order of 10^2 cm^{-1} ($\sim 10^{-2}$ eV). This value of energy falls in the infrared region of the electromagnetic spectrum. The effect of the spin-orbit interaction on the chromium $^4S_{3/2}$ ground state is to split it in two spin doublets, called Kramer's doublets, as shown in Fig. 3.2. One of the doublets contains the states $M_S = \pm 1/2$ and the other $M_S = \pm 3/2$. It is noted in Fig. 3.2 that scale B for the energy splitting is magnified 400 times over scale A. The magnitude of the splitting due to the spin-orbit interaction depends on the value of λ and 10 Dq and the amount of trigonal distortion.

3.6 Spin-Spin Interaction

The spin-spin term is due to the interaction between the spin magnetic moments of the electrons, and is given by the expression

$$\mathcal{H}_4 = 4\beta^2 \sum_{i<k} \left\{ \frac{\vec{s}_i \cdot \vec{s}_k}{r_{jk}^3} - \frac{3(\vec{r}_{jk} \cdot \vec{s}_j)(\vec{r}_{jk} \cdot \vec{s}_k)}{r_{jk}^5} \right\} ,$$

where the summation is over all the pairs of electrons of the ion. With respect to the free ion wave function, this term can be written as

$$\mathcal{H}_4 = -\rho \, (\vec{L} \cdot \vec{S})^2 + \frac{1}{2}(\vec{L} \cdot \vec{S}) - \frac{1}{3} L \, (L+1) S (S+1) ,$$

where ρ is a proportionality constant. The spin-spin interaction represents a small value of energy causing a shift of energy levels by an order of 10^{-1} cm^{-1} (10^{-5} eV).

3.7 Electronic Zeeman Interaction

The interaction of the electrons' magnetic moments with that of an external magnetic field $\vec{H}$ is given by

$$\mathcal{H}_5 = \sum_i \beta(\vec{\ell}_i + 2\vec{s}_i)\cdot\vec{H}.$$

with respect to the free ion ground state wave functions, the Zeeman interaction can be written as

$$\mathcal{H}_5 = \beta\vec{H}\cdot(\vec{L}+2\vec{S}),$$

where β is the Bohr magneton. The effect of this term is shown in Fig. 3.2, and the energy spacings are best observed in the microwave region of the electromagnetic spectrum.

3.8 Hyperfine Interaction

The hyperfine interaction arises in atoms whose nuclei possess a nuclear spin, and the interaction is between the nuclear magnetic moment and the magnetic moments of the electrons. The term is given

by the expression

$$\mathcal{H}_6 = g g_N \beta \beta_N \{ \sum_k [\frac{(\vec{\ell}_k - \vec{s}_k) \cdot \vec{I}}{r_k^3} + \frac{3(r_k \cdot \vec{s}_k)(\vec{r}_k \cdot \vec{I})}{r_k^5}]$$

$$+ \frac{8\pi}{3} \cdot \delta(r_k)(\vec{s}_k \cdot \vec{I}) \} ,$$

where the symbols have their usual meanings. The two terms in the square brackets describe the dipole-dipole interaction between the nucleus and electrons. The last term is the Fermi contact term, and it represents the anomalous interaction of the s electrons with the nuclear spin. It is proportional to the unpaired electronic spin density at the nucleus which is non-zero only for s orbitals. Since Cr^{3+} has no unpaired s electrons, one would expect the Fermi contact term to be zero, but experiments show that this is not so. The discrepancy is explained by configuration mixing and core polarization. Configuration mixing is due to a small admixture of an excited s state into the ground state. In core polarization the unpaired Cr^{3+} d electrons tend to polarize the inner s orbitals, and this polarization is different for spin-up and spin-down electrons. Hence this effect gives rise to an unpaired spin density at the nucleus.

Using the free ion wave functions as a basis, the hyperfine term can be written as

$$\mathcal{H}_6 = \frac{g g_N \beta \beta_N}{\langle r^3 \rangle} \{ (\vec{L} \cdot \vec{I}) + [\xi L(L+1) - K](\vec{S} \cdot \vec{I})$$

$$- \frac{3}{2} \xi [(\vec{L} \cdot \vec{S})(\vec{L} \cdot \vec{I}) + (\vec{L} \cdot \vec{I})(\vec{L} \cdot \vec{S})] \} .$$

In this expression, K is a measure of the non-zero electron density at the nucleus and ξ is a proportionality constant given by

$$\xi = \frac{2\ell+1 - 4S}{S(2\ell-1)(2\ell+3)(2L+1)},$$

where ℓ is the orbital quantum number referring to the d electron in the case of Cr^{3+}. $\mathcal{H}_6$ causes a splitting of the Zeeman energy levels by an order of 10^{-2} cm^{-1} (10^{-6}eV). For $^{53}Cr^{3+}$ the amount of splitting is in the range 25-80 MHz.

3.9 Electric Quadrupole Interaction

Nuclei with spin I>1/2 which possess an electric quadrupole moment Q will interact with a non-uniform electric field at the nucleus to produce small changes in the hyperfine spacings of the Zeeman lines as given by $\mathcal{H}_6$. The quadrupole interaction is given by

$$\mathcal{H}_7 = \frac{e^2Q}{2I(2I-1)}\left[\sum_i \frac{I(I+1)}{r_i^3} - \frac{3(\vec{r}_i\cdot\vec{I})^2}{r_i^5}\right]$$

With respect to the free ion ground state wave functions we have

$$\mathcal{H}_7 = \frac{\eta e^2 Q}{2I(2I-1)r^3}\{3(\vec{L}\cdot\vec{I})^2 + \frac{3}{2}(\vec{L}\cdot\vec{I}) - L(L+1)I(I+1)\}$$

where η is a constant. The shift of the Zeeman hyperfine energy levels due to $\mathcal{H}_7$ for the case of $^{53}Cr^{3+}$ is approximately an order of magnitude less than for $\mathcal{H}_6$.

3.10 Nuclear Zeeman Effect

The nuclear Zeeman interaction is described by the term

$$\mathcal{H}_8 = - g'_N \beta_N \vec{H} \cdot \vec{I}.$$

This term causes a shift in the hyperfine lines by an order of 10^{-3} cm^{-1} (10^{-7}eV). Hence it falls in the radio frequency range of the electromagnetic spectrum.

3.11 The Spin Hamiltonian

Pryce[39] and Abragam and Pryce[40] developed a method to describe the ground state zero-field and Zeeman splitting in terms of an effective spin Hamiltonian. The method is based on the fact that transitions are observed between the lowest energy levels in the phenomenon of paramagnetic resonance. If transitions between $2S'+1$ levels are observed experimentally, then S' can be defined as the fictitious spin of the system. In some cases, such as the $^4P_{3/2}$ ground state of Cr^{3+}, the fictitious spin is identical to the free ion spin. In obtaining the spin Hamiltonian, the terms $\mathcal{H}_3$ to $\mathcal{H}_8$ are applied as a perturbation to the manifold of energy states which were produced by $\mathcal{H}_2$ acting on the ground state term of the free ion.

The total perturbation in this case is

$$\mathcal{H}' = \mathcal{H}_3 + \mathcal{H}_4 + \mathcal{H}_5 + \mathcal{H}_6 + \mathcal{H}_7 + \mathcal{H}_8$$

$$= \{\lambda \vec{L}\cdot\vec{S}\} + \{-\rho(\vec{L}\cdot\vec{S})^2 + \frac{1}{2}(\vec{L}\cdot\vec{S}) - \frac{1}{3}L(L+1)S(S+1)\}$$

$$+\{\beta\vec{H}\cdot(\vec{L}+2\vec{S})\} + \frac{gg_N\beta\beta_N}{\langle r^3\rangle}\{(\vec{L}\cdot\vec{I}) +$$

$$[\xi L(L+1) - K](\vec{S}\cdot\vec{I}) - \frac{3}{2}\xi[(\vec{L}\cdot\vec{S})(\vec{L}\cdot\vec{I})$$

$$+ (\vec{L}\cdot\vec{I})(\vec{L}\cdot\vec{S})]\} + \frac{ne^2Q}{2I(2I-1)r^3}\{3(\vec{L}\cdot\vec{I})^2$$

$$+ \frac{3}{2}(\vec{L}\cdot\vec{I}) - L(L+1)I(I\ 1)\} + \{-g_N\beta_N\vec{H}\cdot\vec{I}\}.$$

The effective spin Hamiltonian that is obtained is written as

$$\mathcal{H}_S = \beta\vec{H}\cdot\tilde{g}\cdot\vec{S} + \vec{S}\cdot\tilde{D}\cdot\vec{S} + \vec{S}\cdot\tilde{A}\cdot\vec{I} + \vec{I}\cdot\tilde{Q}'\cdot\vec{I}$$

$$- \beta_N\vec{H}\cdot\tilde{g}_N'\cdot\vec{I},$$

where the symbol (~) indicates a tensor quantity. Beginning with the first term, the terms describe the electronic Zeeman splitting, the zero-field splitting, the hyperfine interaction, the quadrupole interaction and the nuclear Zeeman effect. The advantage of using a spin Hamiltonian is that the rather complicated behavior of the lowest energy levels of the paramagnetic ion in a crystal subjected to a magnetic field can be

described in a relatively simple way by specifying the effective spin, together with a small number of parameters which measure the magnitudes of the various terms in the Hamiltonian. One must then find a model of the crystal field which corresponds to the spin Hamiltonian and which will explain the observed parameters.

In terms of the principal axes system, which is determined by the symmetry of the crystalline electric field, $\mathcal{H}_S$ can be written as

$$\mathcal{H}_S = \sum_{\substack{i= \\ x,y,z}} (\beta g_i H_i S_i + D_i S_i^2 + A_i S_i I_i + Q_i' I_i^2 - \beta_N g_{N_i}' H_i I_i) \qquad (3.1)$$

It is customary to write

$$\sum_{\substack{i= \\ x,y,z}} D_i S_i^2 = D\{S_z^2 - \frac{1}{3} S(S+1)\} + E(S_x^2 - S_y^2)$$

and

$$\sum_{\substack{i= \\ x,y,z}} Q_i' I_i^2 = Q'\{I_z^2 - \frac{1}{3} I(I+1)\} + \frac{\eta'}{3}(I_x^2 - I_y^2).$$

Here $D = (3/2)D_z$ is called the axial crystal field parameter or zero-field splitting parameter, and $E = (1/2)(D_x - D_y)$ is the rhombic field parameter, $Q' = (3/2)Q_z'$ is the axial electric field quadrupole coupling constant, and $\eta' = (Q_x' - Q_y')/Q_z'$ is the rhombic field parameter. When the crystal field has axial symmetry then we can write $g_z = g_{\parallel}$, $g_x = g_y = g_{\perp}$;

$D_x = D_y$ and so $E = 0$; $A_z = A$, $A_x = A_y \equiv B$; $Q'_x = Q'_y$ and so $\eta' = 0$; $g'_{N_z} = g'_{N_{||}}$, $g'_{N_x} = g'_{N_y} \equiv g'_{N_\perp}$. The symbols $||$ and $\perp$ refer to parallel and perpendicular, respectively. For the case of axial symmetry Eq. 3.1 can then be written as

$$\begin{aligned}\mathcal{H}_S = {} & g_{||}\beta S_z H_z + g_\perp \beta (H_x S_x + H_y S_y) + D\left(S_z^2 - \tfrac{1}{3}S(S+1)\right) \\ & + A S_z I_z + B(S_x I_x + S_y I_y) + Q'\left(I_z^2 - \tfrac{1}{3}I(I+1)\right) \\ & - g'_{N_{||}} \beta_N I_z H_z - g'_{N_\perp} \beta_N (H_x I_x + H_y I_y).\end{aligned} \tag{3.2}$$

The matrix elements of the spin Hamiltonian given by Eq. 3.2 are obtained by operating with $\mathcal{H}_S$ on the ground state manifold of wave functions $|M_S, M_I>$. For $^{53}Cr^{3+}$ we have S = 3/2 and I = 3/2, and so there are $(2S+1)(2I+1) = 16$ different states. Hence the dimension of the matrix described by Eq. 3.2 is 16 X 16. When the applied magnetic field is directed along the z axis then $H_x = H_y \equiv 0$, and the $\mathcal{H}_S$ matrix obtained in this case is shown in Fig. 3.3. When the magnetic field is along a direction perpendicular to the z axis, then the terms of the Hamiltonian given by Eq. 3.2 must be transformed by a rotation to that direction. The rotated form of $\mathcal{H}_S$ has been given by Laurance and Lambe[41] and its matrix elements along the $\perp$ direction are shown in Fig. 3.4. In Fig. 3.3 the compact notation used is $G = g_{||}\beta H_z$, $G' = g'_{N_{||}}\beta_N H_z$, and in Fig. 3.4 $G = g_\perp \beta H_\perp$ and $G' = g'_{N_\perp}\beta_N H_\perp$.

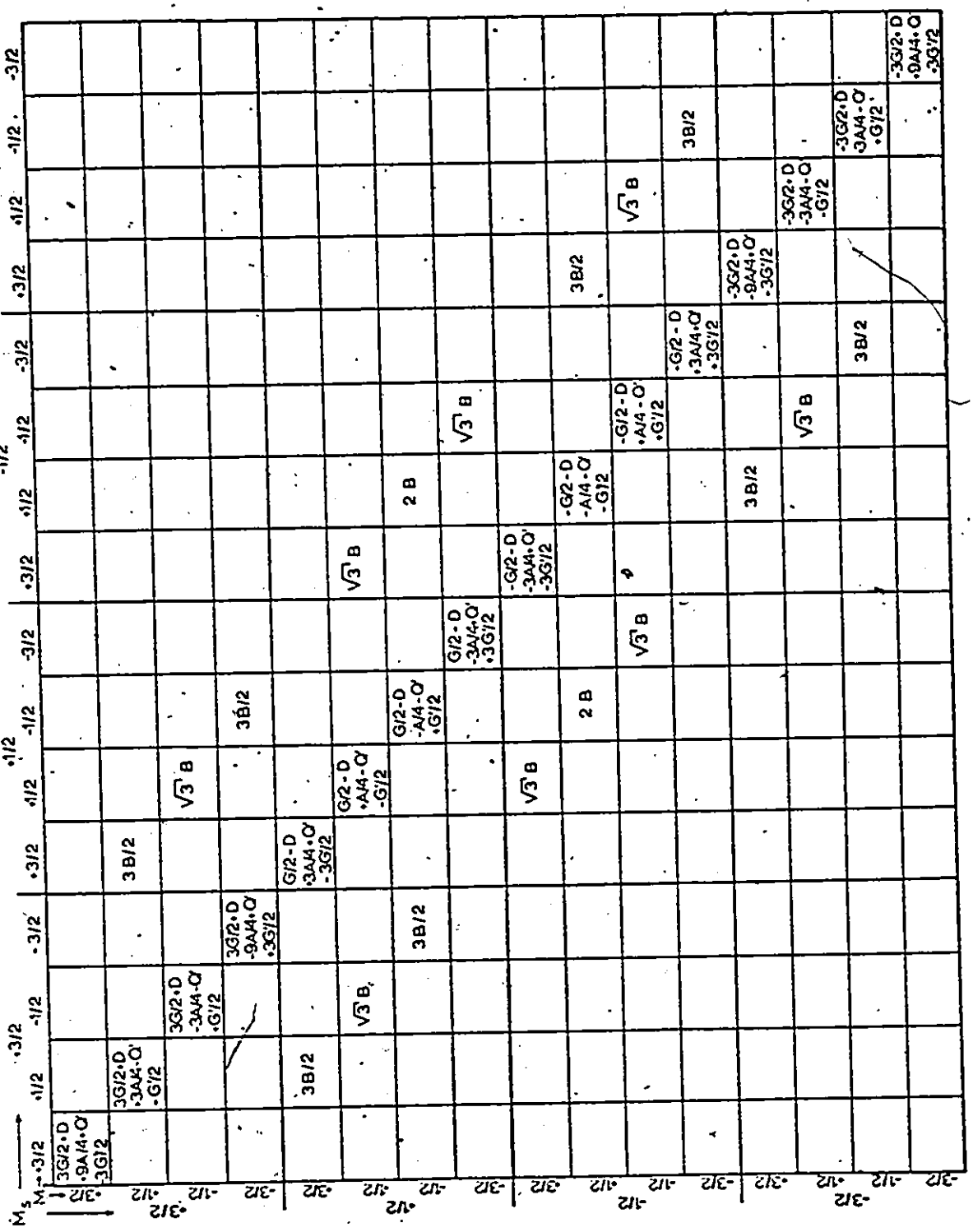

Fig. 3.3 Effective Spin Hamiltonian Matrix with the Magnetic Field applied in the Z Direction.

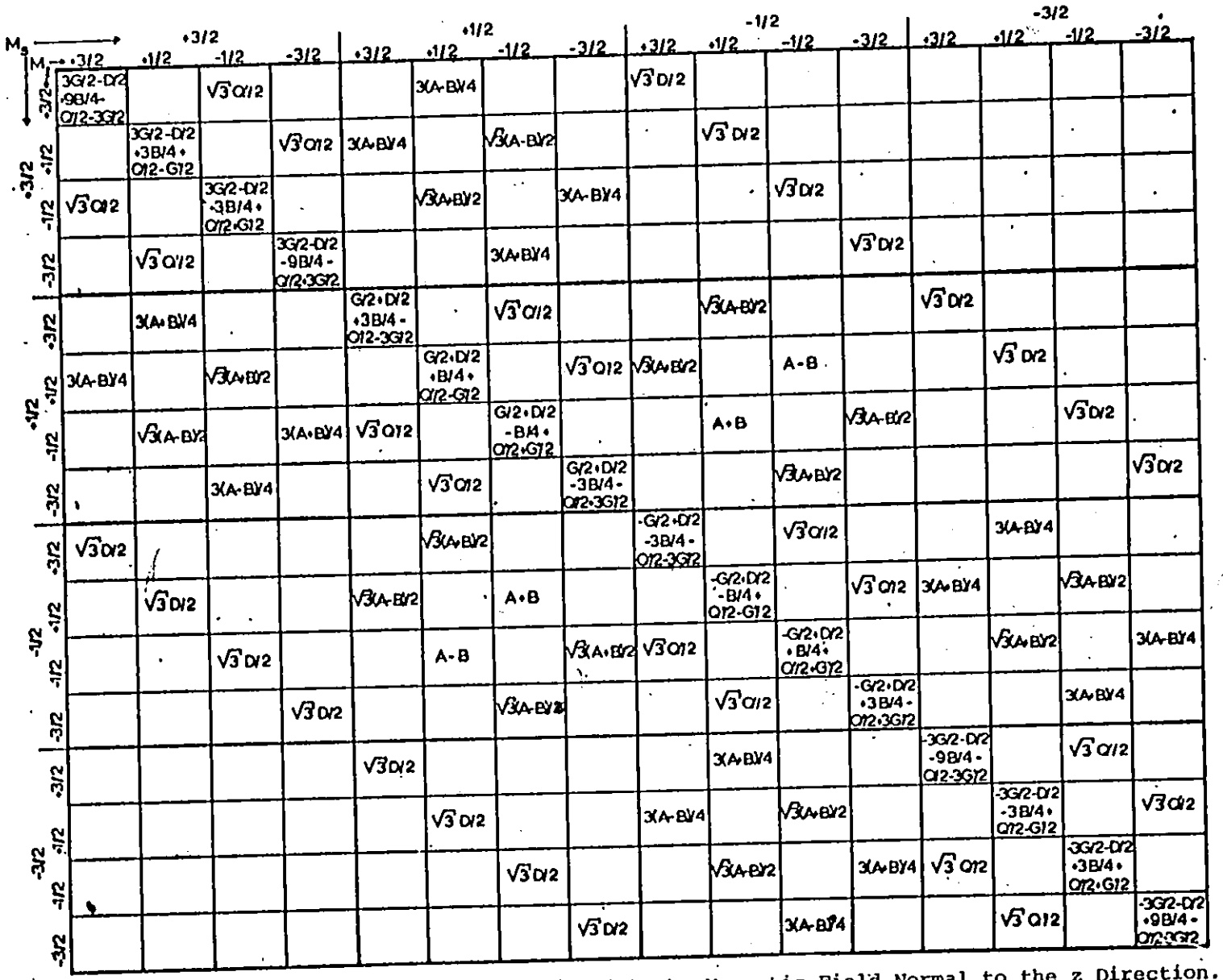

Fig. 3.4 Effective Spin Hamiltonian Matrix with the Magnetic Field Normal to the z Direction.

3.12 Description of Electronic g Values ($g_{||}$, $g_{\perp}$) in the Spin Hamiltonian

The electronic g factor is defined as the ratio of the electronic magnetic moment to the angular momentum, expressed in dimensionless units. In solids the electronic orbital motion of the valence electrons interacts strongly with the crystalline electric field $\mathcal{H}_2$ and becomes decoupled from the spin, a process called quenching. The more complete the quenching the closer the electronic g value will approach the free electron value of 2.0023. The g factor for an ion in a crystal is often anisotropic, having a different value along the principal x, y and z directions. In the case of an axial symmetric crystalline electric field the values of g along the $\perp$ directions x and y are the same. In the derivation of the spin Hamiltonian from the perturbation method described in section 3.11, the tensor components of the g value along the principal-directions for Cr^{3+} are given by

$$g_{ij} = 2.0023 \ (\delta_{ij} - \lambda \Lambda_{ij}).$$

where λ is the spin-orbit coupling constant and Λ_{ij} is the tensor describing the quenching. The effect of Λ_{ij} is to mix some of the excited orbital states into the ground state.

3.13 Description of the D Parameter in the Spin Hamiltonian

The D parameter is called the zero-field splitting parameter because it is a measure of the ground state Kramer's doublet splitting in an axial crystalline electric field when the applied magnetic field is zero.

O'Reilly and Tsang[32] have given the following equation which relates the D parameter to the electric field gradiant V_{zz} due to charges and dipoles external to the Cr^{3+} ion in the crystal:

$$D = \frac{3}{7} \left(\frac{\lambda}{\Delta E}\right)^2 \langle r^2 \rangle V_{zz} \tag{3.3}$$

The quantity λ is the spin-orbit coupling constant of Cr^{3+} in the crystal, ΔE is the energy separation between the ground state $^4S_{3/2}$ and first excited state $^4P_{3/2}$ (shown in Fig. 3.2), and $\langle r^2 \rangle$ is the average value of r^2 for the chromium 3d wave function. Carlin and Walker[5] measured ΔE using optical spectroscopy and obtained a value of 17,700 cm^{-1} for GAlSH, 17,550 cm^{-1} for GAlSeH, and 17,540 cm^{-1} for $AlCl_3.6H_2O$. These quoted measurements were obtained at 20 K. The values of ΔE for Rb and Cs sulfate alums have been measured at room temperature and they were found to be[1] 17,800 and 17,700 cm^{-1}, respectively. Equation 3.3 is approximate in that higher than fourth order terms in the crystal field potential and contributions of the higher excited states have been omitted. Covalency effects have also been neglected. In the derivation of Eq. 3.3 only the condition of a static crystal field was considered, and no account was made for the vibrational mechanism of the crystal. If the letter S is used to represent the static contribution, then Eq. 3.3 can be written as

$$D_S = \frac{3}{7} \left(\frac{\lambda}{\Delta E}\right)^2 \langle r^2 \rangle V_{zz}^{(S)} \tag{3.4}$$

In the experimental and theoretical pressure studies of Walsh[7,8], the effect of crystal vibrations at the paramagnetic ion site was treated as an additive contribution to the D parameter. That is the D parameter is written as

$$D = D_S + D_V \quad , \tag{3.5}$$

where D_V is the vibrational contribution to the zero-field splitting parameter. Walsh et al.[9] and Shrivastava[10] have found experimentally that this additive relationship also holds for other parameters of the spin Hamiltonian. Indeed, Shrivastava[42] has indicated that the relationship is applicable to all the fine structure parameters. It seems logical at this point to write the vibrational part of D in analogy to the static part given by Eq. 3.4, i.e., as

$$D_V = \text{const.}\ V_{zz}^{(V)} \quad , \tag{3.6}$$

where V indicates vibration. The validity of such a relation can be ascertained from the experimental results described in the following chapters.

The values of the spin Hamiltonian parameters vary with temperature and so the temperature dependence of Eq. 3.5 is

$$D(T) = D_S(T) + D_V(T) \quad . \tag{3.7}$$

The mathematical form of $D_S(T)$ and $D_V(T)$ is obtained by using the results of pressure studies as a guide.[9,10,11] It is observed in the separated curves of those studies that the form of $D_S(T)$ can be represented by a parabola while that of $D_V(T)$ as a hyperbolic cotangent. Shrivastava often used a Debye model to fit the vibrational part of the spin Hamiltonian parameters even though their temperature dependence had a hyperbolic cotangent form. In the case of four alums which he considered[13], a wide range of Debye temperatures were obtained and he concluded that the errors originated from the use of the Debye model. Shrivastava[43] was able to account for the ^{52}Cr, ^{53}Cr isotope effect of chromium impurities in axially symmetric sites in MgO in terms of the vibration of local impurity resonance modes. The vibrational contribution to the zero-field splitting parameter D of a given isotope was described by a function of the form $D = A \coth(\hbar\omega/2kT)$, where A is a constant and ω is the frequency of the impurity resonant mode. The hyperbolic cotangent was also used by Carlin and Walker[5] to account for the effect of vibrations on the optical transitions of Cr^{3+} in hydrated crystals.

Based on these experimental and theoretical studies we can write the crystal static distortion contribution to D in the parabolic form

$$D_S = D_S^o (1+\alpha T+\beta T^2).$$

In this equation D_S^o is the value of D_S at 0 K, T is the absolute temperature, and α and β are constants. The contribution to D due to lattice vibrations

is written as

$$D_V = D_V^\circ \coth (\theta/2T),$$

where D_V° is the value of D_V at 0 K, and $\theta = h\nu/k$ with ν being the frequency of the exciting vibration. The total D value is then given by

$$D = D_S^\circ(1+\alpha T+\beta T^2) + D_V^\circ \coth (\theta/2T). \tag{3.8}$$

3.14 Description of the Hyperfine Parameters A and B in the Spin Hamiltonian

The A and B parameters arise from the $\mathcal{H}_6$ term in the original Hamiltonian. McGarvey[44] obtained expressions for these by considering $\mathcal{H}_6$ in a first order perturbation calculation with the ligand orbitals included in the basic states. The calculations were based on a static crystal distortion and the following expressions were found

$$A = P\left[\frac{4}{21}(1 - 2a^2 + b^2) - K\right] \tag{3.9}$$

$$B = P\left[-\frac{2}{21}(1 - 2a^2 + b^2) - K\right] . \tag{3.10}$$

Here $P = -40 \times 10^{-4}$ cm^{-1} for $^{53}Cr^{3+}$. The first term in the square brackets arises from the electron-nuclear dipole-dipole interaction, while the K represents the contribution due to the Fermi contact term. For a site with octahedral symmetry of the coordinated ligands we have $a^2 = \frac{2}{3}$, $b^2 = \frac{1}{3}$, and $1 - 2a^2 + b^2 = 0$, giving A = B from Eqs. 3.9 and 3.10.

In this case, the hyperfine interaction is isotropic and is given by PK. If $a^2 < \frac{2}{3}$ and $b^2 > \frac{1}{3}$ then $1 - 2a^2 + b^2$ is positive and A<B. Experiments[45] show that the D parameter is negative for this case and the coordinated octahedron is trigonally compressed. If $a^2 > \frac{2}{3}$ and $b^2 < \frac{1}{3}$ then $1 - 2a^2 + b^2$ is negative, giving A>B. This case corresponds to a positive D and a trigonal extension of the octahedron.

3.15 Description of the Quadrupole Interaction Parameter Q' in the Spin Hamiltonian.

The nuclear quadrupole interaction parameter Q' arises from the $\mathcal{H}_7$ term in the original Hamiltonian. Bershon[46] has derived a relationship for Q' in terms of a static crystal distortion at the paramagnetic ion site. He found the relation

$$Q' = \frac{3eQ\, V_{zz}}{4I(2I-1)} \cdot (1-\gamma_\infty), \tag{3.11}$$

where eQ is the quadrupole moment of the paramagnetic ion's nucleus, V_{zz} is the electric field gradient external to the paramagnetic ion, and γ_∞ is the Sternheimer antishielding factor. For $^{53}Cr^{3+}$ Sternheimer[47] estimated a value of 12±1.0 for $1 - \gamma_\infty$. Hence for the chromium ion, with I = 3/2, Eq. 3.11 becomes

$$Q'_S = 3eQ\, V_{zz}^{(S)} \tag{3.12}$$

where the letter S stands for static.

Since both D_S and Q'_S are proportional to $V_{zz}^{(S)}$ then the electric field gradient can be eliminated to give the relation

$$Q'_S = k_S D_S \tag{3.13}$$

with

$$k_S = \frac{7eQ(\Delta E)^2(1-\gamma_\infty)}{4I(2I-1)\lambda^2 \langle r^2 \rangle} \tag{3.14}$$

The nature of the vibrational part of Q' can be ascertained from the experimental data of Q' and D which, when obtained for a large number of magnetic complexes of the same type, define a law of behavior operative in the crystals. Hence a discussion of this effect is best considered when the results are analyzed.

3.16 Description of the Nuclear g Value, g'_N, in the Spin Hamiltonian

In the nuclear Zeeman interaction the magnetic field seen by the nucleus is not simply the applied external magnetic field. The application of the field H causes the electronic wave functions to change by an amount proportional to H, and so the electronic field at the nucleus is modified. A consequence of this is paramagnetic shielding or anti-shielding. The magnetic shielding at the nucleus can be treated by substituting $\vec{H}(1+\sigma)$ for $\vec{H}$ in the normal nuclear Zeeman interaction term $\mathcal{H}_g = -g_N\beta_N\vec{H}\cdot\vec{I}$. This term then becomes $\mathcal{H}_g = -g_N\beta_N(1+\sigma)\vec{H}\cdot\vec{I}$, which can be written as $-g'_N\beta_N\vec{H}\cdot\vec{I}$ if $g'_N = g_N(1+\sigma)$. Geschwind[48] treated this problem theoretically and he obtained the following expression for σ:

$$\sigma = -5.84 \left\langle \frac{1}{r^3} \right\rangle_{a.u.} \cdot \frac{\Delta g}{\lambda (cm^{-1})} \qquad (3.15)$$

In this formula Δg is the electronic g-value shift from 2.0023, λ is the spin-orbit coupling parameter, and $\left\langle \frac{1}{r^3} \right\rangle$ is the average value of $\frac{1}{r^3}$ for the Cr^{3+} 3d orbital wave functions.

3.17 Line Shape and Line Intensity

Even though no study of line shapes was done in this work a brief description is given of their mechanism. The relative intensities of the ESR lines on the other hand are important in determining the sign of the zero-field splitting parameter D. There are two main causes giving rise to line broadening in paramagnetic resonance, namely the interaction between the paramagnetic ions and the lattice, and the interaction between the paramagnetic ions themselves. They are treated as relaxation effects characterized by the spin-lattice relaxation time τ and by the spin-spin relaxation time.

i) Spin-lattice interaction

The inverse of the spin-lattice relaxation time, $1/\tau$, is a measure of the rate at which a spin exchanges a quantum of energy with the lattice. Van Vleck[49] attributed this relaxation time to fluctuations of the crystalline electric field due to the thermal vibrations. The spin-orbit

coupling plays an essential role as the mechanism by which the spin of the paramagnetic ion feels the effect of the thermal vibrations. The spin-lattice relaxation time is temperature dependent, increasing with decreasing temperature. Also, τ depends importantly on the separation between the ground state and the first excited state, a large separation being associated with a long relaxation time τ. The spin-lattice interaction causes the spectral lines to be Lorentzian in shape.

ii) Spin-spin interaction

The broadening due to spin-spin interaction is temperature independent and may only be reduced by increasing the separation between the paramagnetic ions. The mechanism is as follows: Each ion is regarded as precessing about the external magnetic field direction, hence having a steady component along the field and a rotating component perpendicular to the field. The steady component sets up a magnetic field at neighbouring ion positions, and so those ions behave as if they were in a field of slightly different strength than the external field. The rotating component sets up a rotating field. If the rotating field has the same frequency as the other paramagnetic ions then there will be a couple acting on the steady component of the magnetic moment of the latter ion, tending to change its direction. The first process gives a broadening which is similar to that which arises from using an inhomogeneous magnetic field; while the second gives a resonance broadening because it

tends to reduce the lifetime of an ion in a given state. A spectral line broadened due to pure spin-spin interaction is Gaussian in shape.

iii) Line intensity

The intensity of a resonance line is proportional to the transition probability between two levels, to the population difference between the levels and to the concentration of the spins. The intensity of the resonance lines will change with temperature because of a re-distribution of the populations of the energy levels.

CHAPTER 4

EQUIPMENT

Two types of ESR spectrometers were used in the course of the studies. One was a commercial unit manufactured by Hilger and Watts Ltd., which was used to make ESR measurements at room temperature, solid carbon dioxide temperature, and liquid nitrogen temperature. For liquid helium temperature ESR and ENDOR measurements, a spectrometer with superheterodyne detection was used. This unit was previously assembled in this laboratory.[50] Both of the spectrometers operated at X-band microwave frequencies ($\sim 9.4_5$ GHz). The external magnetic field was produced by an 8 in. Newport magnet with a rotating base. Using 8 in. pole faces with a 3 in. gap, fields of up to 7 kG were easily obtainable. For higher fields, 4.5 in. pole faces with a 2 in. gap were used. The Hilger and Watts unit had an external magnetic field modulation of 100 kHz, which produced an a/c magnetic field component of approximately one gauss on the steady d/c field. This spectrometer employed a single klystron, and was of balanced bridge design. A Pound-type stabilizer was used to control the klystron frequency.

The superheterodyne spectrometer was operated with an external magnetic field modulation of 200 Hz. A block diagram showing the spectrometer components is given in Fig. 4.1, and a description of the system is as follows: A Varian X-band reflex klystron (i) produces the microwave power. This is followed by an isolator (ii). Part of the microwave power is fed

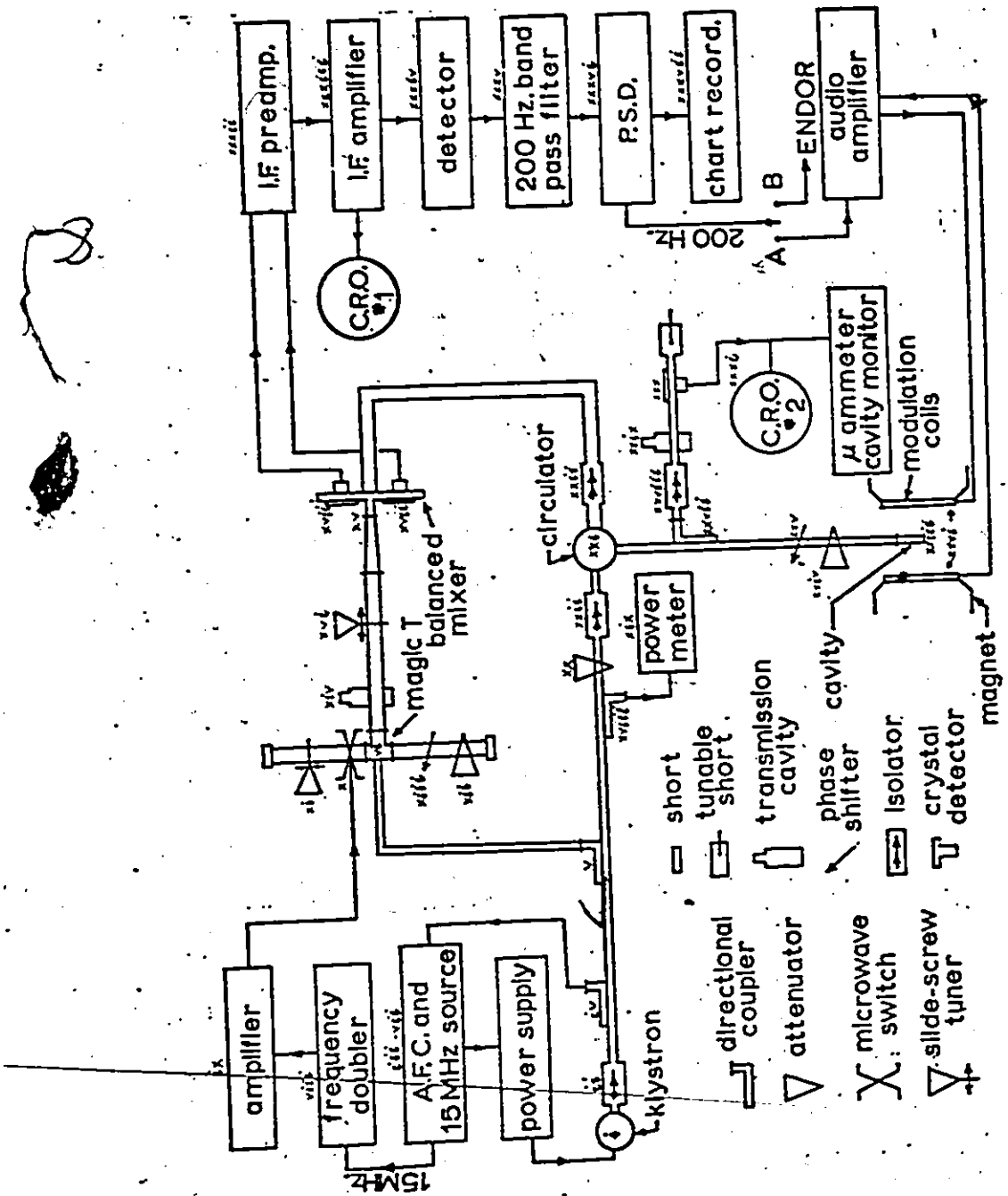

Fig. 4.1 Diagram of the Superheterodyne Spectrometer.

to the automatic frequency control (A.F.C.) unit (iii) via a directional coupler (iv). Part of the remaining microwave power is sent via the 10 db directional coupler (v) to the magic T (vi), and the rest is sent to the sample cavity (xxiii). A 15 MHz source (vii) produces power which is doubled in frequency by the doubler (viii) and amplified by the unit (ix). This 30 MHz power is then fed to a microwave switch (x) in one arm of the magic T (vi). The switch causes the microwave power in this arm to be amplitude modulated at 30 MHz. Hence sidebands are produced 30 MHz above and below the main microwave frequency. The amount of microwave power transmitted out of the magic T is controlled by a slide-screw tuner (xi), an attenuator (xii), and a phase shifter (xiii). One of the sidebands is selected by a transmission cavity (xiv) and fed to a second magic T (xv) via a slide-screw tuner (xvi). Crystal detectors (xvii) are carried on the arms of magic T (xv). Hence if the frequency of the main microwave power is ω_o, then the frequency of the power reaching the second magic T from the transmission cavity is ω_o + 30 MHz or ω_o - 30 MHz, depending on which sideband was selected.

The level of microwave power that was sent to the sample cavity (xxiii) can be read off the power meter (xix) via a 20 db directional coupler (xviii), on which is mounted a thermistor. The level of power sent to the cavity is controlled by a variable attenuator (xx), then fed to the cavity via a circulator (xxi). The cavity branch is isolated by two isolators (xxii) placed before and after the circulator. The amplitude and phase

of the microwave power reflected from the sample cavity is adjusted by an attenuator (xxiv) and a phase shifter (xxv). A portion of the reflected power is deviated by the directional coupler (xxvii) and passes through the isolator (xxviii), the calibrated reflection cavity (xxix), to the crystal detector (xxx). The reflection cavity is used to read off the value of the microwave frequency ω_o. The d/c level of the microwave power detected by the crystal detector is monitored on the oscilloscope (xxxi) and on a microammeter.

The microwave power that is reflected from the sample cavity through the circulator is of frequency ω_o, and it then mixes in the magic T (xv) (also called a balanced mixer) with the power of frequency $\omega_o \pm 30$ MHz mentioned above. The two balanced crystals detect the 30 MHz component of the mixed power, and this is carried to the 30 MHz I.F. amplifiers (xxxii) and (xxxiii).

In the process of detecting an ESR signal, the modulation coils (xxvi) connected to the magnet pole pieces are energized with 200 Hz power. This causes the d/c magnetic field to be modulated with a small a/c component. As the magnetic field is swept through a paramagnetic resonance in the crystal sample, the a/c magnetic field component causes the microwave power to be amplitude modulated at a frequency of 200 Hz. This effect is shown in Fig. 4.2. The amplitude of the power modulation varies as the magnetic field is swept through the resonance, and changes phase by 180° at the peak of the resonance. Hence at resonance, the microwave power

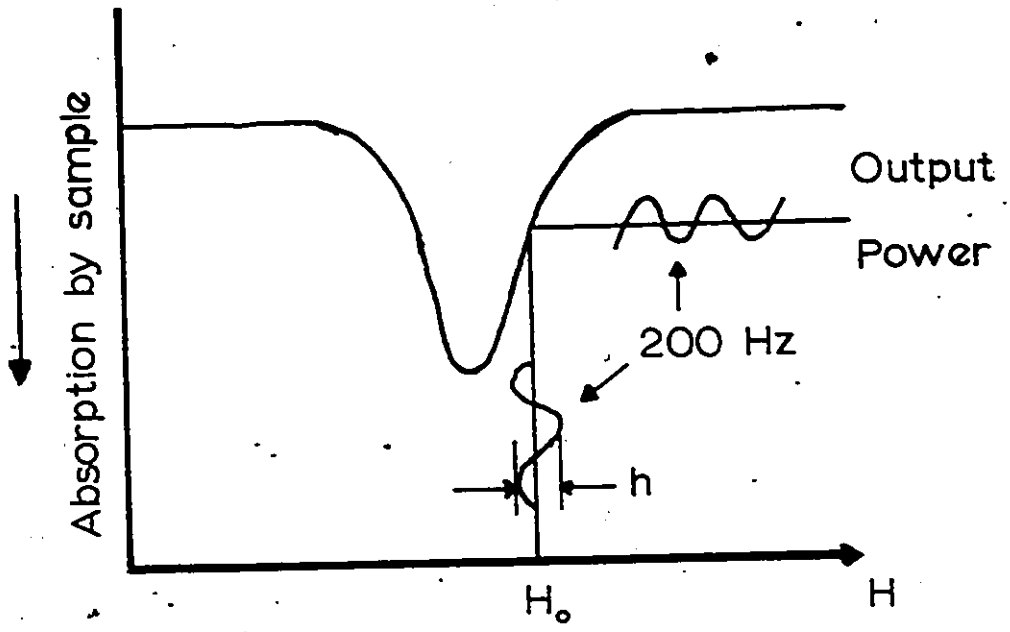

Fig. 4.2 Modulation Process of the Output Power

reflected from the cavity to the balanced mixer is modulated at 200 Hz. This causes the 30 MHz signals from the two crystals detectors (xvii) in the balanced mixer also to be modulated at 200 Hz. When the amplified 30 MHz signal reaches the detector (xxxiv), which is situated immediately after the I.F. amplifier, only the 200 Hz component passes through. This 200 Hz signal is fed through the band-pass filter (xxxv) to the phase-sensitive detector (xxxvi), and then to the chart recorder (xxxvii).

When performing ENDOR the modulation coils on the magnet pole pieces are de-energized and an external rf oscillator is frequency modulated at 200 Hz. The output of the oscillator is then fed to a two - or three - turn coil of wire which is wrapped around the sample. The arrangement of the ENDOR cavity and sample holder is shown in Fig. 4.3. A rectangular cavity operating in the TE_{014} mode is used. The matching screw located above the iris in Fig. 4.3 is used to match the cavity to the waveguide. The arrangement used for the sample and ENDOR coil positions maximizes the resonating Q value of the cavity. The loaded Q of the cavity was approximately 4,500 at 4.2 K. The magnetic field configurations at the sample in the cavity are shown in Fig. 4.4. In this figure, H_1 is the rf microwave magnetic field and H_2 is the rf field due to the power in the ENDOR coil. The external magnetic field H_o is parallel to the small sides of the cavity, and so all the magnetic fields H_o, H_1 and H_2 at the sample position are perpendicular to each other. This configuration produces the maximum ENDOR line intensities. When the power in the ENDOR

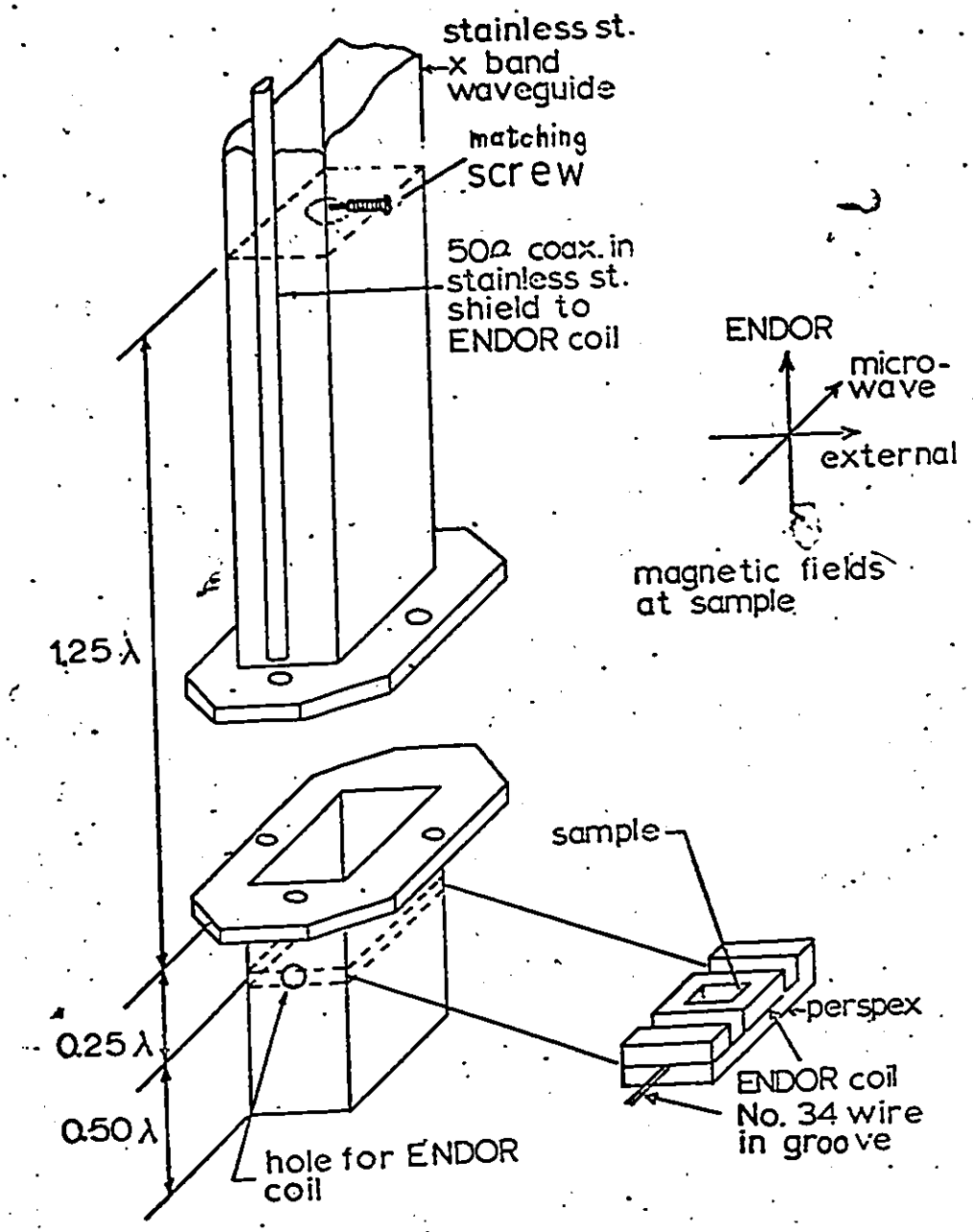

Fig. 4.3 ENDOR Microwave Cavity and Sample Holder

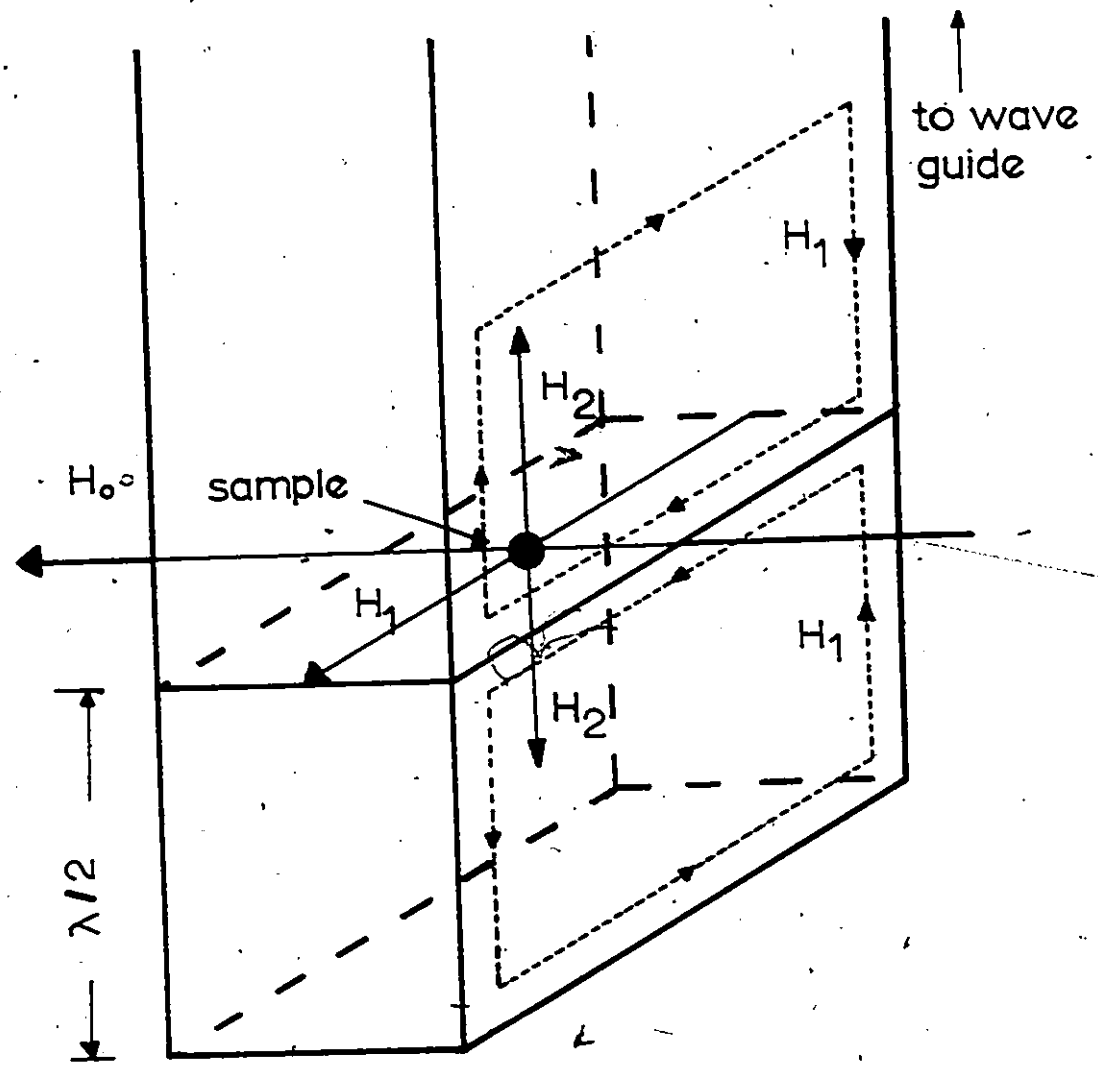

Fig. 4.4 Magnetic Field Configurations at the Sample in the Cavity.

coil is slowly swept in freqqancy through an ENDOR transition, the ENDOR signal is detected in the samemmanner as for the ESR signal described above.

Measurements of the external magnetic field were done using a nuclear magnetic resonance (NMR) spectrometer with a water sample (protons) probe. The accuracy achieved with this method is estimated to be ± 1 gauss. The frequency of the ENDOR power in the coil was measured with a Hewlett-Packard frequency counter, and the experimental accuracy was ±5 kHz. The microwave frequency was read off theccalibrated reflection cavity (or wave meter) with an accuracy of ± 1 MHz.

CHAPTER 5

EXPERIMENTAL MEASUREMENTS AND RESULTS

5.1 ESR of Cr^{3+} in the Guanidinium Salts

Prior to obtaining ENDOR measurements on the chromium ion it is necessary to make ESR measurements at 4.2 K so that the spin Hamiltonian parameters $g_{||}$, $g_{\perp}$ and D can be obtained. These parameters have not been previously obtained at 4.2 K in the guanidinium salts. While they have been obtained previously[23,24] at various elevated temperatures up to room temperature, it was thought desirable to obtain an independent set of D values so that smooth plots of D vs T could be made. The reason for this is that the plots play a central role in the interpretation of the resonance results, and it is important to obtain smooth plots over the whole temperature range between 4.2 and 297 K. The independent measurements insure that all the points were obtained in the same way, and the limits of error of the points and the subsequent curves can be known. Hence, in addition to the 4.2 K results, measurements of D were made at the boiling point of liquid nitrogen (77 K), the sublimation point of solid carbon dioxide (195 K), and at room temperature (297 K).

ESR measurements were made on the four guanidinium hexahydrate isomorphs termed GAlSH, GGaSH, GAlSeH and GGaSeH. As stated in Chapter 2, two sets of each crystal lightly doped with chromium were grown.

In one set the chromium was doped in its natural isotopic abundance, while in the other the dopant was the isotope $^{53}Cr^{3+}$ enriched to 94%. Two magnetic complexes of axial symmetry along the crystal c axis existed in each of the crystals at all temperatures between 4.2 and 297 K. The ESR lines in one complex have twice the intensity of the other because there are twice as many such $Cr^{3+}.6H_2O$ sites in the unit cell. Since the complexes have axial symmetry, magnetic field measurements of the spectral line positions were made when the external magnetic field was directed along the axial direction (z direction) and perpendicular to it (⊥ direction). Typical ESR spectra obtained in GAlSH at room temperature along the two directions are shown in Fig. 5.1 for chromium in its natural isotopic abundance. Part (a) of the figure gives the z axis spectrum while part (b) gives the perpendicular spectrum. ESR lines belonging to the magnetic complex with point group symmetry 3m are labeled G(1), while those with point group symmetry 3 are labeled G(2). The small lines flanking the main ESR fine structure lines are not studied in this work. Two interpretations of their origin have been given in the literature. Milsch and Brummer[51] attributed the lines to superhyperfine interaction of the Cr^{3+} ion with the ligand water protons, while Bates and Sczaniecki[52] attributed them to dipole-dipole interactions between pairs of chromium ions in the crystal.

With the exception of complex (1) in GAlSeH and GGaSeH at 4.2 K, the spectra observed in all the guanidinium crystals at the four

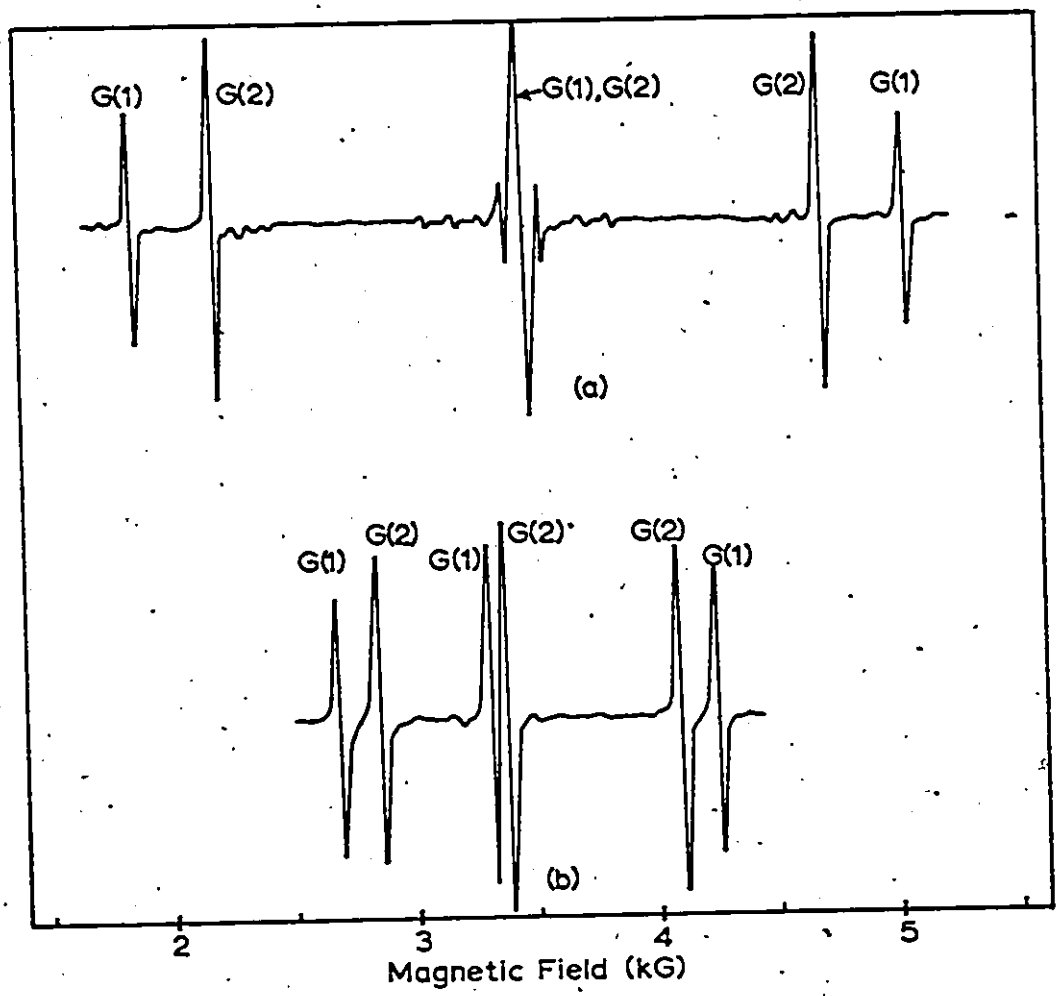

Fig. 5.1 ESR Spectra of GA1SH at Room Temperature.

(a) The Magnetic Field is Applied Along the Z Direction.

(b) The Magnetic Field is Applied Along a Perpendicular Direction.

temperatures considered are similar in appearance to that shown in Fig. 5.1. The above two cases are exceptions because the large zero-field splitting parameter D at 4.2 K for these complexes causes the resonance lines to be irregularly spaced or missing. The z and perpendicular axis spectra of Cr^{3+} in GAlSeH at 4.2 K are shown in Fig. 5.2 (a) and (b), respectively. It is observed in part (a) of Fig. 5.2 that the order of the two low field lines in the complexes (1) and (2) is reversed, while in part (b) it is observed that the central line of complex (1) is missing. The measured ESR line positions are listed in Tables 5.1 and 5.2. Measurements along the perpendicular direction were done at 4.2 K so as to obtain $g_\perp$ for the ENDOR calculations. Such measurements are not needed if only the zero-field splitting parameter D is required, and so no perpendicular direction measurements were made above 4.2 K.

The patterns of spectral lines obtained in the crystals containing enriched $^{53}Cr^{3+}$ were the same as described above for the Cr^{3+} in its natural isotopic abundance, except that now each fine-structure line was split into a group of four closely spaced hyperfine lines. The center of gravity positions of the $^{53}Cr^{3+}$ hyperfine groups along the z and perpendicular directions had the same magnetic field values as those given in Tables 5.1 and 5.2. Actually, more accuracy is attainable in the fine structure line positions with the chromium in its natural isotopic form because in this case the $^{52}Cr^{3+}$ isotope (84% abundance) produces large unsplit lines whose positions can be accurately measured. The crystals

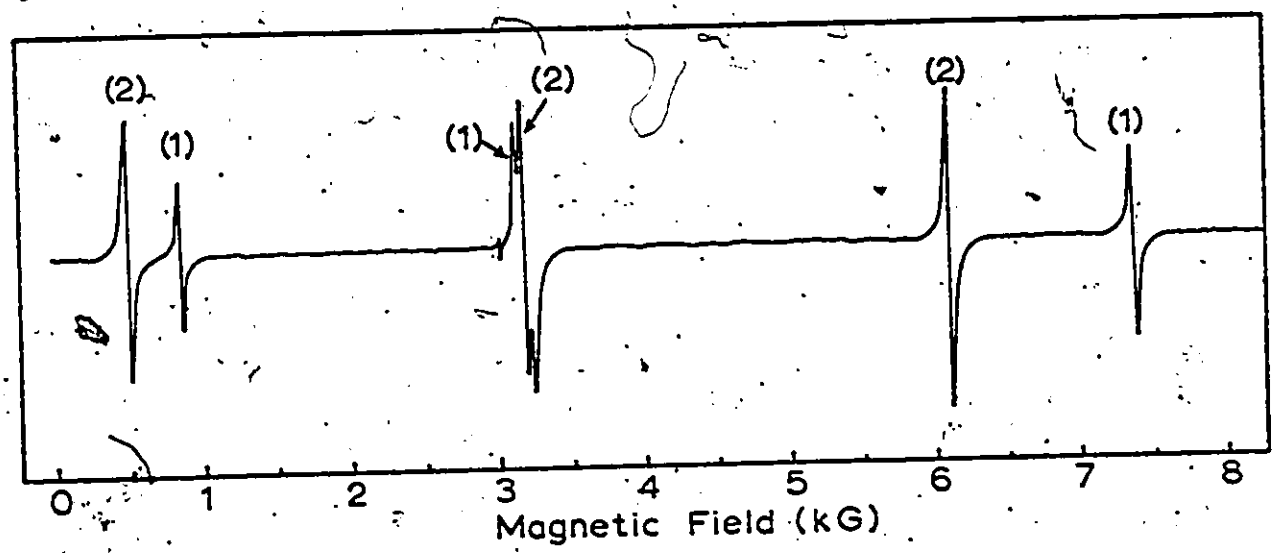

(a)

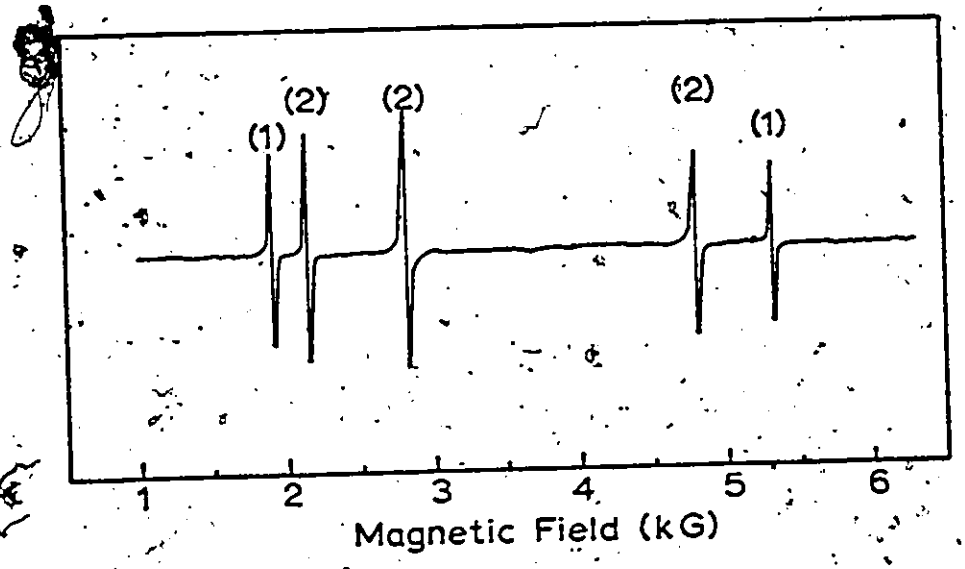

(b)

Fig. 5.2 ESR Spectra of GAlSeH at Helium Temperature.

(a) The Magnetic Field is Applied Along the Z Direction.

(b) The Magnetic Field is Applied Along a Perpendicular Direction.

TABLE 5.1 Magnetic Field Positions of the Cr^{3+} ESR Lines Along the Z Direction in the Guanidinium Salts (in units of kG).

SALT	4.2 K	77 K	195 K	277 K
GAlSH(1)	0.860	1.254	1.402	1.846
	3.367	3.612	3.386	3.445
	5.876	5.970	5.370	5.022
GAlSH(2)	1.439	1.794	1.846	2.185
	3.367	3.612	3.386	3.445
	5.305	5.430	4.926	4.686
GGaSH(1)	1.415	1.833	1.896	2.133
	3.374	3.679	3.417	3.376
	5.315	5.520	4.953	4.606
GGaSH(2)	1.867	2.266	2.232	2.400
	3.374	3.679	3.417	3.376
	4.871	5.069	4.600	4.350
GAlSeH(1)	0.805	*	*	0.399
	3.287	3.267	3.437	3.468
	7.411	7.191	6.898	6.457
GAlSeH(2)	0.439	0.500	0.899	1.117
	3.354	3.267	3.457	3.468
	6.192	6.033	5.980	5.761
GGaSeH(1)	0.384	*	*	0.225
	3.360	3.245	3.008	3.029
	7.118	6.887	6.196	5.808
GGaSeH(2)	0.755	0.764	0.695	0.876
	3.360	3.245	3.008	3.029
	5.994	5.813	5.347	5.152

* The field was too low to measure the line with the existing equipment.

TABLE 5.2 Magnetic Field Position of the Cr^{3+} ESR Lines Along a Perpendicular Direction in the Guanidinium Salts at 4.2 K (in units of kG).

SALTS	4.2 K
GAlSH(1)	2.241 3.144 4.593
GAlSH(2)	2.456 2.967 4.325
GGaSH(1)	2.454 3.148 4.335
GGaSH(2)	2.651 3.246 4.119
GAlSeH(1)	1.919 -- 5.328
GAlSeH(2)	2.137 2.825 4.771
GGaSeH(1)	1.956 — 5.174
GGaSeH(2)	2.203 3.220 4.665

containing enriched $^{53}Cr^{3+}$ are important, however, because the ENDOR measurements are done using them. Additionally, it was found desirable during the course of the work to measure the spacings between the ESR hyperfine lines at room temperature in crystals which showed good hyperfine line resolution. In the case of the guanidinium salts at this temperature, the GAlSeH crystal showed the best hyperfine line resolution. The resolution became poorer at low temperatures in these salts. The ESR spectrum of a typical group of hyperfine lines at room temperature along the z axis for $^{53}Cr^{3+}$ in GAlSH is shown in Fig. 5.3, and for GAlSeH in Fig. 5.4. Also shown in Fig. 5.4 is the spectrum of $AlCl_3.6H_2O$, which shows the best hyperfine line resolution of all the hydrated crystals considered in this work. The letters marked H_1, H_2 and H_3 in Fig. 5.3 refer to the magnetic field setting positions at which ENDOR measurements are made at 4.2 K. In Fig. 5.4, H' refers to the hyperfine spacing required in the room temperature ESR measurements. The positions of the end lines in the hyperfine group are obtained by measuring the line extremum values H_1 and H_2, the average of which will give the line center value. The ENDOR and room temperature hyperfine line measurements are described in the appropriate sections below.

5.2 ESR of Cr^{3+} in the Alums

Alums with two types of behaviors were studied; those which do not undergo low temperature phase transitions between 4.2 and 297 K, and those which do. The $Cr^{3+}.6H_2O$ magnetic complexes in the regular alums

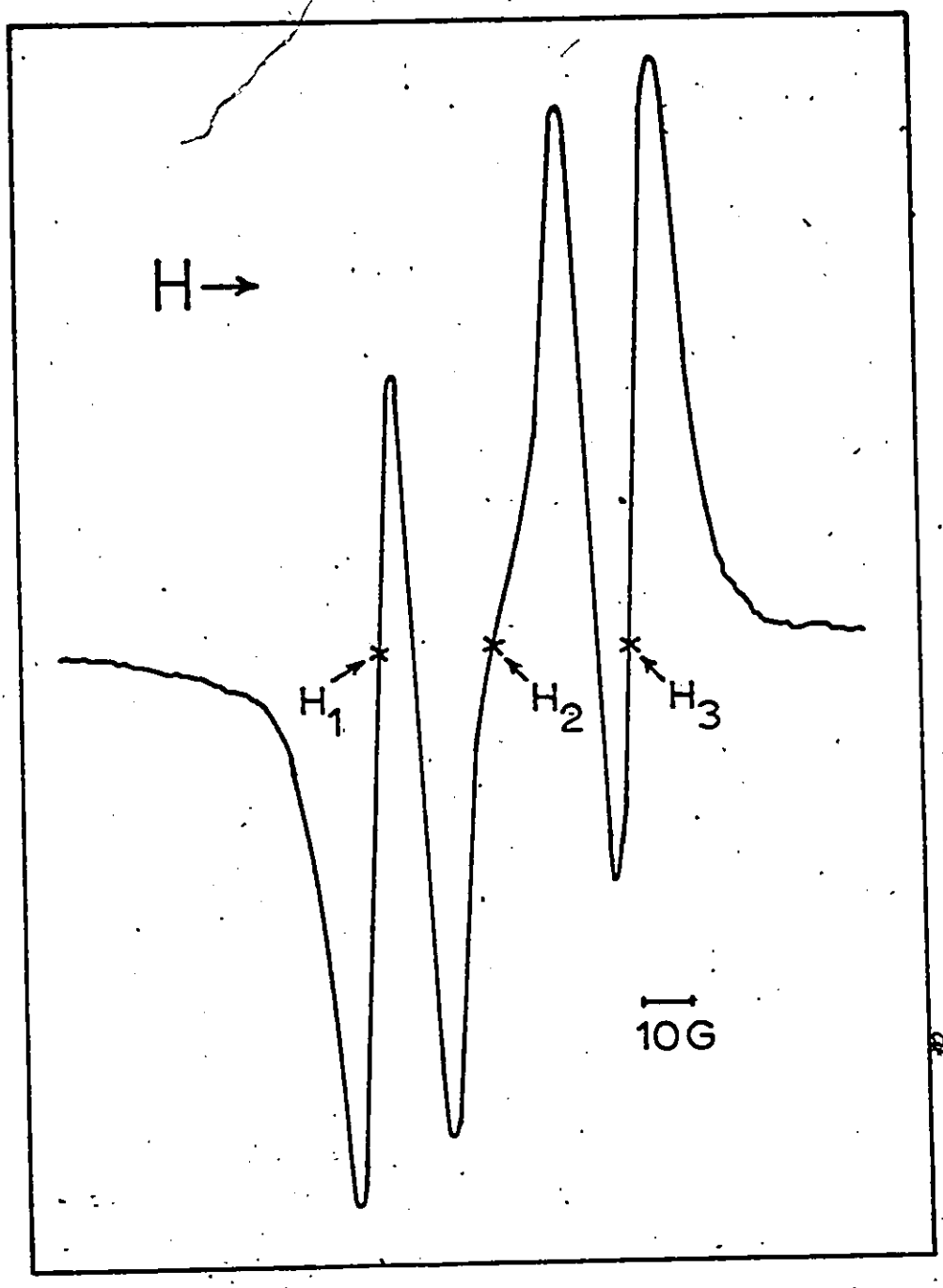

Fig. 5.3 ESR Hyperfine Lines at Room Temperature along the Z Direction for $^{53}Cr^{3+}$ in GAlSH.

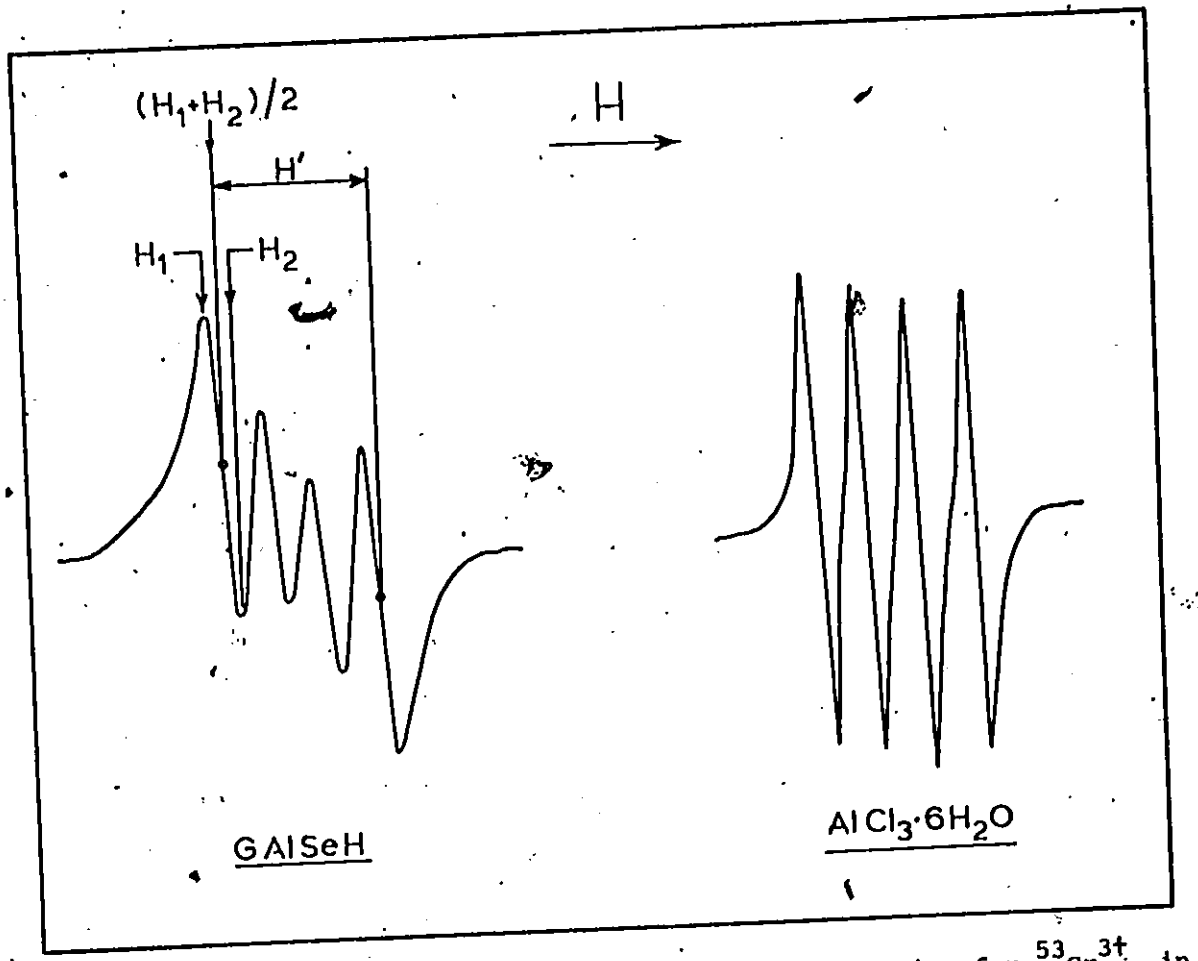

Fig. 5.4 ESR Hyperfine Lines at Room Temperature along the Z Direction for $^{53}Cr^{3+}$ in GAlSeH and in $AlCl_3.6H_2O$.

exhibited trigonal distortions in this temperature range. These alums are CsAl, CsGa, CsCr and CsIn sulfate alums; RbAl, RbGa and RbCr sulfate alums; TlAl and TlGa sulfate alums; and CsAl and CsGa selenate alums. The magnetic field positions of the spectral lines in these crystals along the z axis directions were measured at 4.2, 77, 195 and 297 K and the results are listed in Table 5.3. No measurements were made at 4.2 K in TlAl alum because the ESR lines were too broad and too close together, hence causing the magnetic field positions of the lines to be obscured. Typical chart recordings of the ESR spectra in alums for Cr^{3+} in trigonally distorted sites have been given previously.[50] The NH_4 and K sulfate alums undergo low temperature phase transitions. Below the transition temperatures the $Cr^{3+}.6H_2O$ magnetic complexes change from trigonal to rhombic symmetry. The magnetic field positions of the spectral lines along the z directions, above the transition temperatures, for NH_4Al, NH_4Ga, KAl and KGa sulfate alums are listed in Table 5.3. Also listed in the table are the results for NH_4In sulfate alum above and below the phase transition temperature. The results obtained below the transition in this crystal are only approximate in that the measurements were made with the magnetic field directed along the crystal [111] direction, even though the z axis of the magnetic complex is displaced slightly away from this direction. The approximate values are sufficient to give a description of the behavior of the $Cr^{3+}.6H_2O$ magnetic complexes in the crystal below the phase transition temperature.

TABLE 5.3 Magnetic Field Positions of the Cr^{3+} ESR Lines Along the Z Direction in Alums (in units of kG)

ALUM	TEMPERATURE (K) 4.2	77	195	297
CsAl (sulfate)	1.805 4.905	1.704 4.840	1.782 5.010	1.782 5.082
CsGa "	1.954 4.820	1.806 4.702	1.887 4.911	1.876 5.000
CsCr "	2.016 4.846	1.851 4.669	1.930 4.876	1.954 5.034
CsIn "	2.223 4.516	2.097 4.446	2.180 4.676	2.134 4.762
RbAl "	2.628 4.144	2.513 4.041	2.375 4.435	1.969 4.925
RbGa "	2.224 4.480	2.135 4.415	1.989 4.789	1.614 5.194
RbCr "	2.226 4.605	2.099 4.551	1.960 4.835	1.609 5.245
TlAl "		2.693 4.079	2.399 4.384	1.960 4.922
TlGa "	2.428 3.363 4.351	2.308 4.234	1.990 4.780	1.527 5.266
CsAl (selenate)	2.147 3.375 4.604	2.058 4.493	2.117 4.750	1.994 4.915
CsGa "	1.801 3.362 4.925	1.691 4.809	1.829 5.075	1.695 5.194
NH_4Al (sulfate)		3.184 3.356	2.913 3.922	2.392 4.495
NH_4Ga "			2.526 4.278	1.996 4.884
NH_4In "	2.716 3.994	2.593 3.923	2.495 4.335	1.941 4.948
KAl "			3.268 3.492	2.589 4.280
KGa "			2.792 3.818	2.129 4.752

5.3 Calculation of the D Parameter

When the hyperfine structure matrix elements are put equal to zero in Figs. 3.3 and 3.4, then the 16 x 16 matrices reduce to 4 x 4 matrices which describe the fine structure spectra in the z and perpendicular directions. The diagonalized 4 x 4 matrices can be solved to give expressions for the magnetic field positions of the Cr^{3+} ESR fine structure lines. The expressions for the z direction are

$$H_1 \quad (\tfrac{3}{2} \leftrightarrow \tfrac{1}{2}) \quad = H_{o||} - 2D \tag{5.1}$$

$$H_2 \quad (\tfrac{1}{2} \leftrightarrow -\tfrac{1}{2}) \quad = H_{o||} \tag{5.2}$$

$$H_3 \quad (-\tfrac{1}{2} \leftrightarrow -\tfrac{3}{2}) = H_{o||} + 2D, \tag{5.3}$$

and for the perpendicular direction are

$$H_1(\tfrac{3}{2} \leftrightarrow \tfrac{1}{2}) \quad = H_{o\perp} - (H_1^2 - H_1 D + D^2)^{\frac{1}{2}} + (H_1^2 + H_1 D + D^2)^{\frac{1}{2}} \tag{5.4}$$

$$H_2(\tfrac{1}{2} \leftrightarrow -\tfrac{1}{2}) \quad = H_{o\perp} + (H_2^2 + H_2 D + D^2)^{\frac{1}{2}} + (H_2^2 - H_2 D + D^2)^{\frac{1}{2}} \tag{5.5}$$

$$H_3(-\tfrac{1}{2} \leftrightarrow -\tfrac{3}{2}) = H_{o\perp} + (H_3^2 - H_3 D + D^2)^{\frac{1}{2}} - (H_3^2 + H_3 D + D^2)^{\frac{1}{2}} \tag{5.6}$$

In Eqs. 5.1 to 5.3, $H_{o||} = h\nu_o/g_{||}\beta$ with ν_o being the microwave frequency and $g_{||}$ being the Cr^{3+} electronic g value along the z direction. H_1, H_2 and H_3 are the low, central, and high field positions, respectively,

of the ESR lines for positive D. In eqs. 5.4 to 5.6, $H_{o\perp} = h\nu_o/g_\perp\beta$ with $g_\perp$ being the Cr^{3+} electronic g value along a perpendicular direction. H_1, H_2 and H_3 are the high, central, and low field positions, respectively, of the ESR lines for positive D. Each of the equations 5.4 - 5.6 can be used to find $g_\perp$ when the value of D found from the z axis equations is substituted into them, but it is difficult to find D from them without the use of a computer. As seen in Eqs. 5.1 - 5.3, the D value can be calculated simply from the measured positions of the high and low field ESR lines. The central line then gives a check to the $g_{||}$ value. In cases where the low field line along the z axis could not be measured, then the central and high field lines are used in the calculations. The calculated values of D are given in Tables 5.4 and 5.5. The results for the concentrated K and NH_4 chromic alums and $AlCl_3.6H_2O$, which were determined by others, are also included in the tables. The results are given in units of 10^{-4} cm^{-1}. The g values of all the chromium magnetic complexes were found to lie within the range $g = 1.975 \pm 0.005$. To transfer from units of kG to cm^{-1} a factor of 10.8491 kG/cm^{-1} was used for the alums and 10.8349 kG/cm^{-1} for the guanidinium salts. The conversion factors depend on the g values measured in the salts and on the relation $h\nu = g\beta H$.

The sign of the D parameter can be obtained by comparing the relative intensities of the low and high field ESR lines at room and liquid helium temperatures. This effect can be illustrated with the aid of Fig. 5.5. When the D parameter is positive the relative magnitude of the high field line to the low field line will increase at lower

TABLE 5.4 Spin Hamiltonian D Parameter at Given Temperatures for Cr^{3+} in Trigonally Distorted $Cr^{3+}.6H_2O$ Complexes (unit of D is $10^{-4}cm^{-1}$).

Crystal	4.2 K	77 K	195 K	297 K
RbAl sulfate alum	349 ± 5	348 ± 5	474 ± 5	681 ± 5
RbGa " "	518	525	645	824
RbCr " "	567	565	663	838
TlGa " "	442	444	643	862
TlAl " "	-	320	457	683
CsAl " "	-715	-723	-744	-762
CsGa " "	-660	-667	-697	-719
CsCr " "	-652	-649	-679	-710
CsIn " "	-528	-541	-575	-606
CsAl selenate alum	565	562	607	673
CsGa " "	720	719	748	806
GAlSH(2)	-889	-889	-712	-577
GAlSH(1)	-1,155	-1,088	-915	-733
GGaSH(2)	-695	-651	-547	-450
GGaSH(1)	-898	-851	-705	-570
GAlSeH(2)	-1,327	-1,277	-1,172	-1,071
GAlSeH(1)	-1,880	-1,810	-1,597	-1,398
GGaSeH(2)	-1,211	-1,165	-1,073	-986
GGaSeH(1)	-1,735	-1,681	-1,471	-1,288
$AlCl_3.6H_2O$[a]	-341	-338	-337	-326

[a] Pack and Manoogian, Ref. 3.

TABLE 5.5 D Values of Cr^{3+} in Ammonium and Potassium Sulfate Alums Measured above the Phase Transition Temperatures. NH_4In Alum is an Exception in that the Values at 4.2 and 77 K are Measured below the Transition Temperature.

Unit of D is $10^{-4}cm^{-1}$ and the error is ± 5 $(10^{-4}cm^{-1})$.

Crystal	4.2 K	77 K	195 K	297 K
NH_4Cr	----	175[a]	425[b]	675[c]
NH_4Ga	----	----	404	665
NH_4Al	----	-40	232	485
NH_4In	294[d]	307[d]	424	693
KCr	----	----	275[b]	600[c]
KGa	----	----	236	604
KAl	----	----	35	390

[a] Bleaney, Ref. 30. Measurement made at 90 K.

[b] Bleaney, Ref. 30. Measurement made at 193 K.

[c] Bagguley and Griffiths, Ref. 53. Measurement made at 290 K.

[d] Approximate value obtained below the transition temperature. Measurements were made along a crystal [111] direction even though the z axes are displaced slightly from this direction.

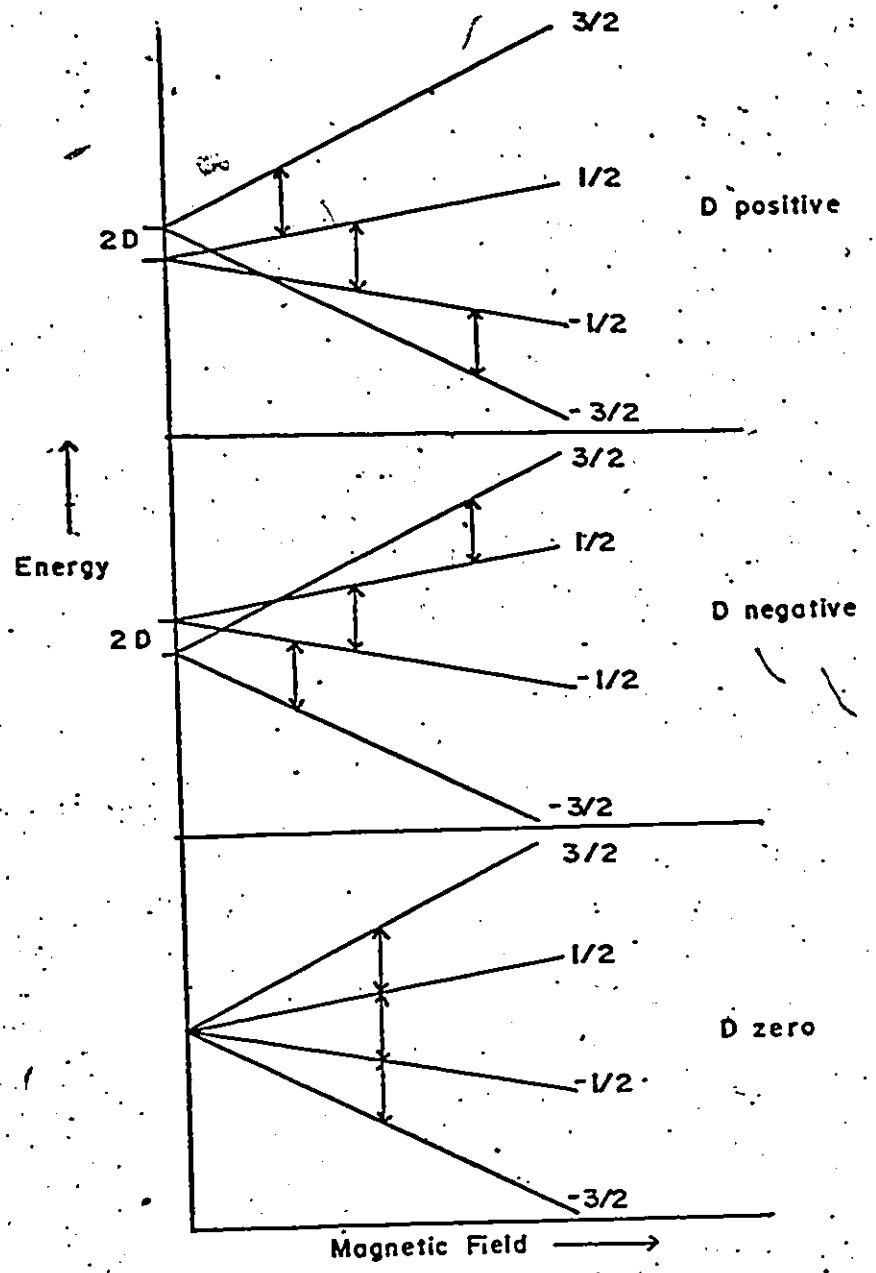

Fig. 5.5 Zeeman Splitting of a $^4S_{3/2}$ State for D Positive, D Negative and D = 0.

temperatures because the difference in population of the $M_S = -3/2 \leftrightarrow -1/2$ transition increases over that of the $M_S = 3/2 \leftrightarrow 1/2$. When D is negative it is the low field line which connects with the more populated $M_S = -3/2$ state, and so the relative magnitude of the low field ground state transition will increase over that of the high field transition with lowering temperature. The sign of D can also be determined from the ENDOR analysis because only the correct sign will give a satisfactory fit to the double resonance data.

The ground state fine-structure energy level diagrams of Cr^{3+} in the magnetic complex GAlSH(1), for the magnetic field along the z and a perpendicular direction, are shown in Fig. 5.6(a) and (b) respectively. Also shown in the figure are the observed ESR transitions. These diagrams are typical for the two types of chromium magnetic complexes in all the GAlSH isomorphs in the temperature range 4.2 and 297 K, with the exception of GAlSeH(1) and GGaSeH(1) at 4.2 K. They are also typical for the trigonally distorted chromium magnetic complexes in the alums which have a negative D, and in $AlCl_3.6H_2O$. For the case of positive D alums the diagrams in Fig. 5.6 are inverted. For the large D parameter of the chromium complex in GAlSeH(1) at 4.2 K, the energy level diagrams along the z and a perpendicular direction are shown in Figs. 5.7 and 5.8, respectively. It is observed in Fig. 5.7 that the low field ESR line is between the same states $M_S = 3/2 \leftrightarrow 1/2$ as is the high field line. It is important to take cognizance of this feature when the ENDOR results

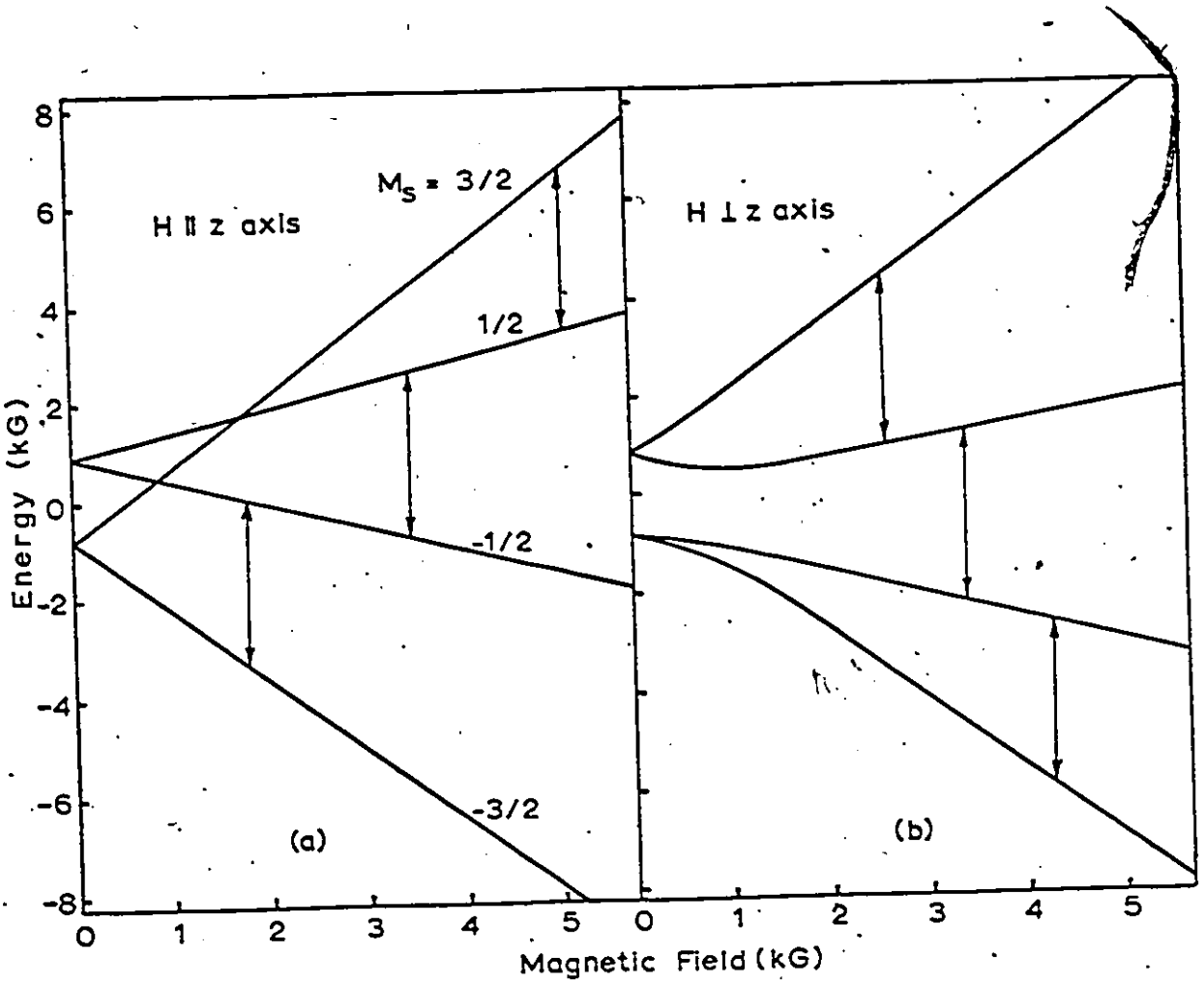

Fig. 5.6 Ground State Fine-Structure Energy Level Diagrams of Cr^{3+} in the Magnetic Complex GALSH(1).

(a) Diagram for the Magnetic Field along the Z Direction

(b) Diagram for the Magnetic Field along a Perpendicular Direction.

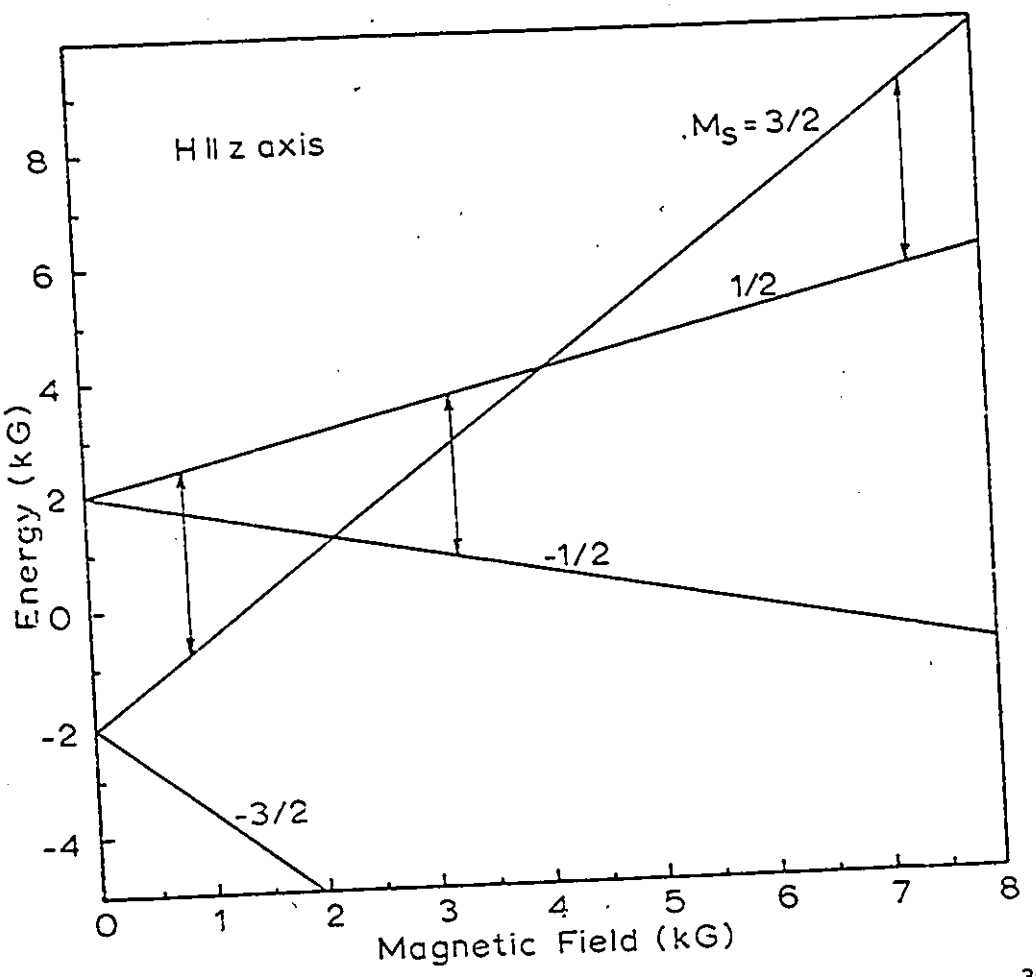

Fig. 5.7 Ground State Fine Structure Energy Level Diagram of Cr^{3+} in the Magnetic Complex GAlSeH(1) at 4.2 K with the Magnetic Field along the Z Direction.

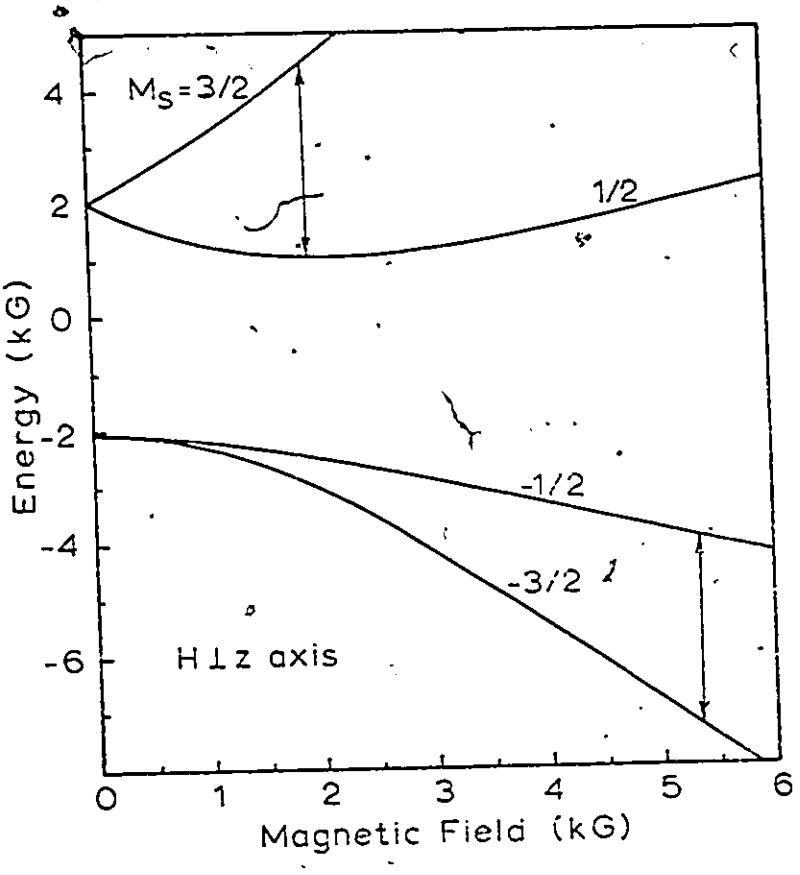

Fig. 5.8 Ground State Fine Structure Energy Level Diagram of Cr^{3+} in the Magnetic Complex GAlSeH(1) at 4.2 K with the Magnetic Field along a Perpendicular Direction.

are fitted to the spin Hamiltonian. In Fig. 5.8 it is observed that the central $M_S = 1/2 \rightarrow -1/2$ transition is missing because of the large D value. For the chromium complex in GGaSeH the z axis energy level diagram is similar to that of Fig. 5.7.

5.4 ENDOR Measurements

ENDOR measurements were done at 4.2 K on the two inequivalent magnetic complexes of $^{53}Cr^{3+}$ in each of the four guanidinium isomorphs GAlSH, GGaSH, GAlSeH and GGaSeH; and in the TlGa, CsIn sulfate alums and CsAl,CsGa selenate alums. In each case measurements were taken along the z and a perpendicular direction. ENDOR readings were obtained for the hyperfine transitions in the $M_S = \pm 3/2$ spin states, and these occur in the 75 MHz frequency region. The results are tabulated in Tables 5.6 to 5.17. For a given magnetic field setting the frequencies of only the two lines with the greatest intensities were measured. The third line is obtained with greater accuracy at a slightly different magnetic field setting.

The ENDOR spectra obtained in GAlSH(1) along the z axis for the low field group of hyperfine lines are shown in Fig. 5.9. The spectra (a), (b) and (c) were obtained when the magnetic field was set at the ESR hyperfine line positions marked H_1, H_2 and H_3 respectively, in Fig. 5.3. The corresponding ENDOR spectra obtained for the z axis high field group of ESR hyperfine lines are shown in Fig. 5.10. The resolution of the ENDOR lines was sufficient to measure them with an accuracy of ±5kHz.

TABLE 5.6 ENDOR Frequencies of $^{53}Cr^{3+}$ in GA1SH(1).

$\vec{H}_z$				$\vec{H}_\perp$			
MAGNETIC FIELD kG (± 1G)	MEASURED MHz (±5kHz)	CALCULATED MHz	DIFFERENCE	MAGNETIC FIELD kG(± 1G)	MEASURED MHz(±5kHz)	CALCULATED MHz	DIFFERENCE
0.841	75.394	75.406	-.012	2.219	74.418	74.421	-.003
	76.854	76.853	+.001		75.326	75.321	+.005
	------	78.313	-----		------	76.232	------
0.863	75.386	75.406	-.020	2.241	74.476	74.479	-.003
	76.841	76.842	-.001		75.378	75.382	-.004
	78.301	78.305	-.004		76.282	76.282	+.000
0.885	------	75.401	-----	2.262	------	74.537	------
	76.841	76.837	+.004		75.418	75.421	-.003
	78.294	78.295	-.001		76.331	76.332	-.001
5.849	------	77.460	-----	4.570	------	75.590	------
	78.052	78.033	+.019		------	75.667	------
	78.616	78.606	+.010		75.715	75.746	-.031
5.874	77.480	77.468	+.012	4.594	------	75.590	------
	78.035	78.038	-.003		75.650	75.667	-.017
	78.610	78.617	-.007		------	75.775	------
5.894	77.456	77.471	-.015	4.616	75.627	75.596	+.031
	78.043	78.046	-.003		------	75.699	------
	78.592	78.625	-.033		------	75.775	------

TABLE 5.7 ENDOR Frequencies of $^{53}Cr^{3+}$ in GAlSH(2)

$\vec{H}$ z				$\vec{H} \perp$			
MAGNETIC FIELD kG (±1G)	MEASURED MHz (±5kHz)	CALCULATED MHz	DIFFERENCE	MAGNETIC FIELD kG (±1G)	MEASURED MHz (±5kHz)	CALCULATED MHz	DIFFERENCE
1.417	75.241	75.254	-.013	2.437	75.803	75.790	+.013
	76.794	76.820	-.026		76.772	76.751	+.021
	------	78.377	-----		------	77.739	-----
1.440	75.241	75.251	-.010	2.452	75.826	75.819	+.007
	76.794	76.809	-.013		76.794	76.780	+.014
	78.362	78.370	-.008		77.756	77.763	-.007
1.464	------	75.246	-----	2.480	-------	75.856	-----
	76.792	76.806	-.014		76.829	76.836	-.007
	78.345	78.357	-.012		77.793	77.797	-.004
5.276	------	77.314	-----	4.299	------	76.229	-----
	77.972	77.990	-.018		76.366	76.368	-.002
	78.658	78.676	-.016		76.477	76.508	-.031
5.289	77.316	77.314	+.002	4.327	76.243	76.234	+.009
	77.994	77.997	-.003		76.325	76.379	-.054
	78.666	78.679	-.013		76.399	76.516	-.117
5.311	77.314	77.319	-.005	4.350	76.273	76.236	+.037
	78.002	78.000	+.002		------	76.392	-----
	------	78.689	-----		------	76.519	-----

TABLE 5.8 ENDOR Frequencies of $^{53}Cr^{3+}$ in GGaSH(1)

$\vec{H} \cdot z$				$\vec{H} \perp$			
MAGNETIC FIELD kG (± 1G)	MEASURED MHz (±5kHz)	CALCULATED MHz	DIFFERENCE	MAGNETIC FIELD kG (± 1G)	MEASURED MHz (±5kHz)	CALCULATED MHz	DIFFERENCE
1.390	75.391	75.396	-.005	2.425	75.803	75.796	+.007
	76.869	76.885	-.016		------	76.716	-----
	------	78.368	-----		------	77.670	-----
1.405	75.392	75.393	-.001	2.447	75.834	75.833	+.001
	76.876	76.877	-.001		76.752	76.763	-.011
	78.366	78.363	+.003		------	77.694	-----
1.425	------	75.390	-----	2.463	------	75.862	-----
	76.874	76.871	+.003		76.784	76.787	-.003
	78.361	78.358	+.003		77.709	77.715	-.006
1.441	------	75.388	-----	2.482	------	75.891	-----
	76.864	76.866	-.002		------	76.819	-----
	78.352	78.347	+.005		77.734	77.746	-.012
5.290	------	77.460	-----	4.307	------	76.260	-----
	------	78.052	-----		------	76.355	-----
	78.661	78.662	-.001		76.448	76.455	-.007
5.304	------	77.458	-----	4.323	------	76.271	-----
	78.062	78.060	+.002		76.349	76.358	-.009
	78.660	78.667	-.007		76.466	76.458	+.008
5.324	77.468	77.466	+.002	4.348	76.279	76.268	+.011
	78.060	78.062	-.002		76.404	76.368	+.036
	78.667	78.675	-.008		------	76.476	-----
5.343	77.465	77.468	-.003	4.364	76.316	76.276	+.040
	78.066	78.065	+.001		------	76.374	-----
	------	78.685	-----		------	76.471	-----

TABLE 5.9 ENDOR Frequencies of $^{53}Cr^{3+}$ in GGaSH(2)

$\vec{H}$ z				$\vec{H} \perp$			
MAGNETIC FIELD kG (±1G)	MEASURED MHz(± 5kHz)	CALCULATED MHz	DIFFERENCE	MAGNETIC FIELD kG (±1G)	MEASURED MHz (± 5kHz)	CALCULATED MHz	DIFFERENCE
1.840	75.256	75.267	-.011	2.615	76.653	76.646	+.007
	------	76.836	-----		------	77.623	-----
	------	78.397	-----		------	78.605	-----
1.855	75.256	75.269	-.013	2.641	76.680	76.678	-.010
	76.828	76.828	+.000		77.652	77.649	+.003
	------	78.392	-----		------	78.628	-----
1.876	75.248	75.259	-.011	2.663	------	76.704	-----
	76.815	76.823	-.008		77.672	77.670	+.002
	78.395	78.382	+.013		78.644	78.655	-.011
1.895	------	75.261	-----	2.686	------	76.723	-----
	76.813	76.815	-.002		------	77.702	-----
	78.383	78.376	+.007		78.665	78.676	-.011
4.845	------	77.324	-----	4.090	------	76.722	-----
	------	78.002	-----		------	76.846	-----
	78.699	78.682	+.017		76.982	76.983	-.001
4.861	------	77.327	-----	4.109	------	76.715	-----
	78.013	78.004	+.009		76.861	76.851	+.010
	78.690	78.690	+.000		76.962	76.994	-.032
4.878	77.330	77.329	+.001	4.129	76.742	76.714	+.028
	78.004	78.010	-.006		76.847	76.851	-.004
	78.704	78.698	+.006		------	76.999	-----
4.900	77.321	77.331	-.010	4.146	76.732	76.717	+.015
	78.016	78.018	-.002		------	76.859	-----
	------	78.706	-----		------	76.996	-----

TABLE 5.10 ENDOR Frequencies of $^{53}Cr^{3+}$ in GAlSeH(1)

$\vec{H}z$

MAGNETIC FIELD kG (±1G)	MEASURED MHz (±5kHz)	CALCULATED MHz	DIFFERENCE
0.739	--------	75.485	-------
	76.942	76.940	+.002
	78.397	78.398	-.001
0.754	75.482	75.489	-.007
	76.946	76.941	+.005
	------	78.406	-----
0.775	75.488	75.493	-.005
	76.952	76.948	+.004
	------	78.415	-----
0.793	75.491	75.497	-.006
	77.039	76.954	+.085
	------	78.424	-----

$\vec{H} \perp$

MAGNETIC FIELD kG (±1G)	MEASURED MHz (±5kHz)	CALCULATED MHz	DIFFERENCE
1.891	70.357	70.358	-.001
	------	71.241	-----
	------	72.092	-----
1.907	70.449	70.437	+.012
	71.308	71.309	-.001
	------	72.171	-----
1.929	70.530	70.540	-.010
	71.400	71.399	+.001
	72.259	72.263	-.004
1.948	------	70.619	-----
	71.476	71.481	-.005
	72.344	72.345	-.001
5.299	------	73.433	-----
	------	73.533	-----
	73.586	73.612	-.026
5.312	------	73.454	-----
	73.532	73.549	-.017
	73.614	73.636	-.022
5.327	73.492	73.472	+.020
	73.574	73.562	+.012
	------	73.665	-----
5.347	73.521	73.483	+.038
	------	73.602	-----
	------	73.694	-----

TABLE 5.11 ENDOR Frequencies of $^{53}Cr^{3+}$ in GaSeH(2)

$\vec{H}z$				$\vec{H} \perp$			
MAGNETIC FIELD kG (±1G)	MEASURED MHz (±5kHz)	CALCULATED MHz	DIFFERENCE	MAGNETIC FIELD kG (± 1G)	MEASURED (MHz (±5kHz)	CALCULATED MHz	DIFFERENCE
0.459	75.188	75.183	+.005	2.108	73.438	73.436	+.002
	76.848	76.853	-.005		74.457	74.450	+.007
	78.521	78.526	-.005		------	75.459	-----
0.474	75.180	75.180	+.000	2.128	73.498	73.499	-.001
	76.847	76.848	-.001		74.509	74.511	-.002
	78.518	78.521	-.003		75.500	75.520	-.020
0.497	75.188	75.180	+.008	2.148	73.568	73.565	+.003
	76.839	76.837	+.002		74.543	74.569	-.026
	78.512	78.510	+.002		75.539	75.580	-.041
0.505	75.177	75.177	-.000	2.163	73.607	73.612	-.005
	76.841	76.835	+.006		74.604	74.619	-.015
	78.510	78.508	+.002		75.629	75.620	+.009
6.233	-----	77.248	-----	4.743	------	75.122	-----
	78.037	78.028	+.001		------	75.301	-----
	78.809	78.821	-.012		75.477	75.507	-.030
6.252	------	77.254	-----	4.767	75.138	75.130	+.008
	78.037	78.036	+.001		75.322	75.320	+.002
	78.818	78.829	-.011		75.495	75.528	-.033
6.270	77.270	77.256	+.014	4.777	75.166	75.135	+.031
	78.043	78.044	-.001		75.337	75.335	+.002
	78.825	78.834	-.009		75.518	75.536	-.018
6.287	77.288	77.264	+.024	4.798	75.177	75.159	+.018
	78.070	78.044	+.026		------	75.349	-----
	78.872	78.845	+.027		------	75.554	-----

TABLE 5.12 ENDOR Frequencies of $^{53}Cr^{3+}$ in GGaSeH(1)

$\vec{H}z$				$\vec{H} \perp$			
MAGNETIC FIELD kG (± 1G)	MEASURED MHz (±5kHz)	CALCULATED MHz	DIFFERENCE	MAGNETIC FIELD kG (± 1G)	MEASURED MHz (±5kHz)	CALCULATED MHz	DIFFERENCE
0.371	75.536	75.542	-.006	1.940	71.278	71.277	+.001
	76.984	76.985	-.001		72.219	72.139	+.080
	78.433	78.424	+.009		------	73.032	-----
0.375	75.533	75.544	-.011	1.964	71.329	71.374	-.045
	76.984	76.985	-.001		72.238	72.244	-.006
	78.432	78.427	-.005		73.128	73.120	-.008
0.406	75.536	75.540	-.014	1.993	------	71.488	-----
	76.985	76.993	-.008		72.286	72.366	-.080
	78.437	78.440	-.003		73.208	73.236	-.028
7.094	77.648	77.615	+.033	5.138	------	73.998	-----
	78.184	78.165	+.019		------	74.074	-----
	78.732	78.733	-.001		74.133	74.164	-.031
7.113	77.636	77.617	+.019	5.174	------	74.032	-----
	78.182	78.173	+.009		74.145	74.122	+.023
	78.734	78.741	-.007		------	74.214	-----
7.147	77.640	77.628	+.012	5.208	------	74.061	-----
	78.187	78.186	+.001		74.140	74.172	-.032
	78.736	78.754	-.018		------	74.246	-----

TABLE 5.13 ENDOR Frequencies of $^{53}Cr^{3+}$ in GGaSeH(2)

$\vec{H} \parallel \vec{Hz}$				$\vec{H} \perp \vec{Hz}$			
MAGNETIC FIELD kG (±1G)	MEASURED MHz (±5kHz)	CALCULATED MHz	DIFFERENCE	MAGNETIC FIELD kG (± 1G)	MEASURED MHz (±5kHz)	CALCULATED MHz	DIFFERENCE
0.728	75.251	75.265	+.006	2.160	74.180	74.163	+.017
	76.888	76.889	-.001		75.223	75.157	+.066
	78.526	78.524	+.002		------	76.156	-----
0.761	75.252	75.262	-.010	2.210	74.242	74.297	-.055
	76.879	76.879	+.000		75.264	75.286	-.022
	78.518	78.511	+.007		76.251	76.285	-.035
0.775	75.255	75.257	-.002	2.240	74.260	74.376	-.116
	76.879	76.876	+.003		75.279	75.368	-.089
	78.515	78.505	+.010		76.308	76.359	-.051
5.972	77.348	77.335	+.013	4.628	------	75.550	-----
	78.079	78.068	+.011		75.756	75.718	-.038
	78.818	78.819	-.001		------	75.898	-----
5.994	77.345	77.337	+.005	4.666	------	75.573	-----
	78.078	78.078	-.000		75.675	75.745	-.070
	78.821	78.827	-.006		------	75.919	-----
5.015	77.345	77.343	+.002	4.702	75.657	75.579	+.008
	78.081	78.086	-.005		------	75.771	-----
	78.818	78.835	-.017		------	75.953	-----

TABLE 5.14 ENDOR Frequencies of $^{53}Cr^{3+}$ in TlGa Sulfate Alum

$\vec{H} \parallel$

MAGNETIC FIELD kG (±1G)	MEASURED MHz (±5kHz)	CALCULATED MHz	DIFFERENCE
2.374	77.940	77.938	+.002
	78.497	78.498	-.001
	79.052	74.065	-.013
2.420	77.947	77.959	-.012
	78.501	78.508	-.007
	79.057	79.073	-.016
2.436	77.946	77.967	-.021
	78.504	78.513	-.009
	79.058	79.078	-.020
2.484	77.945	77.988	-.043
	78.504	78.529	-.025
	79.067	79.083	-.016
4.264	77.010	77.016	-.006
	77.321	77.331	-.010
	77.625	77.641	-.016
4.326	77.001	77.008	-.007
	77.310	77.310	+.000
	77.623	77.618	+.005
4.461	76.978	76.982	-.004
	77.297	77.268	+.019
	77.616	77.560	+.056

$\vec{H} \perp$

MAGNETIC FIELD kG (± 1G)	MEASURED MHz (±5kHz)	CALCULATED MHz	DIFFERENCE
2.853	76.369	76.376	-.007
	76.840	76.883	-.043
	77.308	76.386	-.078
2.902	76.380	76.384	-.004
	76.886	76.887	-.001
	77.398	77.376	+.022
2.961	76.384	76.390	-.006
	76.909	76.884	+.025
	77.406	77.368	+.038
3.789	77.822	77.786	+.036
	78.197	78.165	+.032
	78.553	78.533	+.020
3.836	77.827	77.817	+.010
	78.187	78.186	+.001
	78.545	78.556	-.011
3.891	77.771	77.854	-.083
	78.145	78.215	-.070
	78.549	78.570	-.021

TABLE 5.15 ENDOR Frequencies of $^{53}Cr^{3+}$ in CsIn Sulfate Alum.

$\vec{H}z$				$\vec{H} \perp$			
MAGNETIC FIELD kG (±1G)	MEASURED MHz (±5kHz)	CALCULATED MHz	DIFFERENCE	MAGNETIC FIELD kG (± 1G)	MEASURED MHz (±5kHz)	CALCULATED MHz	DIFFERENCE
2.196	75.873	75.888	-.013	2.787	77.584	77.552	+.032
	77.256	77.273	-.017		78.475	78.452	+.023
	78.648	78.653	-.005		79.360	79.352	+.008
2.219	75.870	75.880	-.010	2.821	77.600	77.583	+.017
	77.258	77.265	-.007		78.498	78.483	+.015
	78.643	78.645	-.003		79.385	79.370	+.015
2.254	75.855	75.875	-.020	2.844	------	77.607	-----
	77.244	77.255	-.011		78.506	78.494	+.012
	78.632	78.630	+.002		79.394	79.384	+.010
4.482	------	77.933	-----	3.917	------	77.438	-----
	78.444	78.424	+.020		77.485	77.370	+.015
	78.928	78.920	+.008		------	77.501	-----
4.497	77.947	77.936	+.011	3.945	------	77.428	-----
	78.436	78.432	+.004		77.480	77.473	+.007
	78.932	78.923	+.009		------	77.507	-----
4.534	77.953	77.944	+.009	3.988	------	77.425	-----
	78.446	78.442	+.004		77.465	77.465	-.000
	78.931	78.941	-.010		------	77.518	-----
4.550	77.958	77.949	+.000				
	78.444	78.445	-.001				
	------	78.949	-----				

TABLE 5.16 ENDOR Frequencies of $^{53}Cr^{3+}$ in CsAl Selenate Alum

$\vec{H}z$				$\vec{H} \perp$			
MAGNETIC FIELD kG (±1G)	MEASURED MHz (±5KHz)	CALCULATED MHz	DIFFERENCE	MAGNETIC FIELD kG (± 1G)	MEASURED MHz (±5kHz)	CALCULATED MHz	DIFFERENCE
2.113	78.011	78.049	-.038	2.740	76.061	76.164	-.103
	------	78.566	-----		------	76.644	-----
	------	79.098	-----		------	77.129	-----
2.143	77.999	78.062	-.063	2.760	76.011	76.170	-.159
	78.659	78.579	+.080		76.651	76.647	-.004
	------	79.098	-----		------	77.132	-----
2.160	------	78.070	-----	2.776	------	76.180	-----
	78.549	78.576	-.027		76.661	76.652	+.011
	79.106	79.106	+.000		77.162	77.124	+.038
2.178	------	78.081	-----	2.800	------	76.183	-----
	------	78.584	-----		------	76.652	-----
	79.107	79.106	+.001		77.121	77.121	-.000
4.543	77.006	77.063	-.057	3.947	77.759	77.670	+.089
	------	77.419	-----		------	78.047	-----
	------	77.767	-----		------	78.450	-----
4.562	77.052	77.063	-.011	3.964	77.796	77.683	+.113
	77.469	77.409	+.060		------	78.057	-----
	------	77.759	-----		------	78.450	-----
4.579	------	77.061	-----	3.983	77.788	77.693	+.095
	77.341	77.403	-.062		------	78.076	-----
	77.755	77.754	+.001		------	78.455	-----
4.597	------	77.058	-----				
	------	77.398	-----				
	77.760	77.743	+.017				

TABLE 5.17 ENDOR Frequencies of $^{53}Cr^{3+}$ in CsGa Selenate Alum

$\vec{H}$ z				$\vec{H} \perp$			
MAGNETIC FIELD kG (± 1G)	MEASURED MHz (±5kHz)	CALCULATED MHz	DIFFERENCE	MAGNETIC FIELD kG (±1G)	MEASURED MHz (±5kHz)	CALCULATED MHz	DIFFERENCE
1.770	77.966	77.974	-.008	2.584	75.576	75.606	-.030
	------	78.491	-----		------	76.075	-----
	------	79.013	-----		------	76.542	-----
1.787	77.974	77.979	-.005	2.604	75.594	75.614	-.020
	78.502	78.499	+.003		76.087	76.085	+.002
	------	79.018	-----		------	76.552	-----
1.807	78.003	77.987	+.016	2.624	------	75.632	-----
	78.511	78.501	+.010		76.107	76.099	+.008
	79.010	79.023	-.013		76.583	76.563	+.020
1.832	------	78.003	-----	2.641	------	75.643	-----
	------	78.507	-----		------	76.112	-----
	79.027	79.026	+.001		76.598	76.563	+.035
4.895	76.971	76.972	-.001	4.112	77.309	77.332	-.023
	------	77.334	-----		------	77.714	-----
	------	77.684	-----		------	78.102	-----
4.914	76.961	76.970	-.009	4.136	77.388	77.353	+.035
	77.323	77.323	+.000		77.742	77.736	+.006
	------	77.679	-----		------	78.118	------
4.927	------	76.970	-----	4.152	------	77.369	------
	77.325	77.318	+.007		77.749	77.746	+.003
	77.673	77.671	+.002		78.134	78.131	+.003
4.952	------	76.967	-----	4.168	------	77.382	-----
	------	77.310	-----		------	77.757	-----
	77.631	77.660	-.029		78.133	78.141	-.008

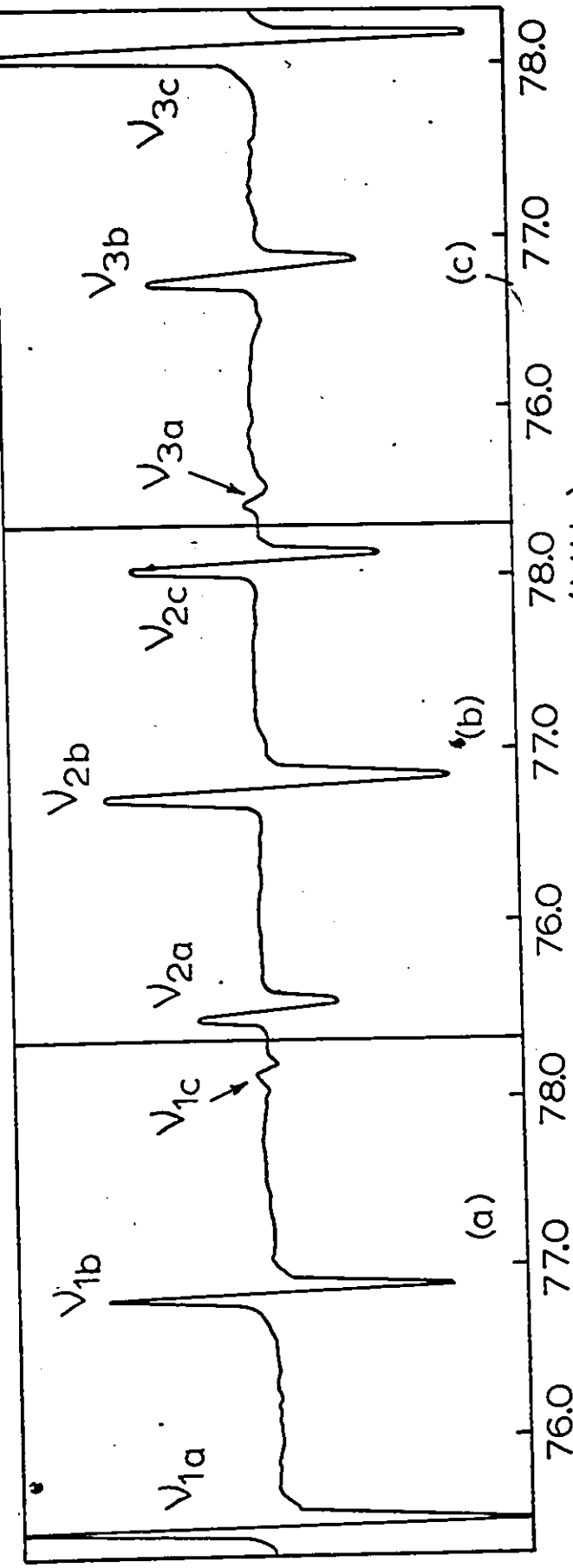

Fig. 5.9 ENDOR Spectra Obtained in GaISH(1) along the z Axis for the Low Field Group of Hyperfine Lines.

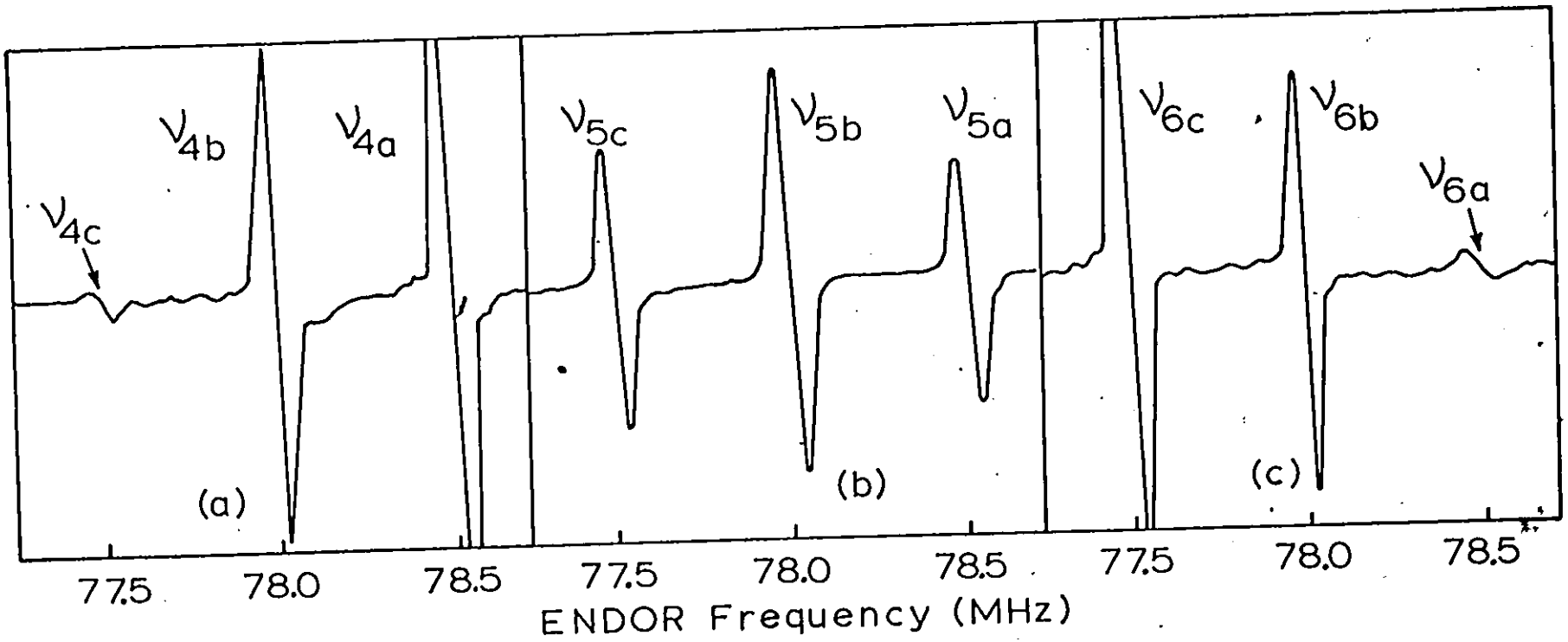

Fig. 5.10 ENDOR Spectra Obtained in GAlSH(1) along the Z Axis for the High Field Group of Hyperfine Lines.

The classification of the key z axis ENDOR lines of Figs. 5.9 and 5.10 is given in Fig. 5.11. Part (a) of Fig. 5.11 represents the $M_S = -3/2 \rightarrow -1/2$ hyperfine lines, (b) gives the relative positions and intensities of the ENDOR lines when the magnetic field was set at the H_1 and H_3 positions, (c) represents the $M_S = 3/2 \rightarrow 1/2$ hyperfine lines, and (d) gives the relative positions and intensities of the ENDOR lines obtained when the magnetic field was set on the H_4 and H_6 positions. For a given magnetic field position H_1, H_2, H_3, etc. the ENDOR line with the greatest intensity, within a triplet ENDOR line spectrum, will originate from the hyperfine spacing connected closest to the ESR transition. For example, for a magnetic field setting H_1 in Fig. 5.11 (a) the ENDOR spectral pattern shown at the left hand side of part (b) is obtained. Since the low frequency line in the spectral pattern has the largest intensity, this means that it must have originated from the hyperfine spacing marked ν_{1a} in part (a) since it connects closest to the ESR transition at H_1. Once the z axis ENDOR lines are assigned in this way then it is relatively simple to fit them to the theoretical hyperfine spacings obtained by diagonalizing the matrix of Fig. 3.3 with a computer.

The actual fitting procedure is done as follows: The matrix of Fig. 3.3 was first diagonalized using second order perturbation theory to give expressions which can be solved to obtain approximate values of the A, B, Q' and g_N' hyperfine parameters. These quantities are then used as starting values in the exact diagonalization of the matrix. Using the $g_{||}$ and D values obtained from the ESR measurements, the hyperfine parameters

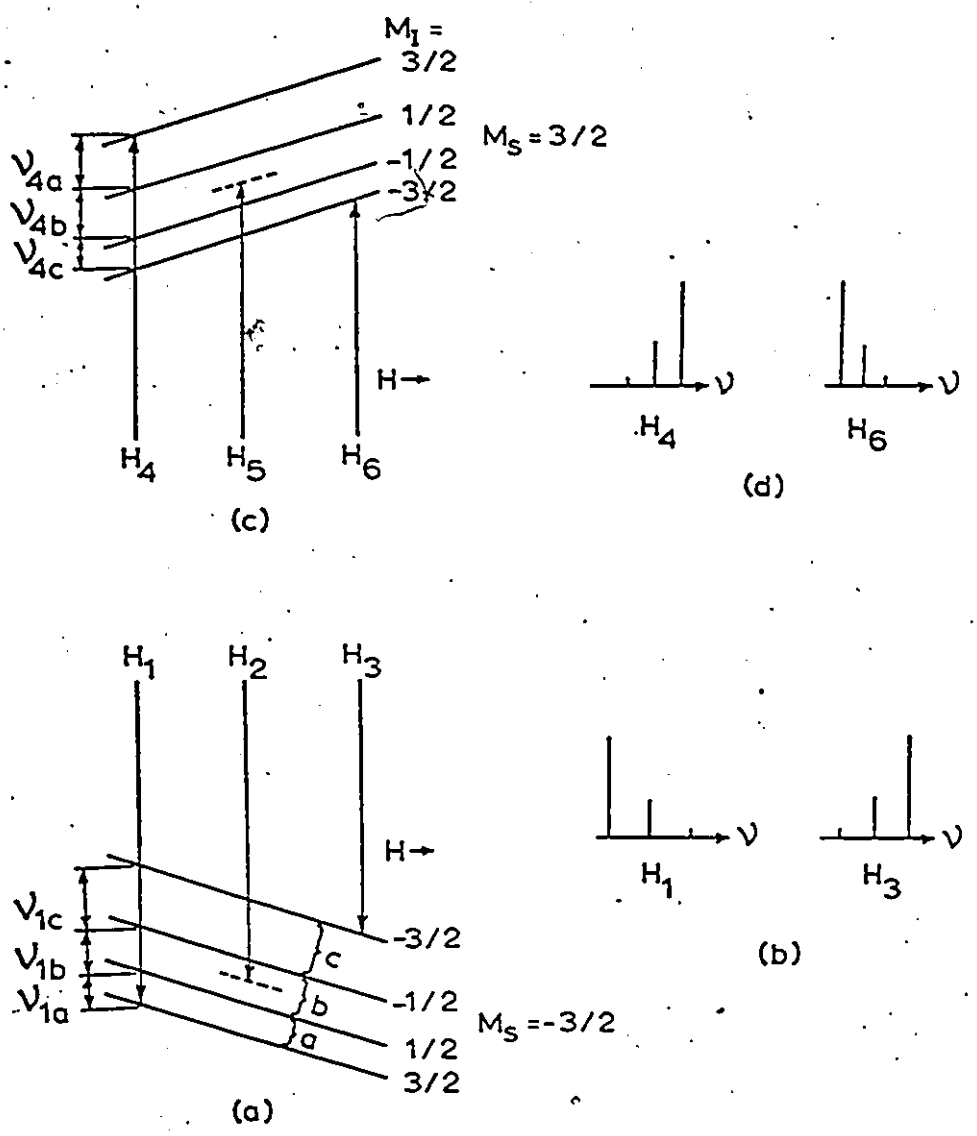

Fig. 5.11 Classification of the ENDOR Lines along the Z Direction.

are then varied in successive steps of computer diagonalization, for measurements along the z axis, until a good fit is obtained between the experimental and theoretical ENDOR frequencies. The diagonalization was accomplished using an I.B.M. diagonalization subroutine called EIGEN. The values of the hyperfine parameters so obtained are then applied, along with the $g_\perp$ and D values, to the perpendicular direction matrix of Fig. 3.4. The hyperfine parameters are again varied slightly until a good fit is obtained along the perpendicular direction. The process is repeated between the two directions until the best fit is obtained. The average error of the fit was 7 kHz along the z axis and 14 kHz along the perpendicular direction. The calculated ENDOR frequencies are listed in Tables 5.6 to 5.17, along with the measured ones. The calculated values of the hyperfine parameters are listed in Table 5.18.

5.5 Measurements of the A and B Hyperfine Parameters at Room Temperature

The $^{53}Cr^{3+}$ hyperfine line spacings were measured at 297 K using common ESR on those crystals which showed good line resolution at this temperature. The A and B values calculated from such measurements have much less accuracy than those obtained from ENDOR measurements. ENDOR measurements cannot be done much above 4.2 K on the dilutely doped crystals because the sensitivity of the effect is low at higher temperatures. Nevertheless it was desirable to obtain the room temperature values of A

TABLE 5.18 Spin-Hamiltonian Hyperfine Parameters $^{53}Cr^{3+}$ in Trigonally Distorted $Cr^{3+}.6H_2O$ Magnetic Complexes at 4.2 K (in Units of $10^{-4}cm^{-1}$).

CRYSTAL	Q'	A	B	A-B	g'_n	Ref.
RbAl Sulfate Alum	-.0215	17.3573	17.2738	.0835	-.3170	a
RbGa " "	-.0164	17.3722	17.2914	.0808	-.3111	b
TlGa " "	-.0217	17.4335	17.3434	.0901	-.3180	
CsAl " "	.1545	17.2038	17.4587	-.2549	-.3140	a
CsGa " "	.1546	17.2119	17.4754	-.2635	-.3110	b
CsIn " "	.1559	17.2283	17.5166	-.2883	-.3146	
CsAl Selenate Alum	-.0144	17.4033	17.3060	.0973	-.3135	
CsGa " "	-.0137	17.4051	17.2921	.1130	-.3150	
$AlCl_3.6H_2O$	.1591	17.2960	17.5192	-.2232	-.3261	c
GAlSH(2)	.1866	17.0982	17.4236	-.3254	-.3165	
GAlSH(1)	.1682	17.0774	17.4273	-.3499	-.3165	
GGaSH(2)	.1868	17.1402	17.4765	-.3363	-.3162	
GGaSH(1)	.1740	17.1102	17.4594	-.3492	-.3175	
GAlSeH(2)	.2045	17.0884	17.4998	-.4114	-.3179	
GAlSeH(1)	.1674	17.0260	17.4721	-.4461	-.3215	
GGaSeH(2)	.1974	17.0997	17.5007	-.4010	-.3176	
GGaSeH(1)	.1670	17.0140	17.4540	-.4400	-.3176	

a Manoogian and Auger, Ref. 2.

b Danilov and Manoogian, Ref. 1.

c Pack and Manoogian, Ref. 3.

and B for a number of complexes because they afford a check to the values predicted in the subsequent analysis. Measurements were made on the complexes listed in Table 5.19. The resolution of typical groups of hyperfine lines in GAlSeH and $AlCl_3.6H_2O$ is shown in Fig. 5.4. The resolution of the lines obtained in CsAl, CsGa sulfate and selenate alums was intermediate between the examples shown in Fig. 5.4.

Measurements of A and B can be made along the magnetic z and perpendicular directions, respectively, by measuring the spacings H' (in Fig. 5.4) for the $M_S = 1/2 \rightarrow -1/2$, $3/2 \rightarrow 1/2$ and $-3/2 \rightarrow -1/2$ groups of hyperfine lines. The values of A or B, correct to second order in perturbation theory, are given by $(H'_{1/2\rightarrow -1/2} + H'_{3/2\rightarrow 1/2} + H'_{-3/2\rightarrow -1/2})/9$. Except for the case of $AlCl_3.6H_2O$, the central $M_S = 1/2 \rightarrow -1/2$ group of hyperfine lines is obstructed by other chromium magnetic complexes in the crystals. In these cases H' was measured for only the $M_S = 3/2 \rightarrow 1/2$ and $-3/2 \rightarrow -1/2$ groups, and the value of A or B was taken as $(H'_{3/2\rightarrow 1/2} + H'_{-3/2\rightarrow -1/2})/6$.

TABLE 5.19. $^{53}Cr^{3+}$ A and B Hyperfine Parameters Measured at Room Temperature (297 K) in Units of $10^{-4}cm^{-1}$. Error is ± 0.20 ($10^{-4}cm^{-1}$).

COMPLEX	A	B
GAlSeH(1)	17.15	17.60
GAlSeH(2)	17.24	17.49
CsAl Sulfate Alum	17.58	17.44
CsAl Selenate Alum	17.60	17.45
CsGa Selenate Alum	17.15	17.50
$AlCl_3.6H_2O$	17.32	17.52

CHAPTER 6

ANALYSIS OF THE EXPRIMENTAL RESULTS

6.1 ESR Results: Classification of the Salts According to Their Magnetic Behavior

The D values listed in Table 5.4 are plotted as a function of temperature in Figs. 6.1 to 6.3. The general form of the curves is a straight-line part between 195 and 297 K, and a bending part below 195 K. The straight line parts of the curves have been extended linearly to high temperatures in order to show more clearly how the various curves are grouped into families. The extended curves aren't meant to describe the high temperature values of D. Indeed it is difficult to measure D values in the hydrated crystals much above room temperature because the crystals lose waters of hydration and their structures become altered. The nature of the grouping of the D vs T curves can form a basis for the classification of the salts according to their magnetic behavior. The two families of the guanidinium salts are dependent on whether the sulphur or selenium atom forms the structure. The sulfate alums are grouped as to the type of monovalent ion, Cs, Rb or Tl. Moreover if the S atom is replaced by Se then these atoms will also determine the grouping.

Generally speaking, two types of behaviors are observed when the high temperature extensions of the D vs T curves are considered. These are the near parallelism of the lines or the existence of common crossing points at high temperatures. As shown in Fig. 6.1, the two groups of

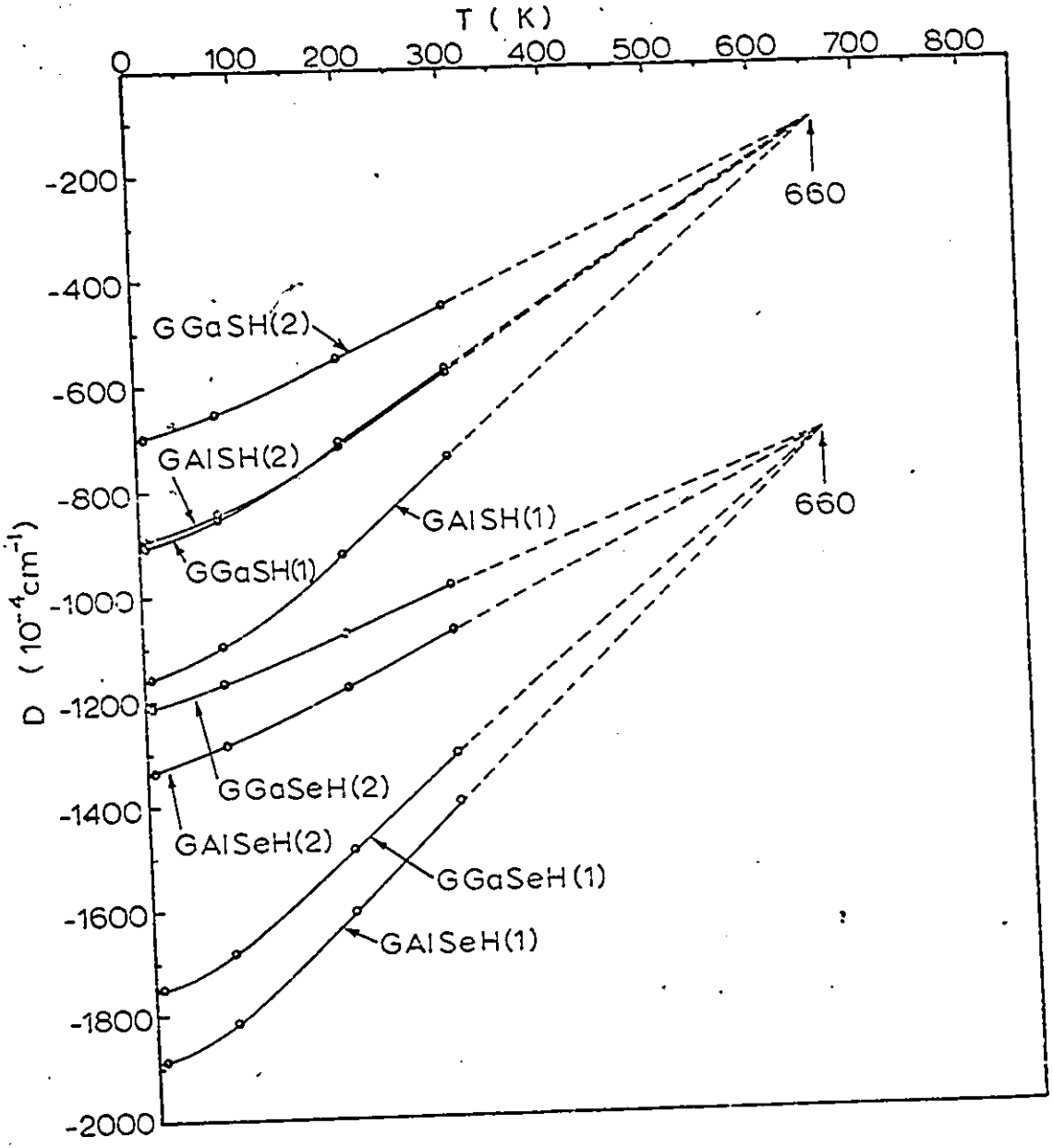

Fig. 6.1 D vs T curves for Cr^{3+} in the Isomorphs of GAlSH.

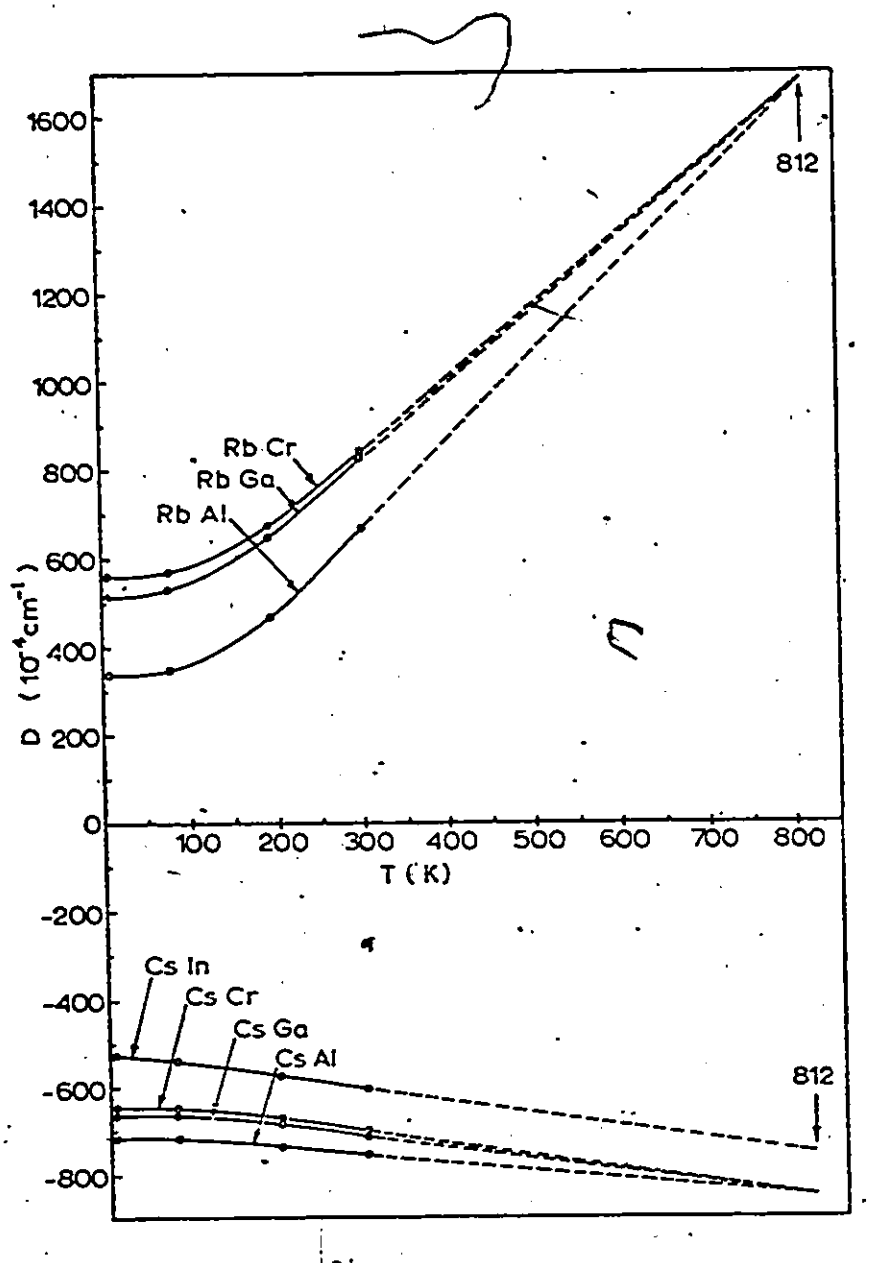

Fig. 6.2 D vs T Curves for Cr^{3+} in the Rb and Cs Sulfate Alums.

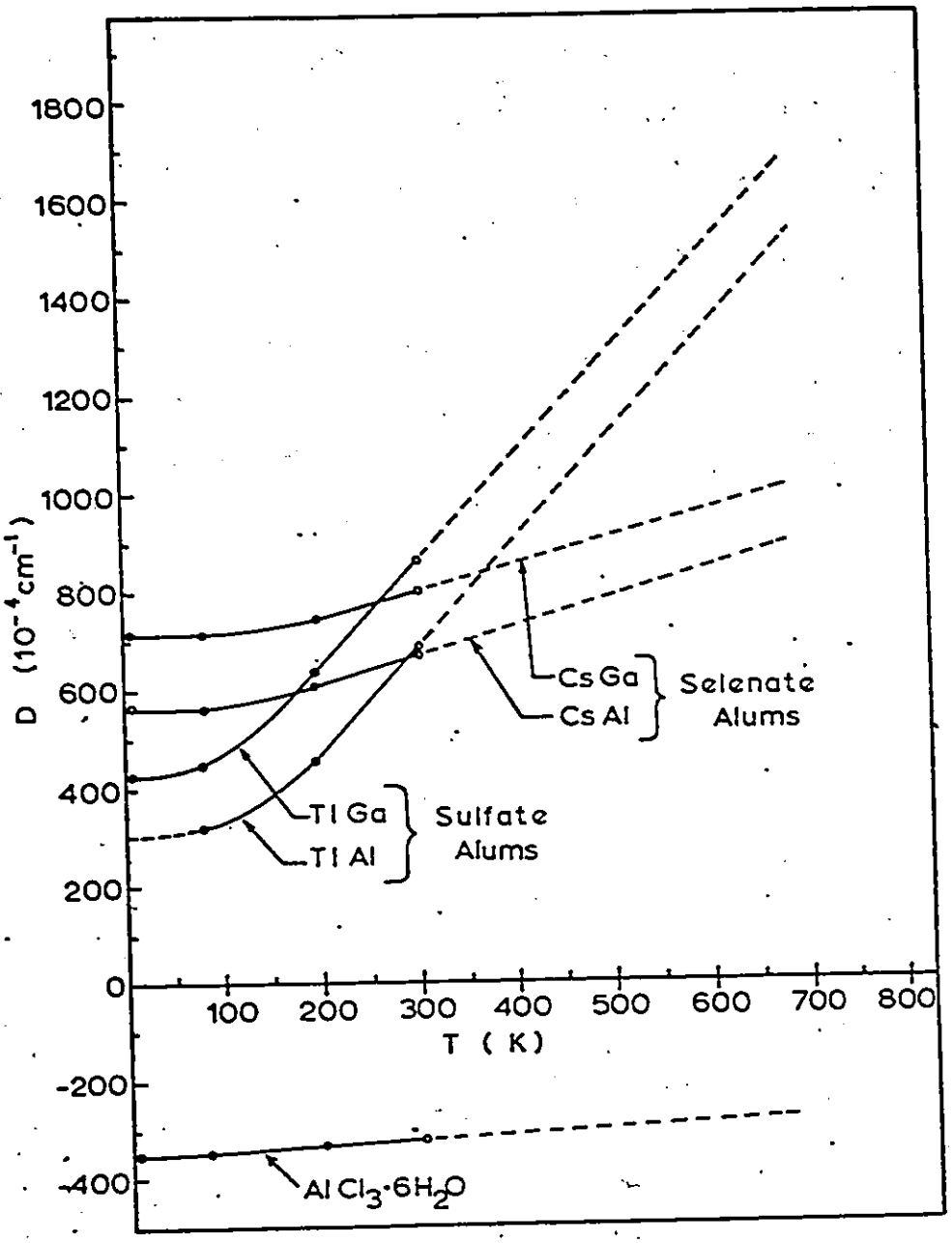

Fig. 6.3 D vs T Curves for Cr^{3+} in the Tl Sulfate and Cs Selenate Alums and in the Crystal of $AlCl_3 \cdot 6H_2O$.

guanidinium salts have common crossing points at 660±10 K, while in Fig. 6.2 it is observed that the Rb and Cs sulfate alums have crossing points at 812±10 K. CsIn sulfate alum is an exception in that its line runs nearly parallel to that of CsCr alum. In the cases of the Cs selenate and Tl sulfate alums of Fig. 6.3, the line groups show near parallelism Another interesting property of the extended lines in the guanidinium salts is that at high enough temperatures they will eventually cross the D axis and change sign. This effect does not occur in the alums shown in Figs. 6.2 to 6.3, even if the straight line parts between 195 and 297 K are extended back towards the D axis. The reason for these varied behaviors are accounted for, in the sections given below, in terms of the crystal vibrational and static distortion effects, which constitute the D vs T curves.

The effect of ionic radii is also evident in the resonance data. The D value is larger at all temperatures for the guanidinium selenates than for the sulfates, and this is likely related to the larger size of selenium. The ionic radii of these atoms are Se^{6+} = 0.42 and S^{6+} = 0.30Å. When considering the following ionic radii of Al^{3+} = 0.51, Ga^{3+} = 0.62, Cr^{3+} = 0.63 and In^{3+} = 0.81Å, it is observed in Fig. 6.2 for the alums that the spacings in D between the curves at 297 K are approximately in proportion to the differences in ionic radii. The D vs T curves serve to classify the alums in a consistent manner, in contrast to X-ray structure measurements which contain some ambiguities in this respect. In the X-ray work both the RbCr and TlGa alums are described as being of β type, similar to the

Cs sulfate alums. However, the magnetic behavior of RbCr alum, as determined by its D vs T curve, is the same as that of the RbAl and RbGa α alums, and a similar situation holds for TlGa alum. The X-ray structure studies of the guanidinium salts did not establish a method of classifying these crystals, whereas the resonance work shows that the isomorphs belong in two groups depending on the S or Se atom.

6.2 ENDOR Results

The values of Q' and A-B obtained from the ENDOR measurements at 4.2 K are plotted in Fig. 6.4 against the corresponding values of D which were found at 4.2 K from the ESR measurements. The Q' values in the figure fall on a number of horizontal lines, there being several close spaced lines for negative D and only one for positive D. The Q' values for negative D are nearly an order of magnitude greater than for positive D. The A-B points follow a straight-line trend and so a best straight line is drawn through them. The A-B line for positive D is drawn to be parallel to that of negative D. Actually, the A-B lines are not used in the analysis, but are presented because they give an indication of the asymmetric behavior of the crystal field as seen by the chromium nucleus. The individual A and B values, however, are analyzed below. The diagonal lines termed k_S in Fig. 6.4 are a consequence of the analysis of the Q' and D parameters into their static and vibration constituents. The Q' vs D plot is the key to such an analysis because of the nature of the plot, and also because of the theoretical relationship linking Q' with D for

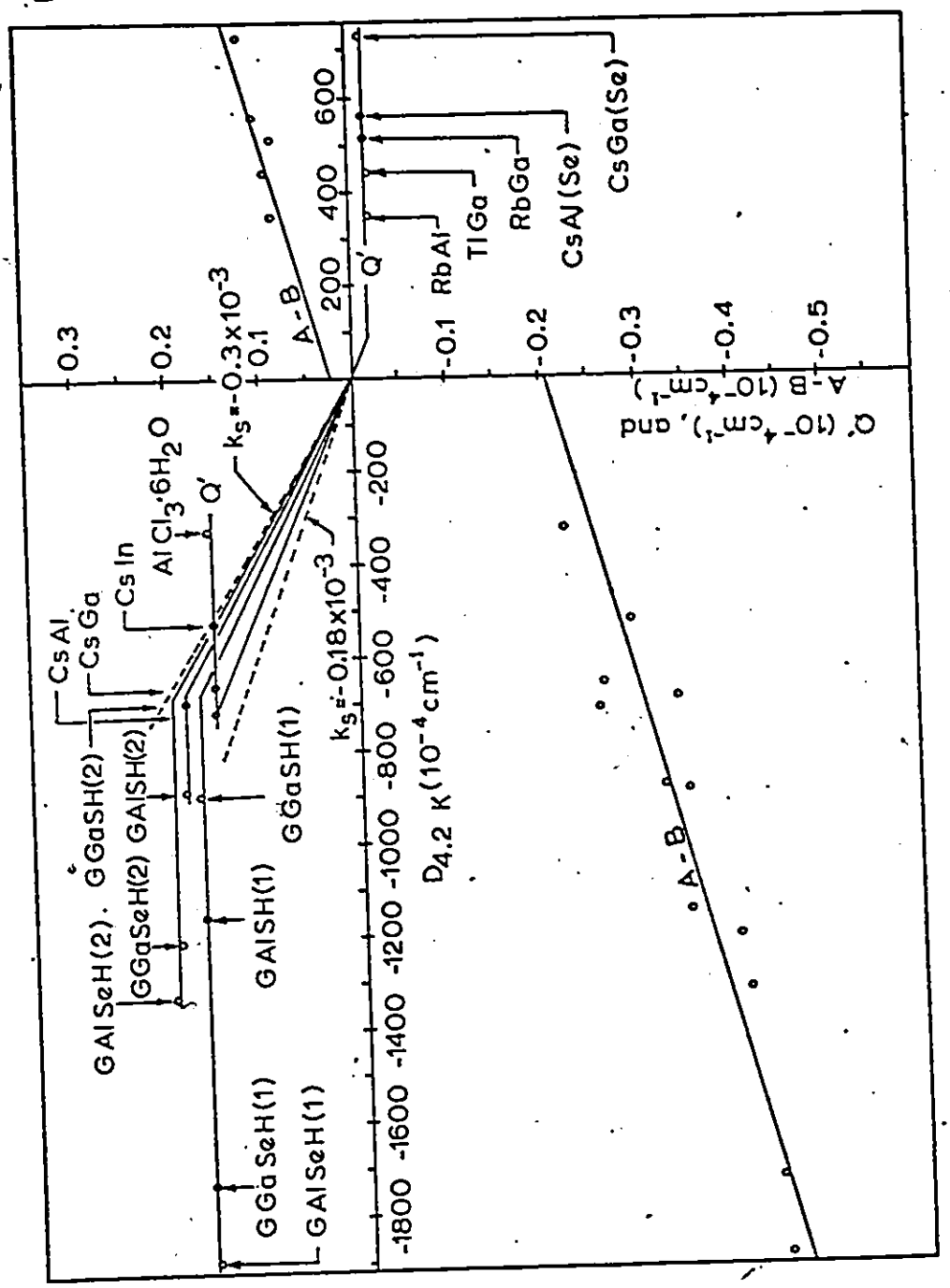

Fig. 6.4 Plot of Q' and A-B vs $D_{4.2\ K}$ for Trigonally Distorted $^{53}Cr^{3+}.6H_2O$ Magnetic Complexes in Hydrated Crystals.

the static effect.

6.3 Procedure for Splitting the Spin Hamiltonian Parameters due to the Contributions of Crystal Vibrational and Static Distortion Effects.

The splitting procedure used to obtain the contributions of the crystal vibrational and static distortion effects to the spin Hamiltonian parameters is empirical. It is based on the experimental results displayed by the D vs T curves of Figs. 6.1, 6.2 and 6.3, and by the Q' vs D plot of Fig. 6.4. It is assumed in the analysis that the temperature dependence of each D vs T curve is due to contributions from the trigonal static distortion at the Cr^{3+} site (D_S) and the vibrational effects of the crystal lattice (D_V). The total D is written as $D = D_S + D_V$, which in functional form is given by Eq. 3.8 as

$$D = D_S^o (1 + \alpha T + \beta T^2) + D_V^o \coth(\theta/2T). \qquad (6.1)$$

This equation must be fitted to each of the D vs T curves. However, each of those curves consist of at most four experimental points with an accuracy of ± 5 ($10^{-4} cm^{-1}$) and there are five parameters to be fitted, namely D_S^o, D_V^o, α, β and θ. When a least square fit of Eq. 6.1 is applied to the curves it is found that all the curves can be fitted within the experimental accuracy for a whole range of θ's from 100 to 1000 K. This method produces a wide range of values for the set of parameters D_S^o, D_V^o, α and β. In order to investigate the nature of the fit for each curve at a given θ, the sensitivity of the parameters for incremental changes in θ

is considered. For example, the sensitivity of the parameter D_S^o is $dD_S^o/d\theta$, and when this is plotted as a function of θ the curve shown in Fig. 6.5 is obtained. It is noted in this figure that the sensitivity of D_S^o is low for small or large values of θ, but that it is high in the range $\theta = 510 \pm 10$ K. D_S^o changes rapidly in this sensitive region, even for increments of θ as small as 0.1 K, and it goes from a large positive to a large negative value. The value of D_S^o is always large outside the sensitive region. Fig. 6.5 is drawn for complex GAlSH(1). When similar plots are made for the other parameters D_V^o, α and β it is found that they also have a maximum sensitivity near 510 K. Moreover, it is found that the four parameters belonging to each of the D vs T curves all have maximum sensitivities near 510 K.

The value of $\theta = 510 \pm 10$ K appears to have a special significance in these crystals. In this respect it is noted that Carlin and Walker[5] found a value of $\theta = 500$ K for the effect of vibrations on the $^4T_2$ band of chromium in the guanidinium salts and in ammonium alum. At this stage of the analysis it is not yet possible to determine unique values of D_S^o, D_V^o, α and β for the individual complexes because their values change rapidly in the sensitive region. The Q' vs D plot of Fig. 6.4 must be used to continue the analysis. In Chapter 3 it was shown that the static theory predicted both Q_S' and D_S to be proportional to the electric field gradiant $V_{zz}^{(S)}$ at the chromium site, and so it was possible to write $Q_S' = k_S D_S$ with k_S given by Eq. 3.14. The relation $Q_S' = k_S D_S$ implies that the static part of Q' is directly proportional to the static part of D.

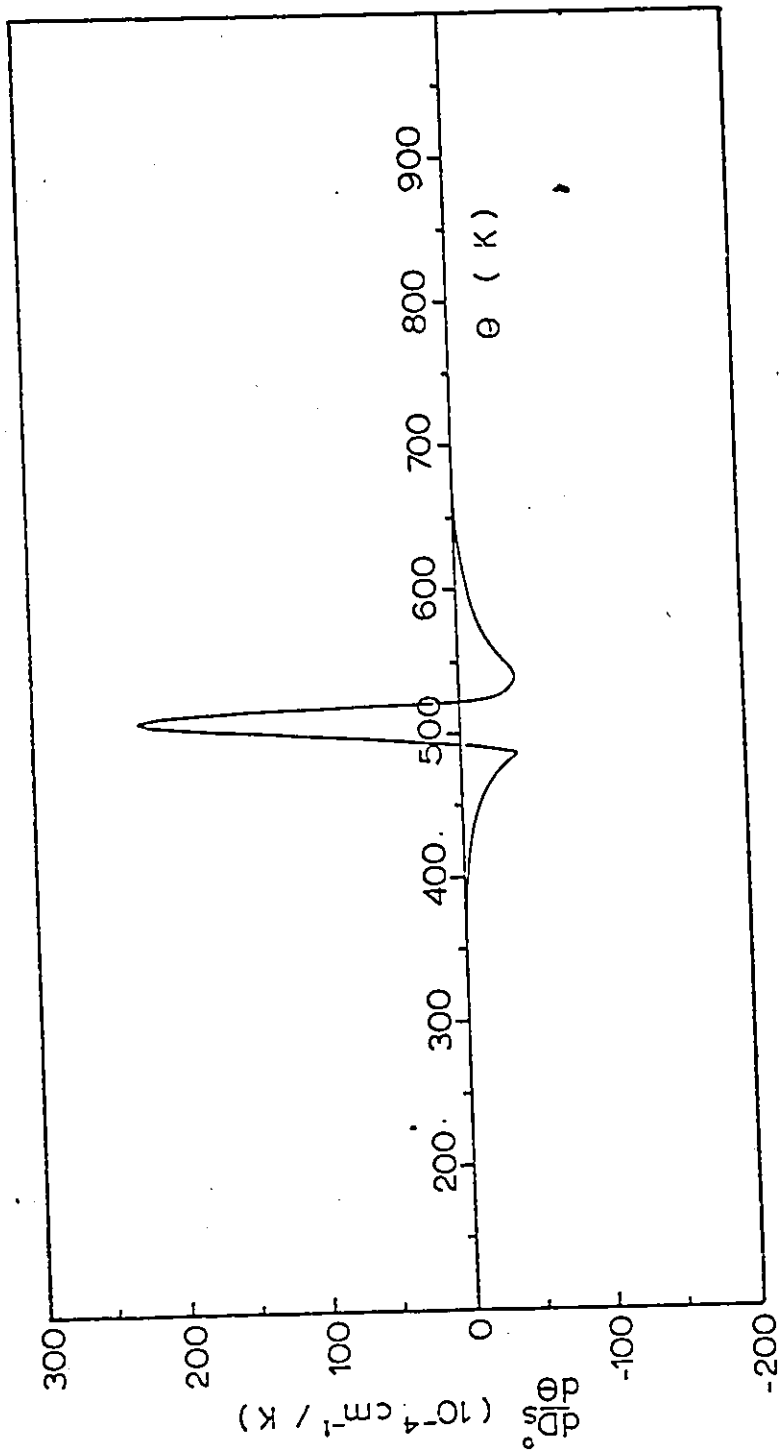

Fig. 6.5 Sensitivity Plot of the D_S^o Parameter as a Function of θ for the Magnetic Complex GA1SH(1)

But in Fig. 6.4 it is observed that the measured Q' values fall on a set of horizontal lines which are independent of D. Hence, since $D = D_S + D_V$, this means that the vibrational part of D must be accounted for by a relation of the form $Q'_V = k_V D_V$. The two contributions together give $Q' = Q'_S + Q'_V$, or more specifically

$$Q' = k_S D_S + k_V D_V, \tag{6.2}$$

where k_S and k_V are constants for any set of Q' points that fall on a given horizontal line of Fig. 6.4.

An initial approximate value of k_S in Eq. 6.2 can be found from the data as follows. Equation 6.2 is first divided by D_V to give the relation

$$Q'/D_V = k_S(D_S/D_V) + k_V. \tag{6.3}$$

This is of the form $y = mx+b$, and so Eq. 6.3 represents a straight line with slope k_S and intercept k_V. Values of D_S and D_V at 4.2 K are obtained for a given θ from the computer readout of the fit of Eq. 6.1 to the experimental D vs T curves. The values obtained at 4.2 K are used because measurements of Q' were made at this temperature in the ENDOR studies. For a given θ, the points of the form $(D_S/D_V, Q'/D_V)$ are plotted with Q'/D_V along the y axis and D_S/D_V along the x axis. Each plot consists of seventeen points, which is the number of available Q' values. A best straight line is then drawn through the points. Since the line represents

Eq. 6.3 then its slope must be k_S and its intercept k_V. This procedure is repeated for many values of θ in the range 100 to 1000 K. It is found that the slope of the line is nearly the same for each chosen value of θ, but that the intercepts vary somewhat. The values of k_S are found to fall in the range of $-0.18(10^{-3})$ to $-0.30(10^{-3})$. The sign of k_V is found to be negative over nearly the whole range of θ, with the exception of about 1 near 510 K where it is positive. Moreover, the relation $k_V = -k_S$ is found to hold in this 1 K range.

Up to this point we have been able to determine the range of validity for k_S and an approximate value of $\theta = 510 \pm 10$ K for all the chromium magnetic complexes. To continue the analysis, the lines described by $Q'_S = k_S D_S$ defining the critical region of k_S are drawn dotted in Fig. 6.4. If D_V is equal to zero for a given Q' point, then Eq. 6.2 requires the point to fall on a line described by $Q'_S = k_S D_S$ with k_S lying within the critical region, since such a line represents pure static distortion and zero vibration. However, most of the Q' points not only do not fall on such lines but they form a system of horizontal lines which are independent of D. This effect is attributed to a combination of static and vibrational contribution to Q' and it can be accounted for in a straightforward manner in this analysis with the aid of Eq. 6.2. As an example of this treatment we consider the straight horizontal line drawn through the Q' points of GAlSeH(1), GGaSeH(1), GAlSH(1) and GGaSH(1). If the purely static contribution of all the points on the horizontal line is described by $Q'_S = k_S D_S$ with a given value of k_S in the allowed range,

then the vibrational contribution must be given by another straight line of the form $Q'_V = k_V D_V$ with the condition that $k_V = - k_S$. In this way the sum of the two contributions can add up to give the straight horizontal line found experimentally. For Q' points lying on a horizontal line different from the above example, then a different k_S is indicated but the relation $k_V = - k_S$ must still be maintained. As stated above, for all the magnetic complexes considered together, the sign of k_S is found to be negative. This means that k_V must be positive for the relation $k_V = - k_S$ to hold. Such a relation was found to hold in the limited range of 1 K near θ=510 K. It should be mentioned that while the θ value of best fit (i.e., positive k_V with $k_V = -k_S$) falls in the range $\theta = 510 \pm 10$ K for all the complexes considered together, it is not necessarily the same for each individual complex.

The actual values of D_S and D_V at T = 4.2 K for each magnetic complex can be determined graphically from Fig. 6.4 with the aid of Eq. 6.2. As shown in Fig. 6.4, straight horizontal lines can be drawn through the Q' points (i) for GAlSeH(1), GGaSeH(1), GAlSH(1), and GGaSH(1), (ii) for GAlSeH(2) and GGaSeH(2), (iii) for GAlSH(2) and GGaSH(2), (iv) for CsAl, CsGa and CsIn sulfate alums and $AlCl_3 \cdot 6H_2O$, and (v) for RbAl, RbGa and TlGa sulfate alums and CsAl and CsGa selenate alums. Cognizance must be made in the following analysis to the fact that, for the seventeen magnetic complexes pertinent to our discussion, the D vs T curves can be classified into three general groups. That is, the members of a group behave in a related manner, and there is a difference of behavior between

the groups. One group consists of the guanidinium complexes, another consists of the Cs sulfate alums plus $AlCl_3.6H_2O$, and the third is made up of the Rb and Tl sulfate alums and the Cs selenate alums. The correct value of k_S in the static lines $Q'_S = k_S D_S$ must be chosen partly on the basis of judgement when considering a particular set of Q' values, but there are some constraints on the choice. The most obvious constraint is the fact that k_S must fall within the allowable range indicated by the dotted lines in Fig. 6.4. Another is that the $Q'_S = k_S D_S$ line cannot pass between two Q' points belonging to a given horizontal line, but must pass on either one side or the other of the whole set. If this is not done then the subsequent decomposition of the related Q' points will give widely unrelated values of D_S and D_V which are incompatible with the orderly nature of the D vs T curves. In this respect, a valid separation of a set of D vs T curves into static and vibrational contributions can only be obtained if the signs of D_S or D_V are the same for all members of the group. The relation between the signs and magnitudes of D_S and D_V as described by Eq. 6.2, for Q' points in the four quadrants of Fig. 6.4, is shown in Fig. 6.6.

The actual static lines used in this analysis are shown in Fig. 6.4. For the Q' points in the upper left hand quadrant of Fig. 6.4 the slopes of the static lines are drawn to be essentially in proportion to the magnitudes of the Q' values. In this way the static line for the Cs sulfate alums plus $AlCl_3.6H_2O$ falls near the left side of the set of Q' points. Its actual position is in fact chosen to pass through the Q'

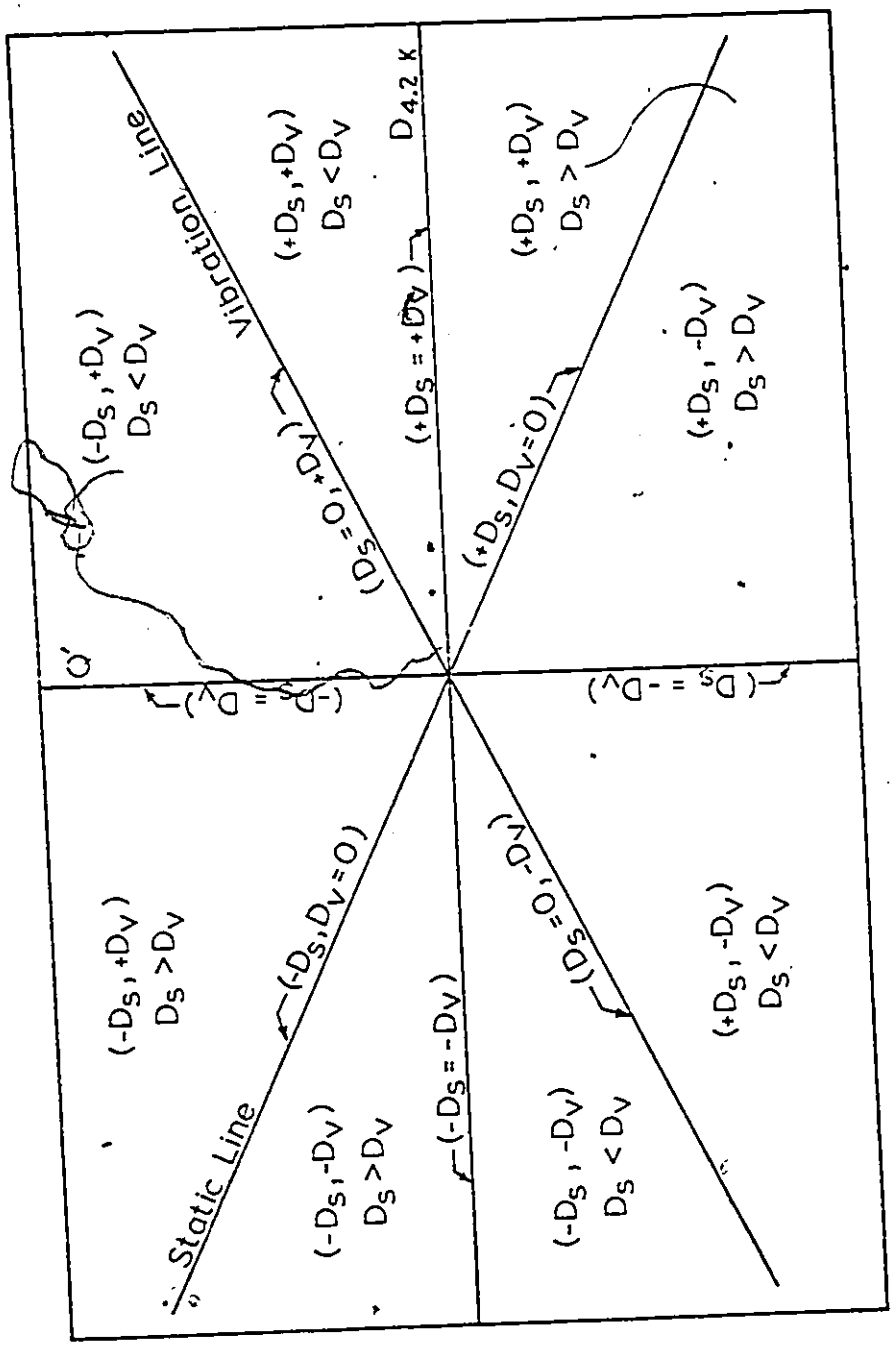

Fig. 6.6 Magnitudes and Signs of D_S and D_V in the Equation $Q' = k_S D_S + k_V D_V$ for Q' Points in the $(D_{4.2\ K}, Q')$ Plane.

point of CsAl sulfate alum. The static lines for the guanidinium complexes all fall to the right hand side of the Q' points. The line for the Rb, Tl sulfate alums and Cs selenate alums is taken to be the same as that for the Cs sulfate alums. The reason for the different values of k_S and the need for several static lines, can be attributed to the fact that the constant in front of Eq. 3.14 is different for the various groups of magnetic complexes. The four values of k_S used in Fig. 6.4 are $-0.300(10^{-3})$, $-0.290(10^{-3})$, $-0.257(10^{-3})$ and $-0.215(10^{-3})$.

The graphical procedure for finding the value of D_S and D_V at 4.2 K for a typical Q' point of the guanidinium salts is illustrated in Fig. 6.7. The first step of the procedure is to draw the static line $Q' = k_S D_S$ with the chosen value of k_S, and then to draw the vibration line $Q'_V = k_V D_V$ with $k_V = -k_S$. With the aid of a pair of dividers, equal values of Q'_V are measured off at the two positions shown marked in the square boxes. The values of D_S and D_V are then read off the x axis as indicated in the figure. The correct value of Q'_V is obtained when the sum of D_S and D_V is equal to the D value of the given Q' point. These values can alternately be found without the use of dividers simply by drawing lines parallel to Q'_S and Q'_V and passing through the considered Q' point. These lines are shown dotted in Fig. 6.7. This procedure is repeated for all the Q' points that fall on the horizontal line under consideration. All such points will have the same static and vibration lines described by Eq. 6.2.

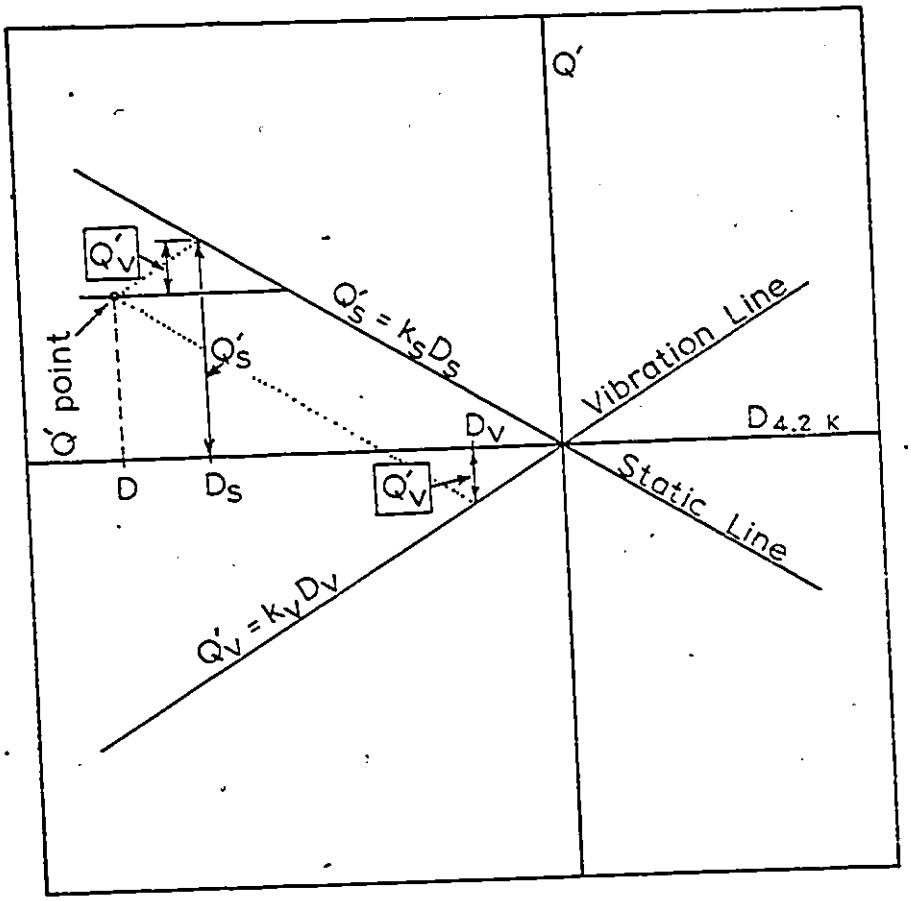

Fig. 6.7 Graphical Procedure for Obtaining the Value of D_S and D_V for a Given Q' Point.

When the values of D_S and D_V at 4.2 K have been found for all seventeen Q' points by the above procedure, it is then possible to pick out the values of D_S^o, D_V^o, α, β and θ for each pair of D_S and D_V from the computer readouts of Eq. 6.1 which are evaluated at 4.2 K. The parameters obtained for all the magnetic complexes are listed in Table 6.1. With the aid of these parameters it is possible to draw graphs of the static and vibrational contributions to the D vs T curves by plotting the separate parts of Eq. 6.1. These plots are shown in Figs. 6.8 to 6.12 for the various magnetic complexes. The portions of the separated curves above 297 K are expected to have less validity at elevated temperatures because they are not derived from fitted points on the original D vs T curves at these temperatures. Their positions are a consequence of the fit below 297 K but they can be expected to give a general description of the high temperature region.

In Fig. 6.13 a graph is made of D_S^o vs D_V^o, and it is seen that all the points fall on essentially two straight lines which have slopes of 45°. The upper line in the figure is due to the magnetic complexes with positive D values, while the lower line is for negative values. It can be shown that the graph reflects the nature of Eq. 6.2 if the close approximation is made that D_S and D_V at 4.2 K are equal to D_S^o and D_V^o, respectively. In this case Eq. 6.2 becomes

$$D_S^o = D_V^o + Q'/k \text{ when } k_V = -k_S,$$

and this equation gives a correct description of Fig. 6.13.

TABLE 6.1 Values of the Parameters D_S°, D_V°, α, β and θ that Occur in the Equation $D = D_S^\circ (1+\alpha T+\beta T^2)+ D_V^\circ \coth (\theta/2T)$

CRYSTAL	D_S° (10^{-4} cm^{-1})	D_V° (10^{-4} cm^{-1})	α (10^{-4} K^{-1})	β (10^{-6} K^{-2})	θ (K)
RbAℓ sulfate alum	225.0	124.0	-12.5100	18.5090	513.5
RbGa " "	299.9	218.1	- 1.5871	8.5822	511.5
TℓGa " "	271.1	170.4	1.2212	14.3730	512.5
CsAℓ " "	-714.5	0.0	1.6003	0.2141	512.5
CsGa " "	-685.4	25.4	1.4877	0.6759	510.5
CsIn " "	-630.1	102.1	2.0701	1.5091	511.0
CsAℓ selenate alum	298.1	260.9	2.1966	-0.6941	511.5
CsGa " "	368.2	351.8	0.4260	-2.0550	513.5
$AlCl_3.6H_2O$	-539.5	192.6	-1.7585	1.9830	514.0
GAℓSH(2)	-764.4	-125.6	-6.9958	-3.1180	509.5
GAℓSH(1)	-914.6	-242.4	-7.5520	-4.0522	509.5
GGaSH(2)	-671.9	- 22.1	-8.0658	-1.5956	506.5
GGaSH(1)	-782.2	-117.8	-7.6896	-2.9719	513.5
GAℓSeH(2)	-966.4	-363.6	-5.1280	-3.1397	515.5
GAℓSeH(1)	-1267.0	-615.0	-5.0813	-5.0567	511.5
GGaSeH(2)	-910.5	-300.5	-4.8424	-2.8433	505.5
GGaSeH(1)	-1202.0	-536.0	-4.6541	-4.9225	512.5

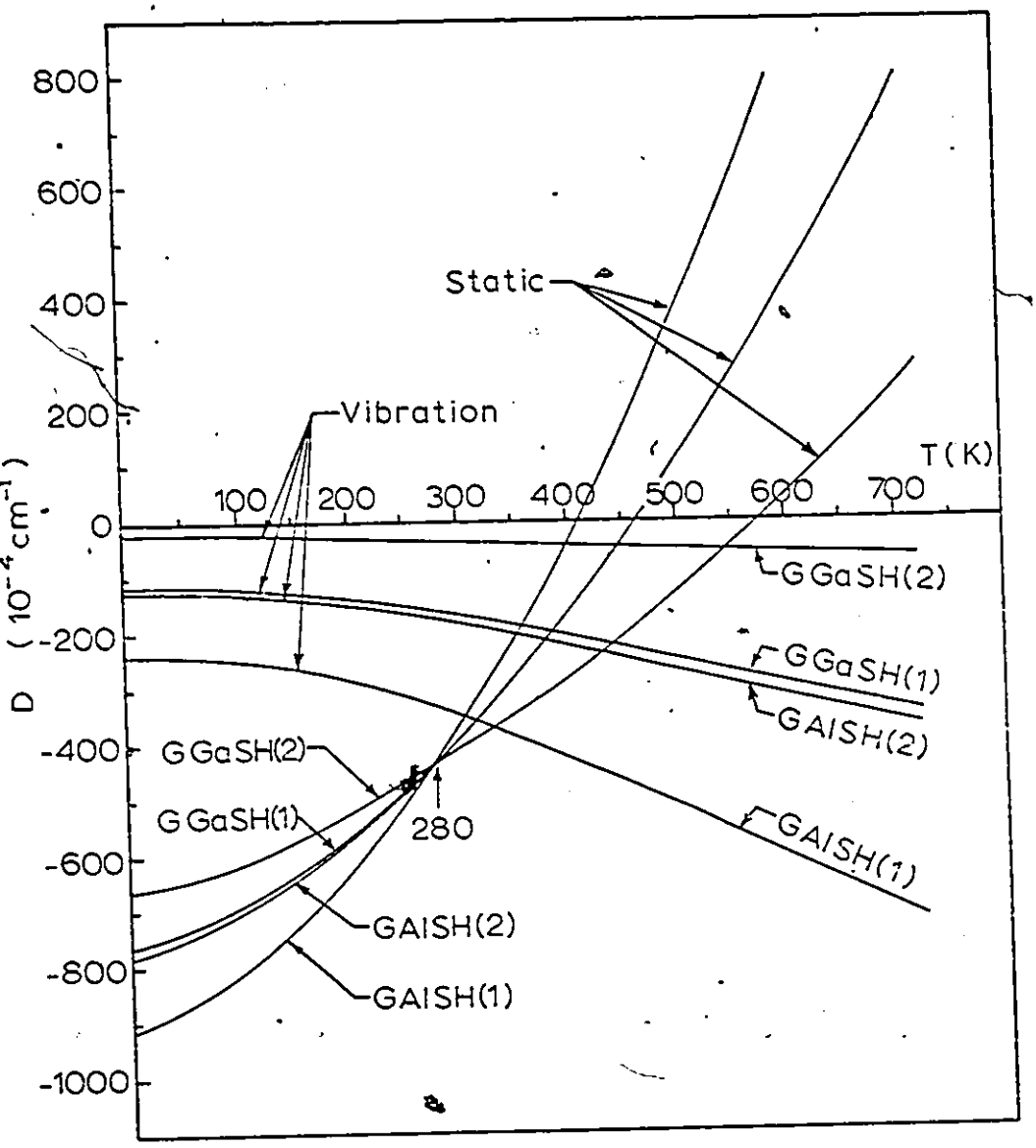

Fig. 6.8 D_S vs T and D_V vs T Curves for the Guanidinium Sulfate Magnetic Complexes.

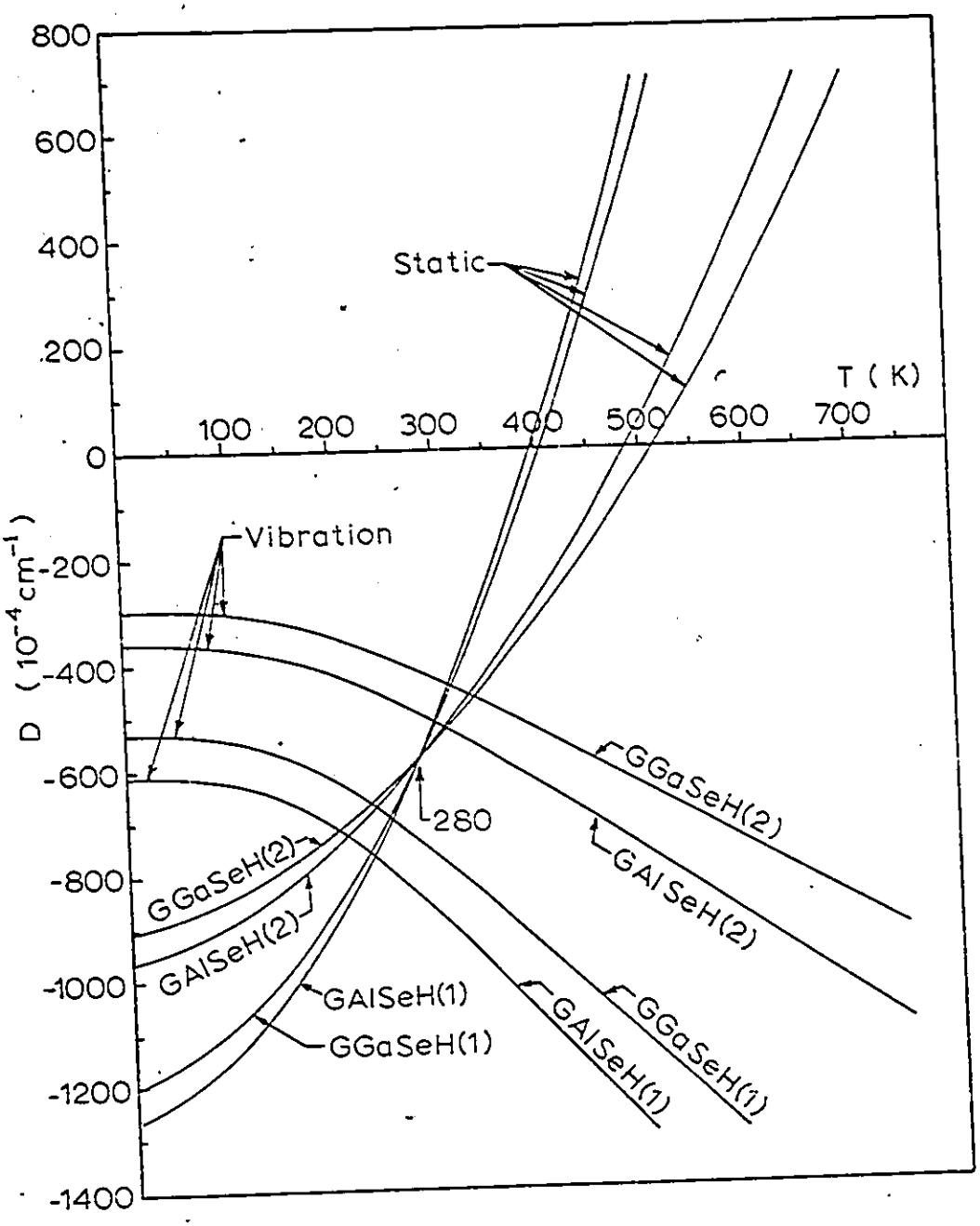

Fig. 6.9 D_S vs T and D_V vs T Curves for the Guanidinium Selenate Magnetic Complexes.

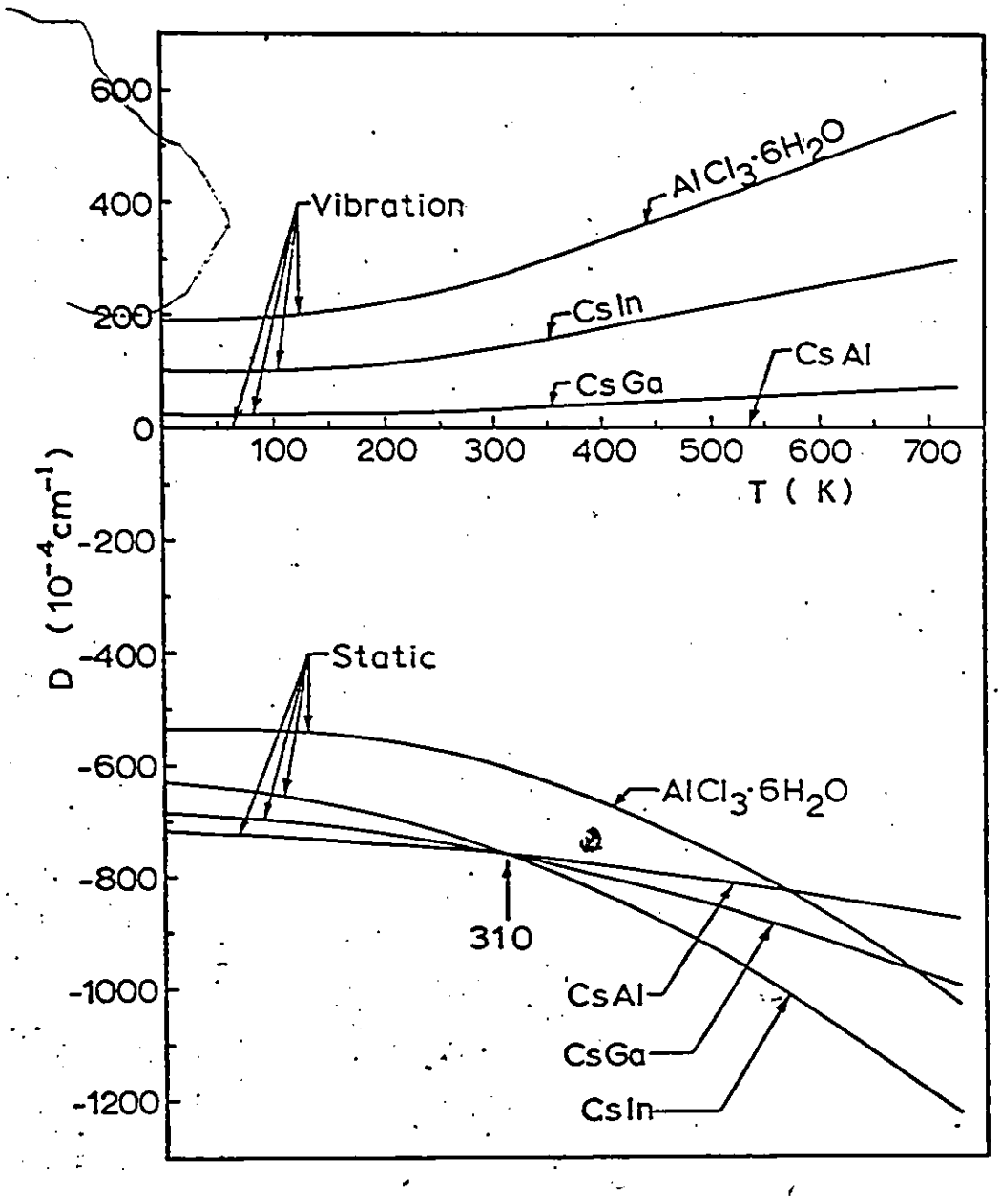

Fig. 6.10 D_S vs T and D_V vs T Curves for the Cs sulfate Alums and $AlCl_3 \cdot 6H_2O$.

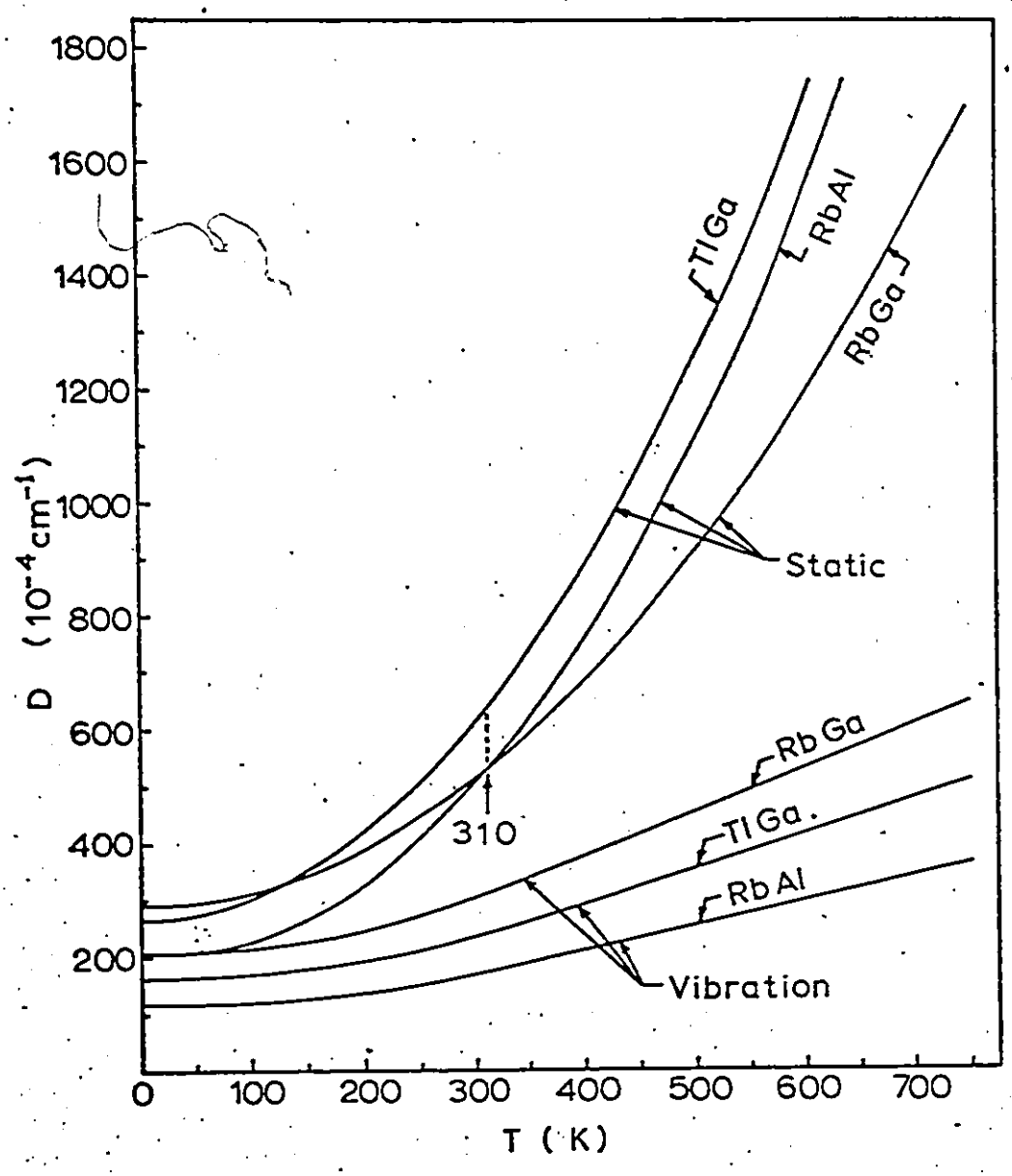

Fig. 6.11 D_S vs T and D_V vs T Curves for the Rb and Tl Alums.

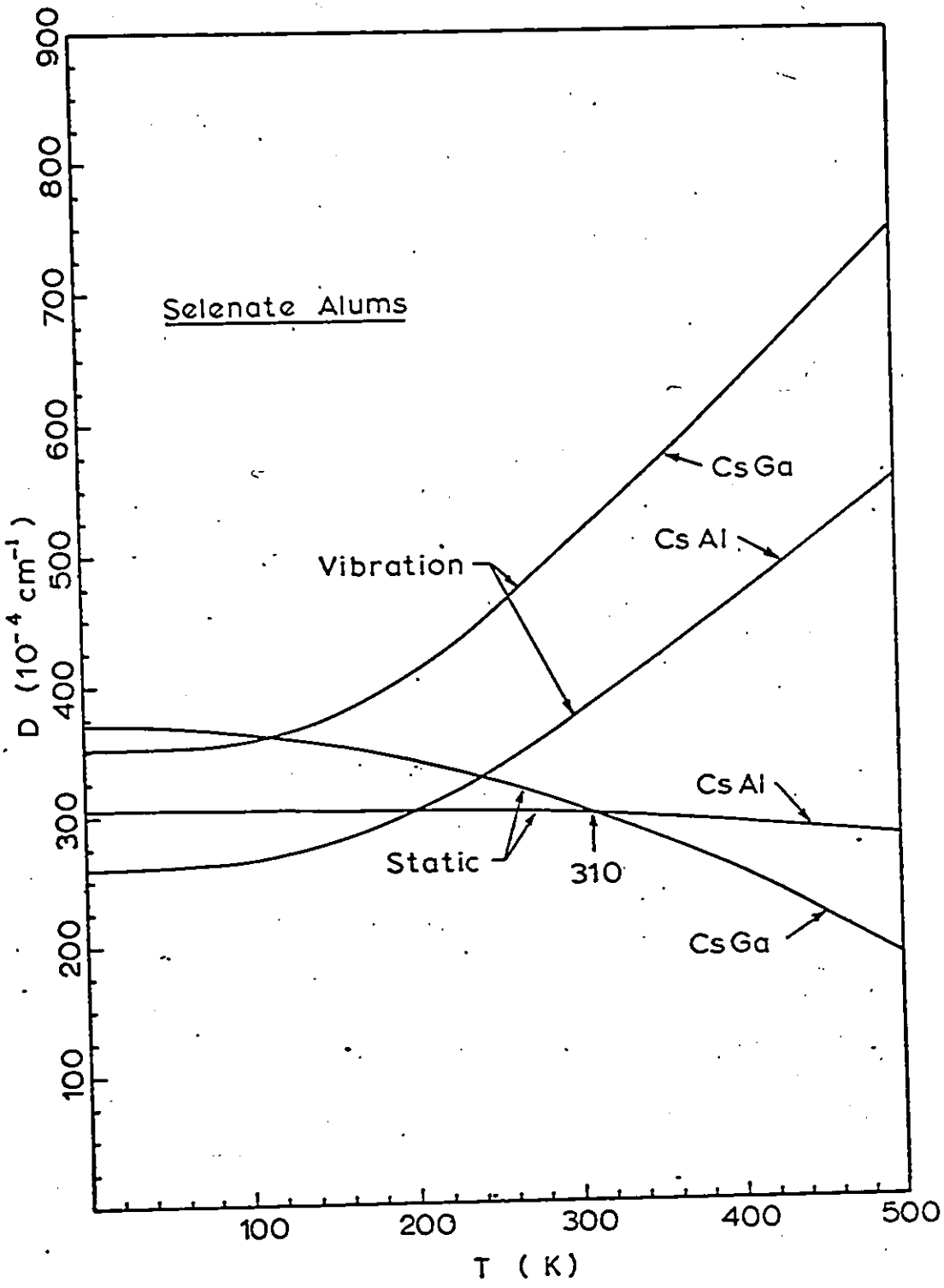

Fig. 6.12 D_S vs T and D_V vs T Curves for the Cs Selenate Alums.

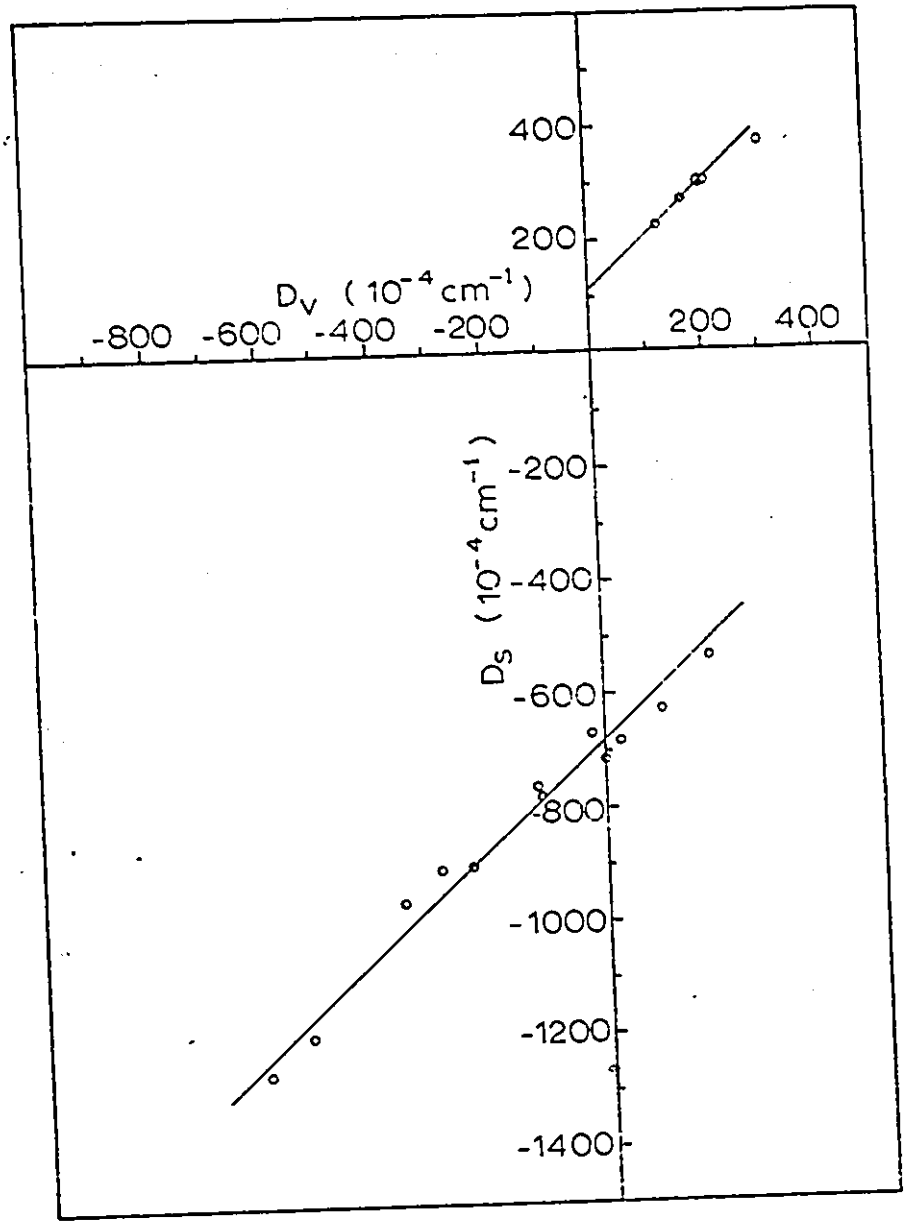

Fig. 6.13 Plot of D_S^o vs D_V^o.

An interesting property exhibited by the splitted D vs T curves is the existence of common crossing points for the related groups of static lines. For the guanidinium salts, as shown in Figs. 6.8 and 6.9, these occur at 280 K. For the alums, as shown in Figs. 6.10 6.11 and 6.12, these occur at 310 K. It is interesting to note that all the static crossing points in the hydrated salts occur near room temperature. The values of D_S at the static crossing points, termed D_{SC}, appear to have a special significance because the values are separated from each other in discrete steps. The D_{SC} values at all the crossing points found in this work are illustrated in Fig. 6.14. Also shown in the figure is the value for TlGa alum taken at 310 K. No ENDOR measurements were taken for the companion salt TlAl alum but its static curve is expected to cross that of TlGa alum at 310 K, as for all the other alums. Since the behavior of $AlCl_3.6H_2O$ cannot be directly compared with the guanidinium salts or the alums, its value of D_{SC} is taken at room temperature (297 K), which is close to the crossing point temperature of all the measured salts. The D_{SC} values of all the salts fall at the points indicated in Fig. 6.14 within an accuracy of $\pm 3(10^{-4}cm^{-1})$, there being no exceptions. The location of the D_{SC} values for the NH_4 and K sulfate alums shown in the figure is a consequence of the analysis described below. The positive and negative D_{SC} values are separated by incremental steps of 115 $(10^{-4}cm^{-1})$ and 165 $(10^{-4}cm^{-1})$, respectively. Using these step values it is possible to predict other values of D_{SC}, and some of these are shown in Fig. 6.14. If the D_{SC} values are represented by integral numbers as indicated in the figure, then it is possible to describe them by the expression

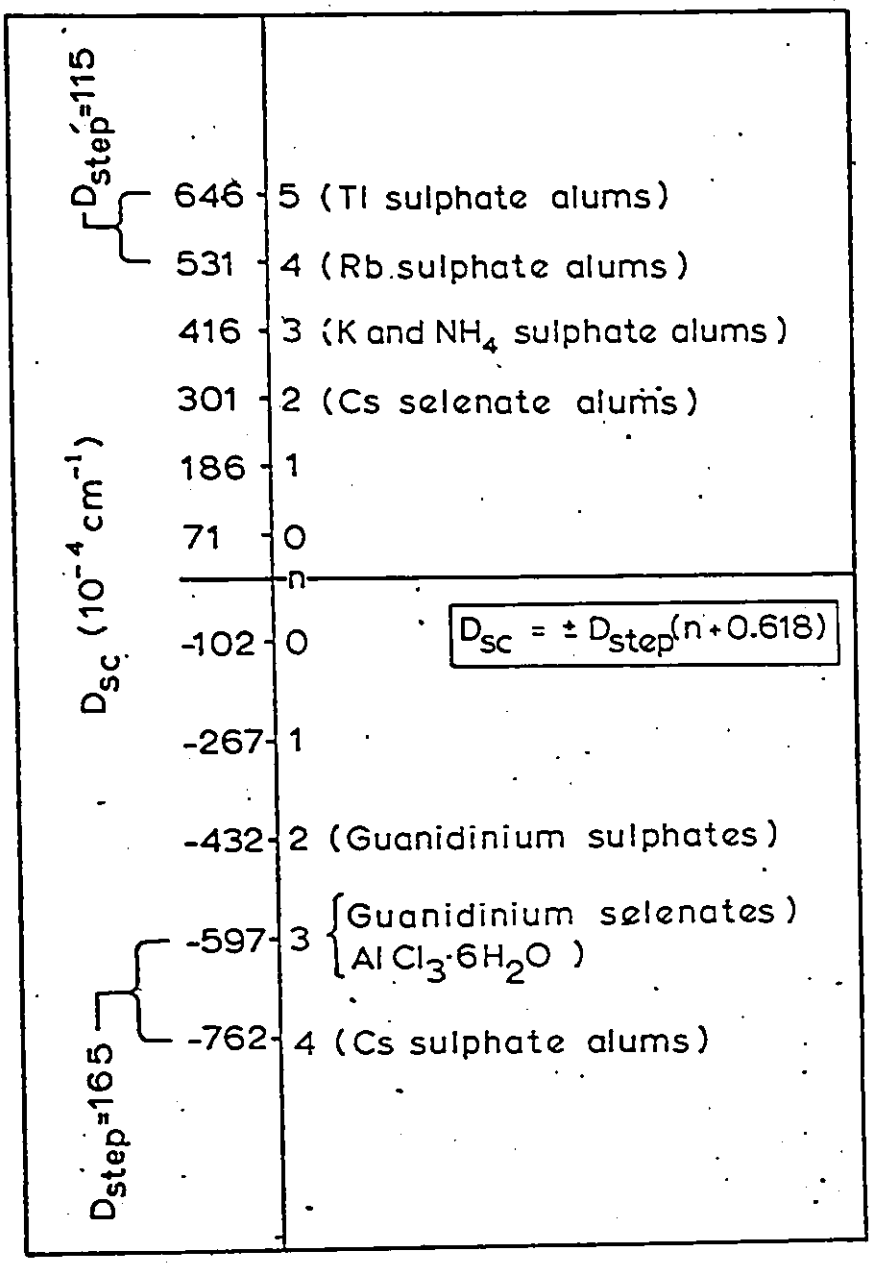

Fig. 6.14 Plot of the D Values at the Static Crossing Points for Cr^{3+} in the Trigonally Distorted Octahedral Sites of Hydrated Crystals.

$$D_{SC} = \pm D_{step}(n + 0.618), \qquad (6.3)$$

where n = 0, 1, 2, 3,..., and $D_{step} = 115(10^{-4}cm^{-1})$ for positive D_{SC}, and $165(10^{-4}cm^{-1})$ for negative D_{SC}. The error of the number 0.618 in the above equation is ±0.001. Fig. 6.14 indicates a relationship that exists between all the trigonally distorted $Cr^{3+}.6H_2O$ magnetic complexes. The implication is that while the individual groups of crystals act in a similar fashion in families, all the crystals are also related to each other as a "race". This situation exists from the point of view of the magnetic behavior of the chromium complexes.

6.4 Splitting Procedure for the D Values of the Ammonium and Potassium Alums

As stated in Chapter 2, the NH_4 and K sulfate alums undergo low temperature phase transitions. However, above the transition temperatures the $Cr^{3+}.6H_2O$ magnetic complexes exhibit axial symmetry as in the other alums. In this section the D vs T curves are split into crystal vibrational and static distortion contributions for the NH_4 and K chromic alums, and for the isomorphs NH_4Al, NH_4Ga, NH_4In, KAl and KGa alums lightly doped with Cr^{3+}. Since the D vs T curves exist only in a limited range of temperature for Cr^{3+} in trigonally distorted sites, the separation into D_S and D_V curves can be successfully achieved only by adhering closely to the relations established above for the crystals which do not undergo low temperature phase transitions. The principal relations that were

established are as follows: (i) The $^{53}Cr^{3+}$ quadrupole interaction parameters measured at 4.2 K for a family of crystal isomorphs fall nearly on a straight horizontal line when plotted against their respective Cr^{3+} D values measured at 4.2 K. The relationship is described by the equation

$$Q' = k_S D_S + k_V D_V,$$

when considering the D vs T curves split into their static and vibrational components. The constants k_S and k_V (with $k_S = -k_V$) are taken to be the same for all the alums, and so the pertinent one has the value $-0.215(10^{-3})$. (ii) The static crossing points of the NH_4 and K alums likely occur at 310 K and fall at one of the values given in Fig. 6.14. In principle the NH_4 and K alums need not have the same value of D_{SC}. (iii) For all the hydrated crystals studied above the average value of θ in Eq. 6.1 is $\theta = 512.0 \pm 0.5$ K. For just the alums the average value is $\theta = 512 \pm 0.1$ K. Hence the value of $\theta = 512$ K is used when analyzing the NH_4 and K alums.

The D values obtained above the phase transition temperatures as listed in Table 5.5 of Chapter 5 are plotted in Figs. 6.15 and 6.16 for the NH_4 and K alums respectively. The lines drawn through the points are a consequence of the analysis described below, and they show the form the D vs T curves would have at low temperature if the chromium magnetic complexes were not affected by phase transitions occuring in the crystals. An observation can be made regarding the nature of the D vs T curves between 195 and 297 K and the existence of phase transitions in the crystals. It is noted in Fig. 6.15 that all the D vs T curves for the NH_4 alums between 195 and 297 K are essentially parallel to each other. The same is true

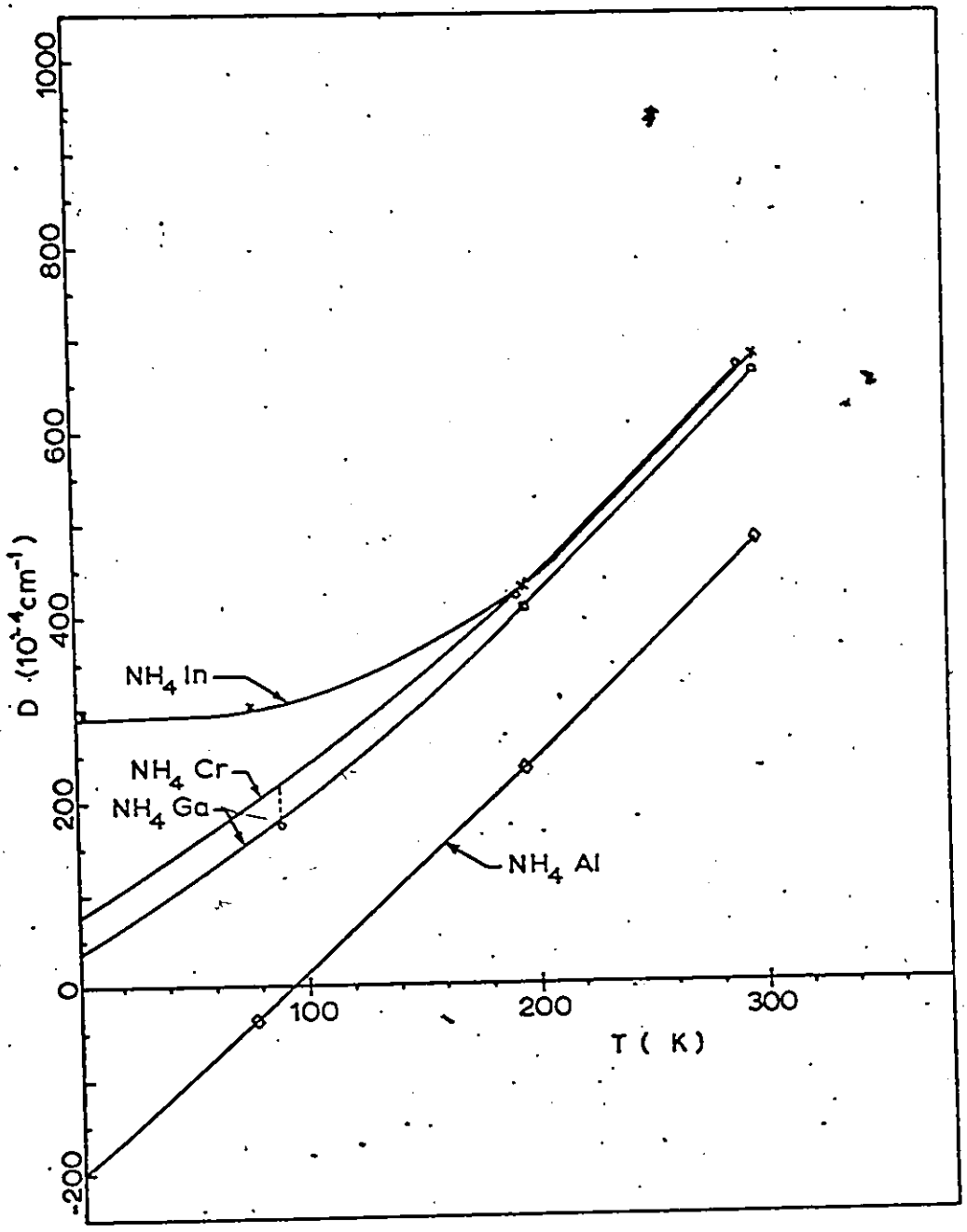

Fig. 6.15 - D vs T Curves for Cr^{3+} in NH_4 Alums.

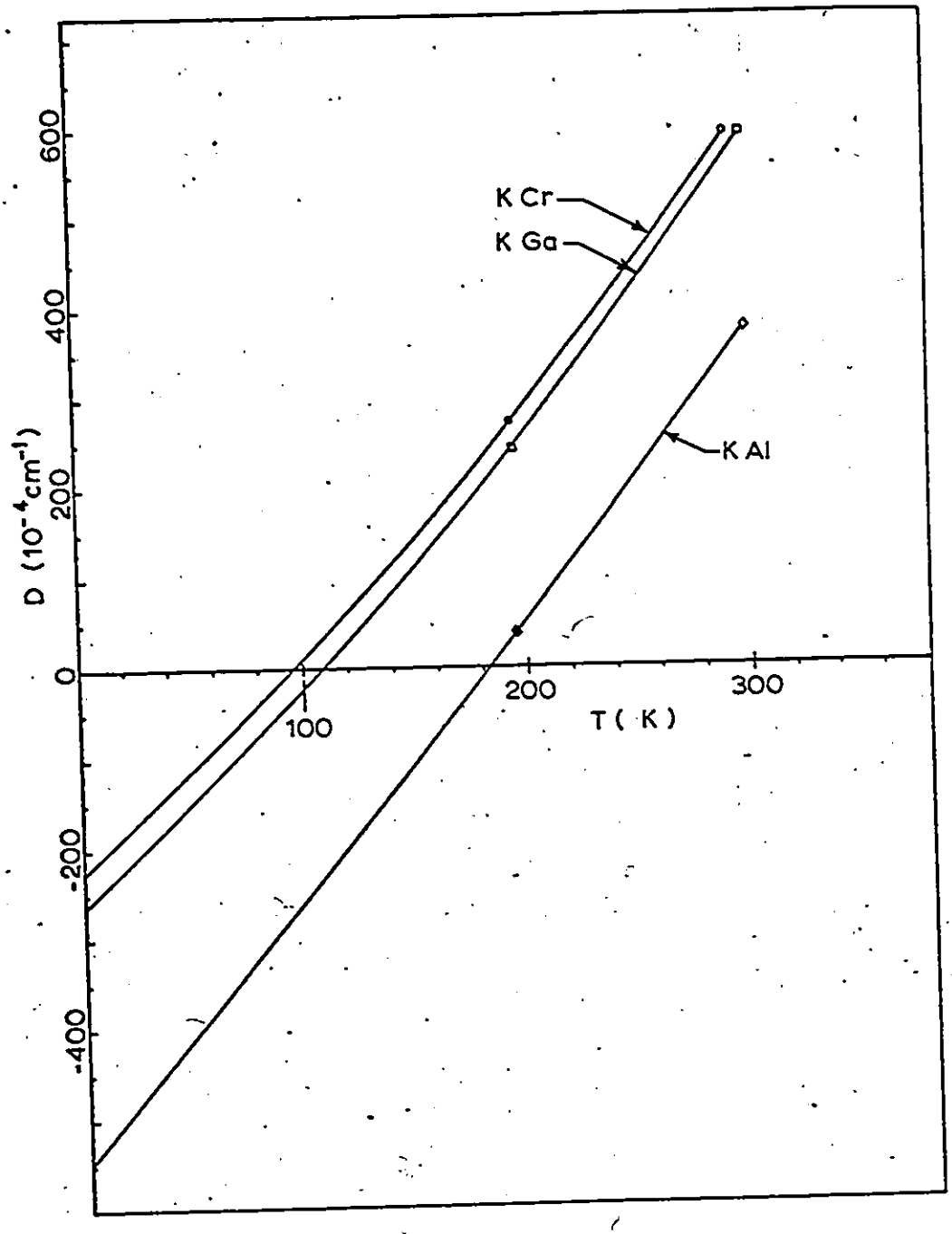

Fig. 6.16 D vs T Curves for Cr^{3+} in K Alums.

for the K alums of Fig. 6.16, but in this case the slope of the lines is different than that of the NH_4 alums. It is evident that the grouping of the lines is dependent on the monovalent ion, i.e. on the crystal, and not on the Cr^{3+} ion. When the straight line parts of all the curves bewtween 195 and 297 K in Figs. 6.15 and 6.16 are extended linearly back to 0 K, they will pass through zero D. This effect can be attributed to the fact that the crystals undergo a particular type of phase transition at low temperature. The actual transition temperatures are not given, however, by the zero D crossing temperatures.

The experimental D values above the phase transition temperatures for the NH_4 and K alums are split into their static and vibrational parts using Eq. 6.1, and by taking into account the three constraints discussed above. The procedure of splitting involves two steps, the first of which gives an approximately correct splitting. The purpose of the first step is to determine the values of the static crossing points, D_{SC}, applicable to the NH_4 and K alums. To achieve this, trial D vs T curves are drawn through the points at 195 and 297 K and the curves are extended to 0 K with arbitrary bends at low temperature. Equation 6.1 is then fitted to the trial curves with the aid of a computer, and the average error between the fit of Eq. 6.1 and the points on the D vs T curve is calculated. This procedure is repeated with new curves determined by the computer, the points of which are average of the original curves and the ones required to fit Eq. 6.1. The points at 195 and 297 K were kept fixed at all times. The approximately correct curves are obtained when an average error of

$\pm 5(10^{-4}cm^{-1})$ exists between the trial curve and Eq. 6.1. This error value is used because it represents the error of the D values when they are measured experimentally. The computer readout values of D, D_S and D_V obtained at the chosen fit are then plotted as a function of temperature. An examination of the static curves showed that the static crossing points of the NH_4 and K alums occurred higher than 310 K but the average positions of the curves for both types of alums were centered closely about a D_S value of 416 $(10^{-4}cm^{-1})$ at 310 K. The centering was so close in the case of the NH_4 alums that a value of $D_{SC} = (416\pm1)(10^{-4}cm^{-1})$ could be predicted without the aid of Fig. 6.14.

The second step of the analysis was similar to the first except that the static curves were constrained to cross at a value of 416 $(10^{-4}cm^{-1})$ at 310 K. In addition, besides obtaining an average error of $\pm5(10^{-4}cm^{-1})$ between the trial curves and Eq. 6.1, the region of best fit was required to conform to Eq. 6.2 for the computer readout values of D_S and D_V at 4.2 K. The final D vs T curves obtained for the NH_4 and K alums are shown in Figs. 6.15 and 6.16 respectively. These curves represent the best fit of Eq. 6.1 to the D values measured at 195 and 297 K, and they show the form the curves would be expected to have at low temperature if the chromium magnetic complexes were not affected by phase transitions. The splitted static and vibrational curves are shown in Figs. 6.17 and 6.18 for the NH_4 and K alums, respectively. The positions of the Q' values calculated at 4.2 K using Eq. 6.2 are shown in Fig. 6.19. The Q' value for NH_4In alum falls on nearly the same straight line as for the

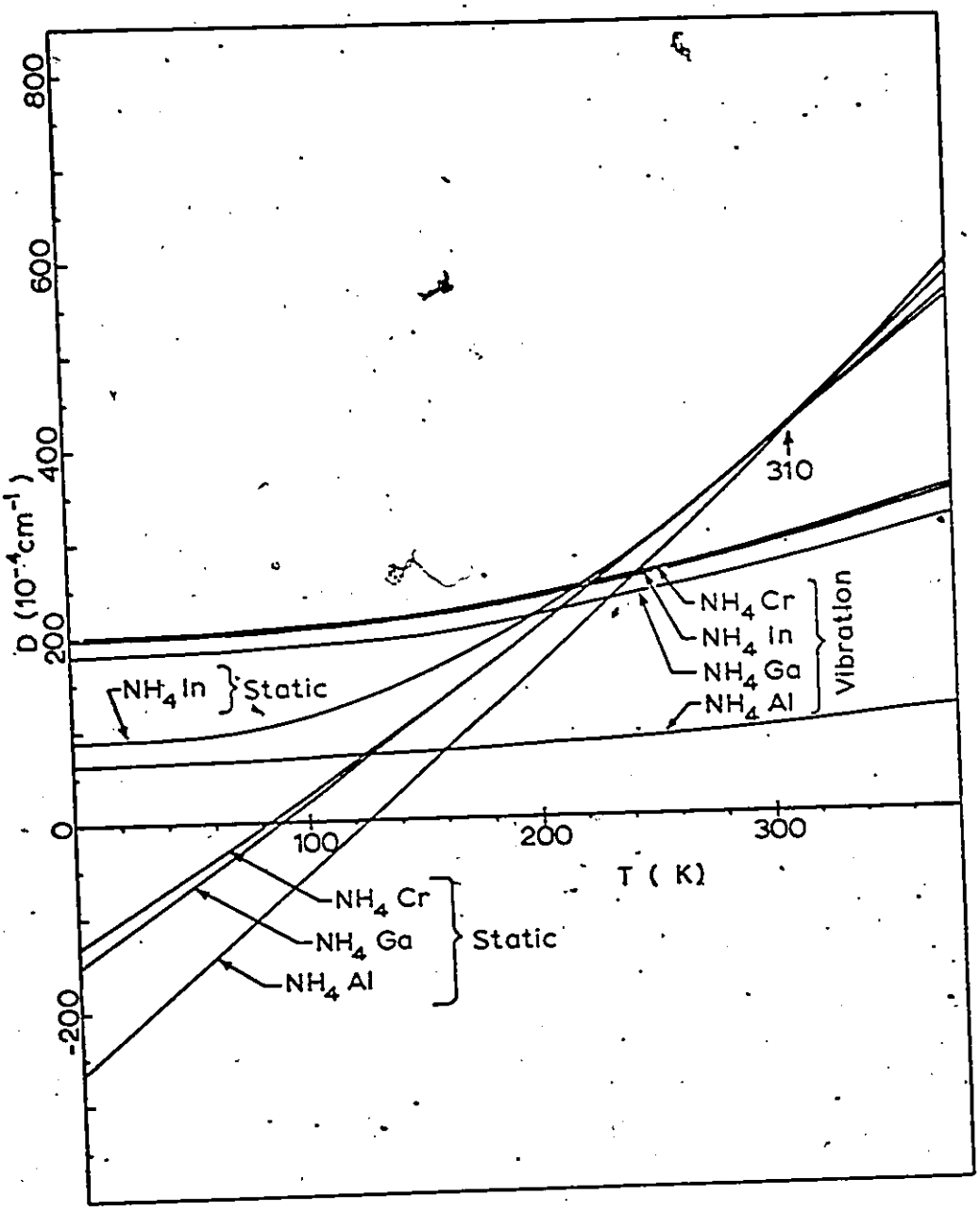

Fig. 6.17 D_S vs T and D_V vs T Curves for the NH_4 Alums.

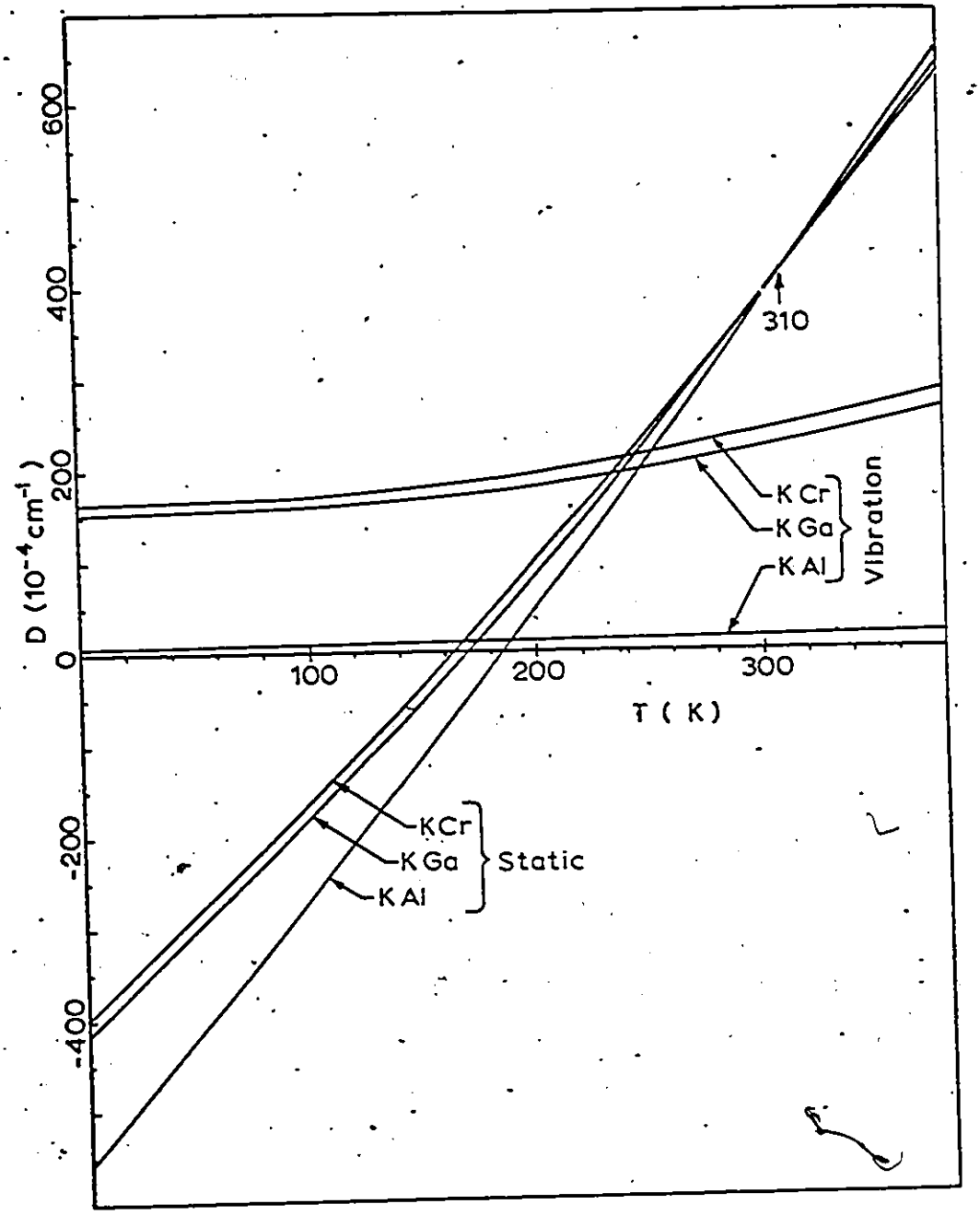

Fig. 6.18 D_S vs T and D_V vs T Curves for the K Alums

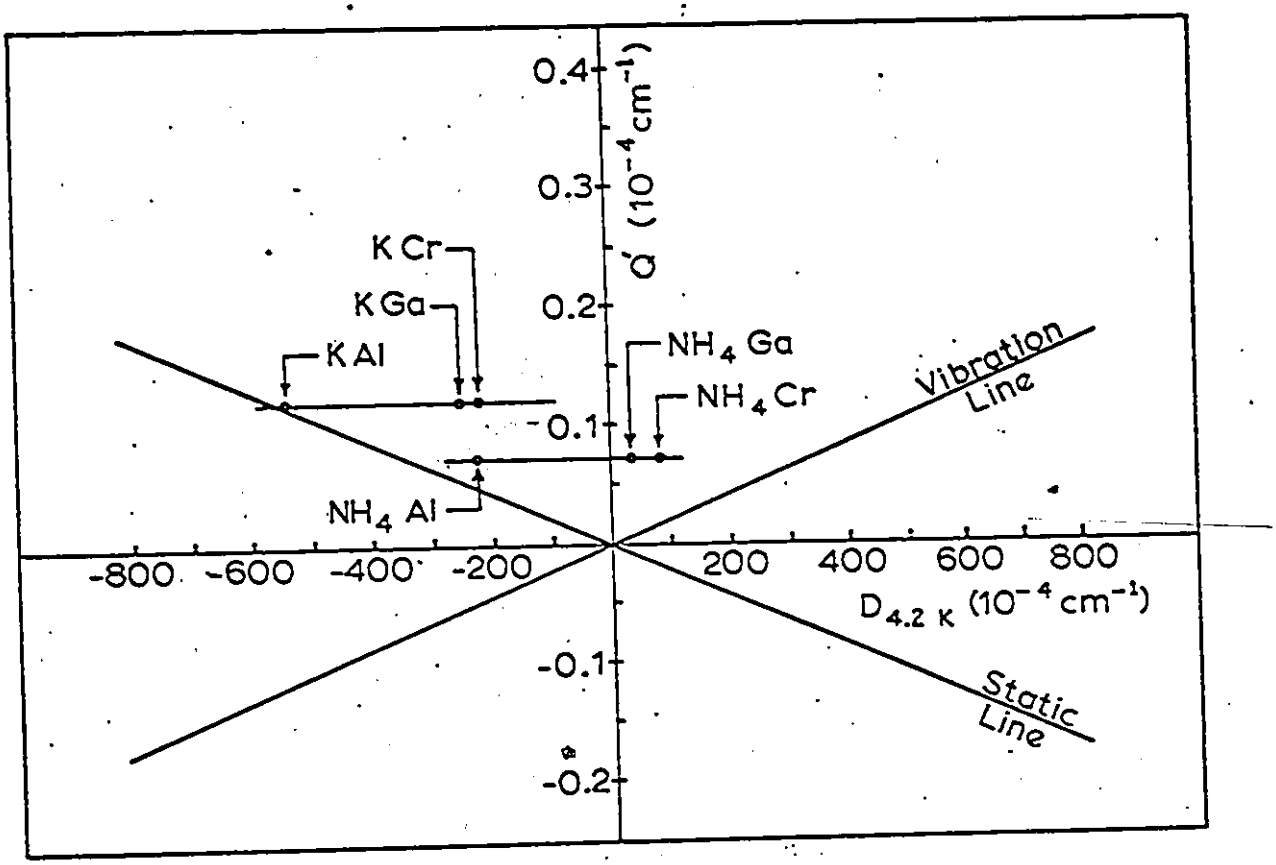

Fig. 6.19 Calculated Values of Q' at 4.2 K vs the Calculated Values of D at 4.2 K for the K and NH_4 Alums.

Rb and Tl alums of Fig. 6.4 and so it is not shown in Fig. 6.19. The values of D_S^o, D_V^o, α and β for the best fit lines are shown in Table 6.2. Also included in the table are the temperatures at which the static curves change sign.

6.5 Splitting of the A and B Hyperfine Parameters into Crystal Vibrational and Static Distortion Contributions

In view of the above analyses, a model is now presented which allows the $^{53}Cr^{3+}$ hyperfine parameters A and B in the hydrated salts to be split into contributions due to crystal vibrational and static distortion effects, in addition to the Fermi contact term. The relationships used in the splitting, which include the three types of contributions, are

$$A = A_S + A_V + K'$$

$$B = B_S + B_V + K'$$

where K' is due to the Fermi contact term, and A_S, A_V, B_S and B_V are contributions to A and B due to the static (subscript S) and vibrational (subscript V) effects of the trigonal crystalline electric field acting on the chromium ion. In this model the static and vibrational parts of A and B are taken to be proportional to the static and vibrational parts of the zero-field splitting parameter D, i.e. of D_S and D_V, found above. The above two equations can then be written as

$$A = a_S D_S + a_V D_V + K' \qquad (6.5)$$

TABLE 6.2 Values of the Parameters D_S^o, D_V^o, α, β, and θ that Occur in the Equation $D = D_S^o (1+\alpha T+\beta T^2)+D_V^o \coth (\theta/2T)$; and the Values T_C, which are the Temperatures at which the Static Curves Change Sign.

ALUM	D_S^o (10^{-4} cm^{-1})	D_V^o (10^{-4} cm^{-1})	α (10^{-4} K^{-1})	β (10^{-6} K^{-2})	θ (K)	T_C (K)
NH_4Cr	-127.8	206.1	-116.53	-6.6165	512	82
NH_4Ga	-150.0	185.3	-112.38	-2.9460	512	87
NH_4Al	-266.1	67.2	- 79.369	-1.0288	512	124
NH_4In	96.1	196.9	- 20.851	41.251	512	...
KCr	-393.2	168.0	- 56.720	-3.0918	512	162
KGa	-410.0	154.1	- 53.154	-3.7914	512	168
KAl	-557.2	7.2	- 51.523	-1.5351	512	184

$$B = b_S D_S + b_V D_V + K' \tag{6.6}$$

In these expressions a_S, a_V, b_S and b_V are constants which must be determined from the experimental measurements of A and B. The analysis is based on the fact that data has been obtained at one temperature (4.2 K in this case) for many chromium magnetic complexes, and that the plotted results show a well-defined law of behavior.

As stated in Chapter 3, McGarvey has given the following first-order expressions to describe the A and B parameters:

$$A = P[(4/21)(1-2a^2+b^2)-K] \tag{3.9}$$

$$B = P[-(2/21)(1-2a^2+b^2)-K] \tag{3.10}$$

The first term in the square brackets arises from the effect of the static crystal field on the electron-nuclear dipole-dipole interaction, while the K term is the isotropic contribution due to the Fermi contact term. Equations 3.9 and 3.10 can be written as

$$A = 2P\Delta + K' \tag{6.7}$$

$$B = -P\Delta + K' \tag{6.8}$$

where $K' = -PK$ and $\Delta = (2/21)(1-2a^2+b^2)$. Since the first terms in Eqs. 6.7 and 6.8 represent contributions to A and B due to the static effect of the trigonally distorted crystalline electric field, then they can be written as

$$A = A_S + K' \tag{6.8}$$

$$B = B_S + K' \tag{6.10}$$

with $A_S = -2B_S$. The prescription for parameter splitting dictated by Eqs. 6.7 and 6.8, for given values of A and B with positive or negative D, is shown diagrammatically in Fig. 6.20. The situation shown there is that of a constant K' and Δ for both sets of points, with the condition $A_S = -2B_S$ being satisfied. In general, a different combination of K' and Δ is obtained for each set of points with the condition $A_S = -2B_S$ being satisfied.

The values of A and B measured at 4.2 K, as listed in Table 5.18, are plotted against the corresponding D values at the top of Fig. 6.21. The points shown there for NH_4 and K alums are not measured values, but are predicted on the basis of the analysis described below. The room temperature plot of all the points shown at the bottom of the figure are also predicted results. The experimental A values measured at 4.2 K fall nearly on a straight line. In the analysis procedure the measured A values are fitted to Eq. 6.5 along with the corresponding values of D_S and D_V evaluated at 4.2 K, using a least square fit computer program. This step determines values of $a_S = 1.7352(10^{-4}cm^{-1})$, $a_V = 1.6136(10^{-4})$ and $K' = 17.306(10^{-4}cm^{-1})$ for all the complexes taken together. It is reasonable that K' should be nearly the same for all the $Cr^{3+}.6H_2O$ magnetic complexes because in each case the six waters coordinated to the chromium ion are known to form nearly regular octahedra of essentially the same size. Using the value of $K' = 17.306\ (10^{-4}cm^{-1})$, Eq. 6.6 is then fitted to the B values in each of the two branches shown at the top of Fig. 6.21.

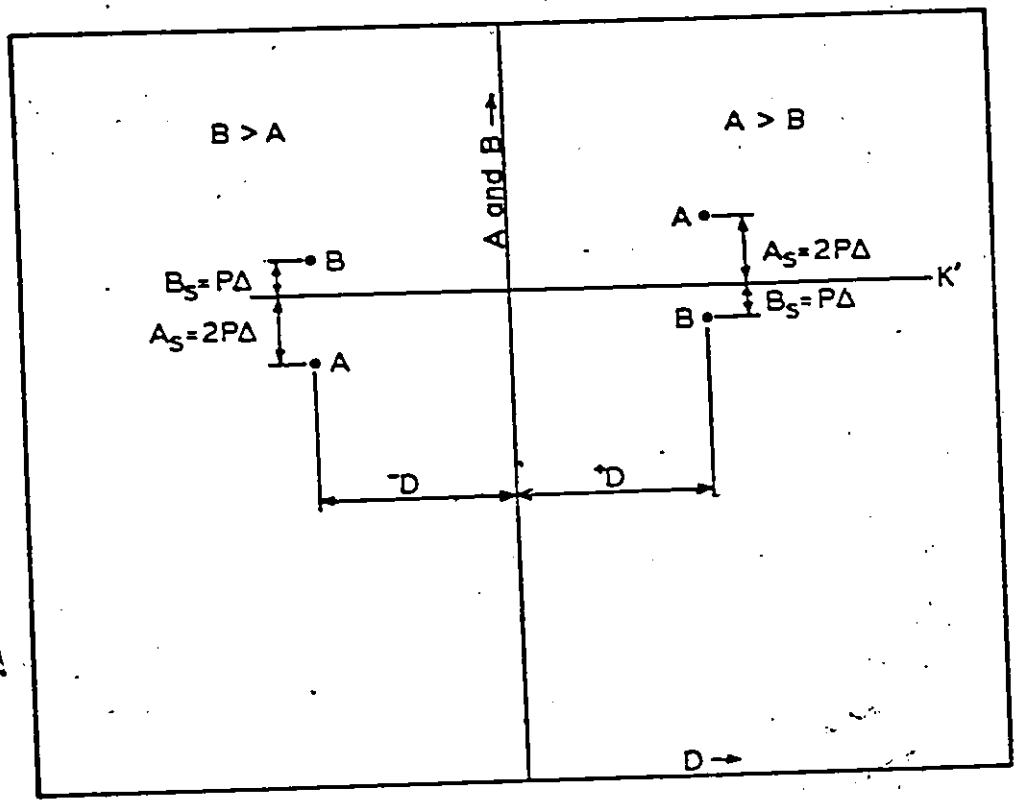

Fig. 6.20 Diagram Illustrating Equations 6.7 and 6.8 for D Positive and for D Negative.

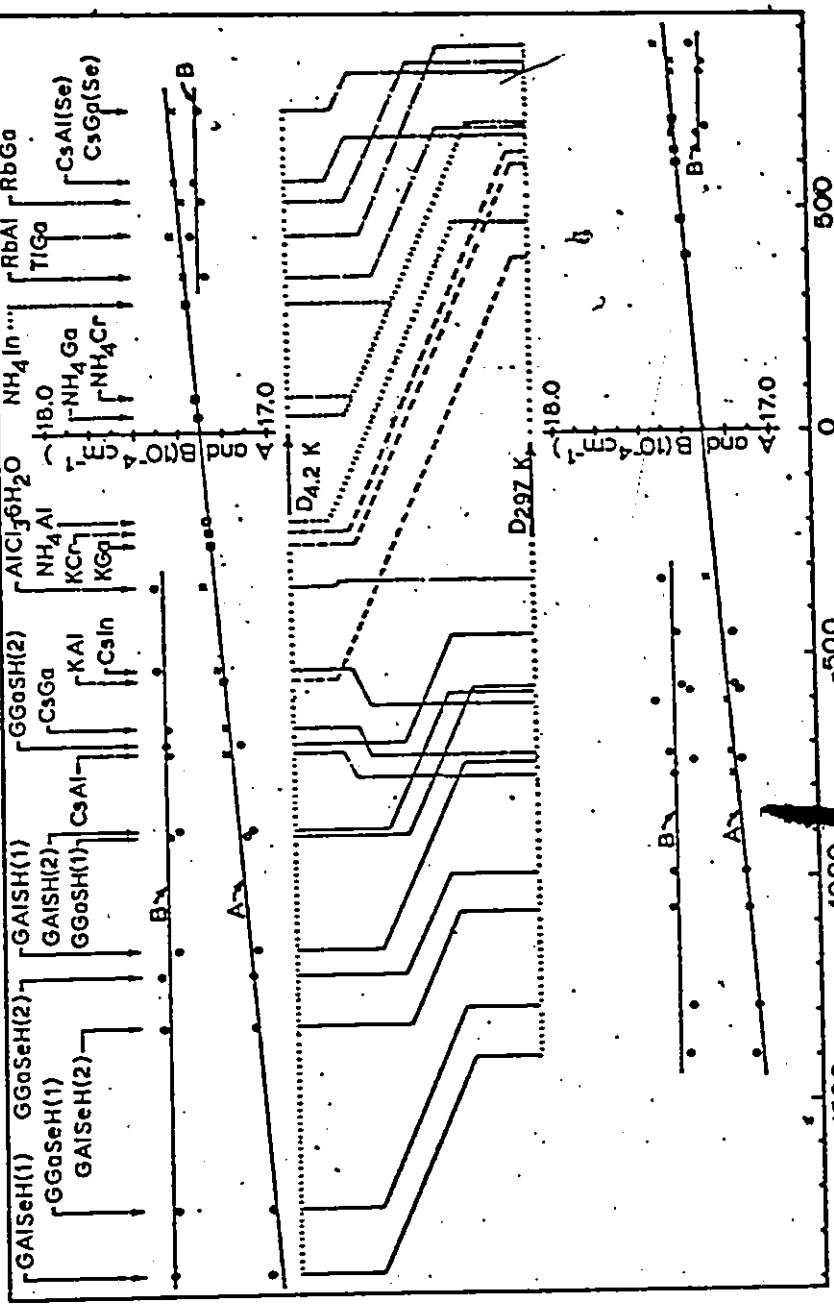

Fig. 6.21 Plots of A vs D and B vs D at 4.2 K and at 297 K.

For the positive D branch one obtains $b_S = -1.642(10^{-5})$ and $b_V = 1.7223$ (10^{-6}), while for the negative D branch $b_S = -1.3534(10^{-4})$ and $b_V = -1.9576$ (10^{-4}).

With the known values of a_S, a_V, b_S, b_V and K' it is possible to plot the temperature dependence of A and B for each magnetic complex using Eqs. 6.5 and 6.6 because the temperature dependence of D_S and D_V is known. These graphs are produced in Figs. 6.28 to 6.39, along with the individual graphs of A_S, A_V, B_S and B_V. Since the NH_4 and K alums undergo low temperature phase transitions, then the low temperature part of the curves in Figs. 6.35 to 6.39 belonging to these salts represents hypothetical values expected if the chromium magnetic complexes were not affected by the phase transitions occuring in the crystals. The predicted curves for the NH_4 and K alums are obtained by substituting their values of D_S and D_V into Eqs. 6.5 and 6.6, along with K' = 17.306 $(10^{-4}cm^{-1})$. The predicted A values for NH_4 and K alums at 4.2 K, taken from Figs. 6.35 and 6.37, are shown in the top graph of Fig. 6.21. The B values are obtained using the values of b_S and b_V belonging to the positive D branch. The ones belonging to the negative D branch were found to give an extremely large temperature variation in B, and so had to be ruled out. The predicted B values are not shown in Fig. 6.21 so as not to obscure the diagram.

Since the A and B curves shown in Figs. 6.22, 6.25, 6.28, 6.31 and 6.33 are derived using the least square fit values of a_S, a_V and K', then the positions of the curves will be shifted slightly vertically from

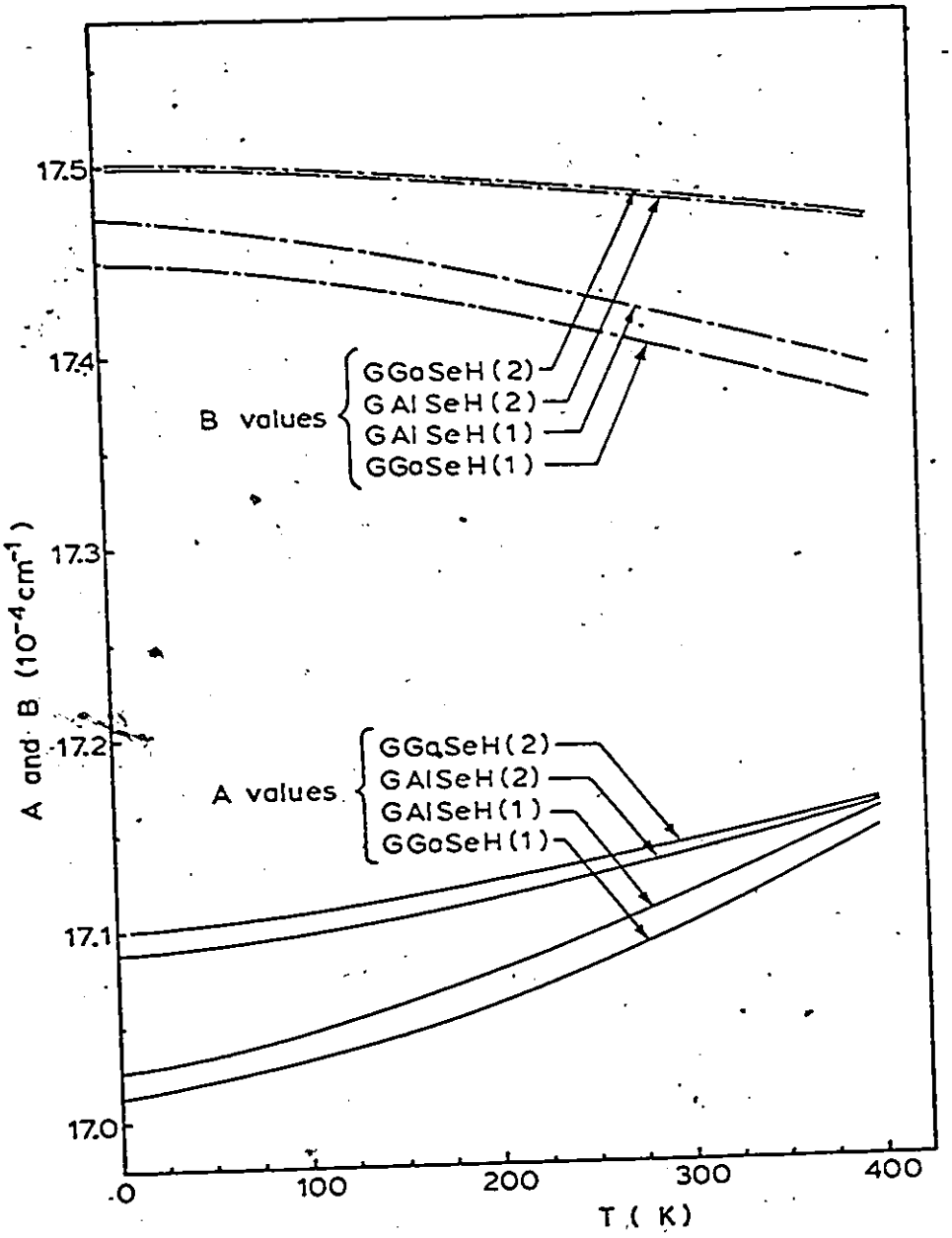

Fig. 6.22 Temperature Dependence of A and B for the Guanidinium Selenate Salts.

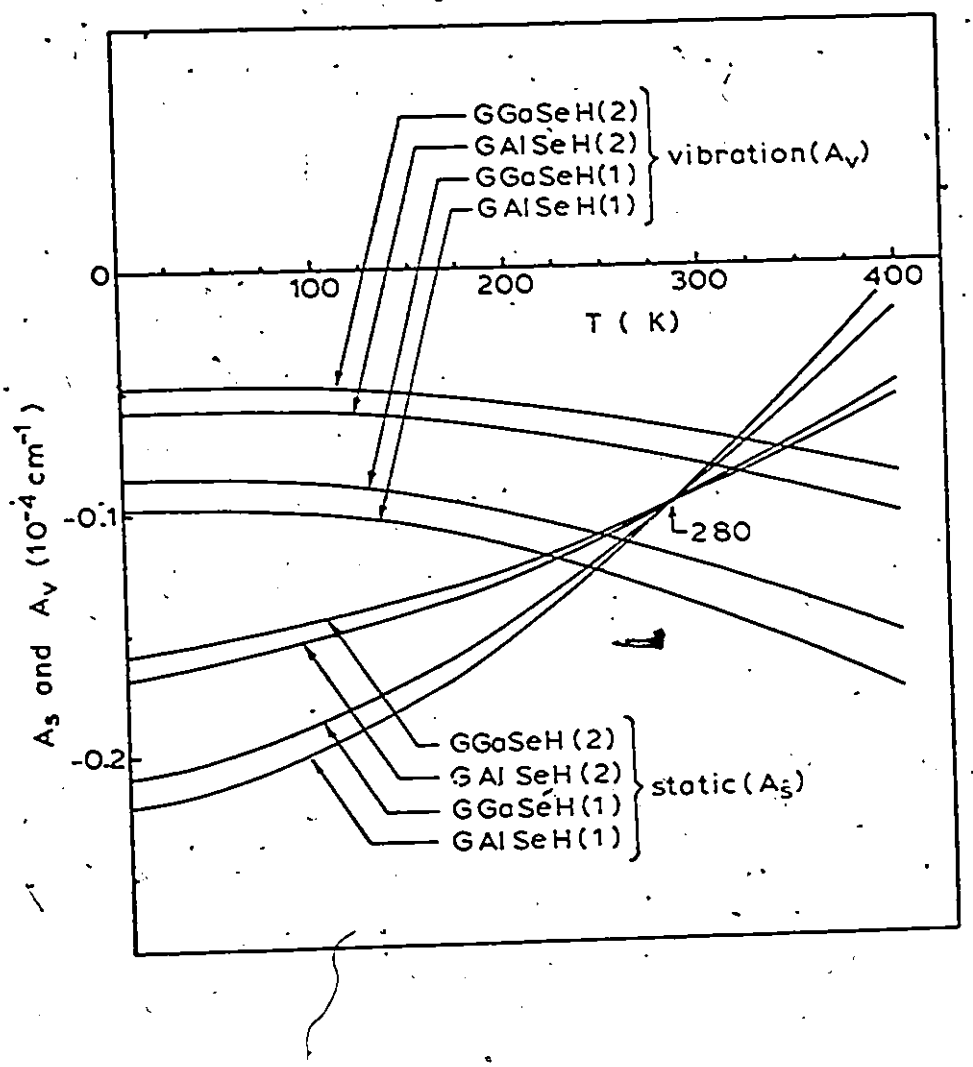

Fig. 6.23 Temperature Dependence of A_S and A_V for the Guanidinium Selenate Salts.

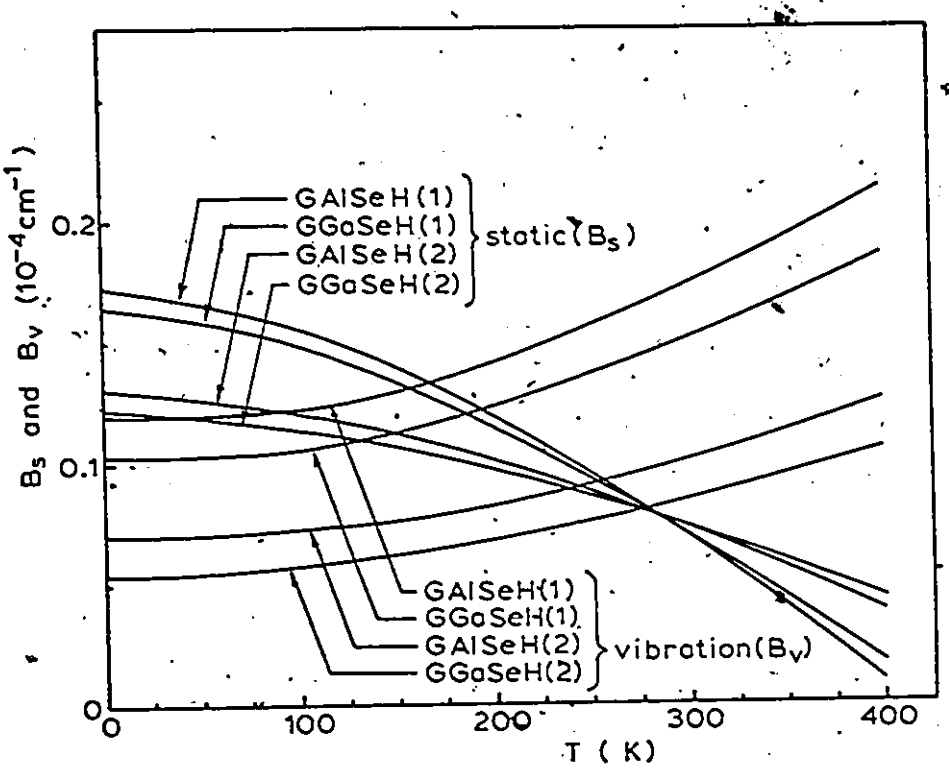

Fig. 6.24 Temperature Dependence of B_S and B_V for the Guanidinium Selenate Salts.

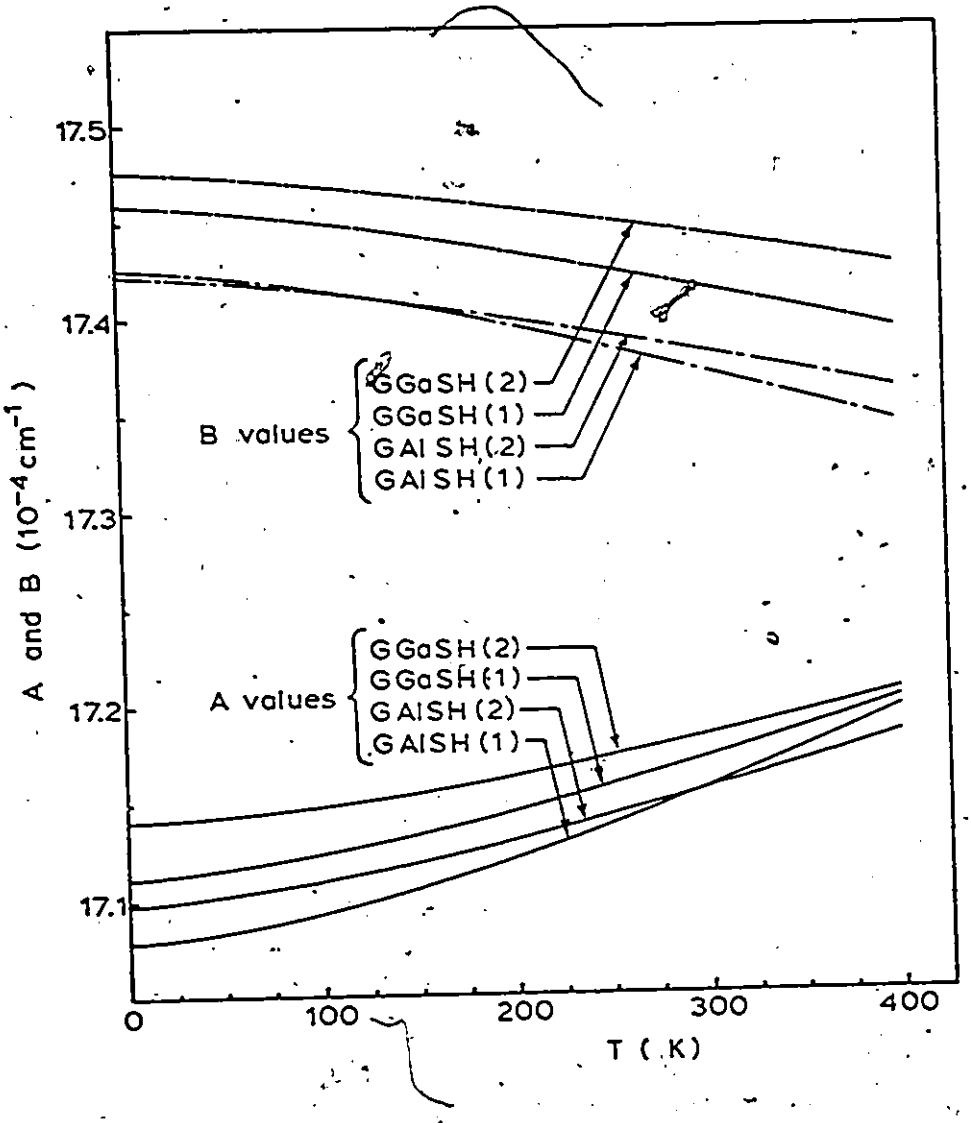

Fig. 6.25 Temperature Dependence of A and B for the Guanidinium Sulfate Salts.

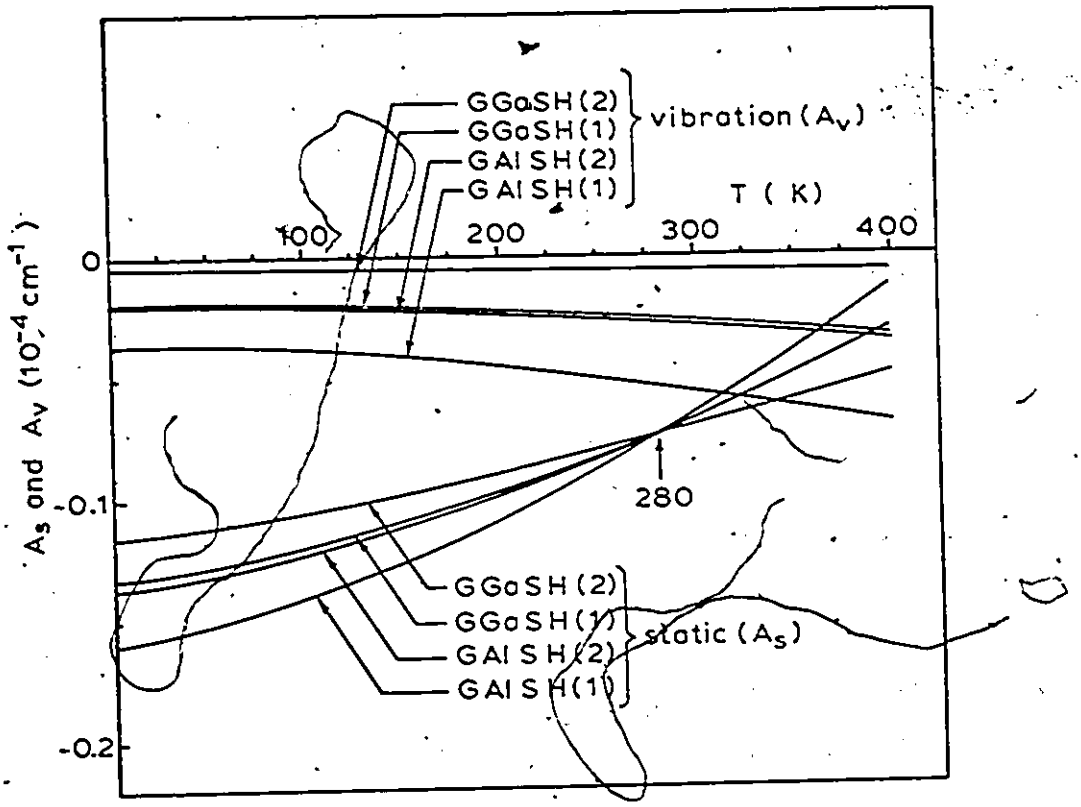

Fig. 6.26 Temperature Dependence of A_S and A_V for the Guanidinium Sulfate Salts.

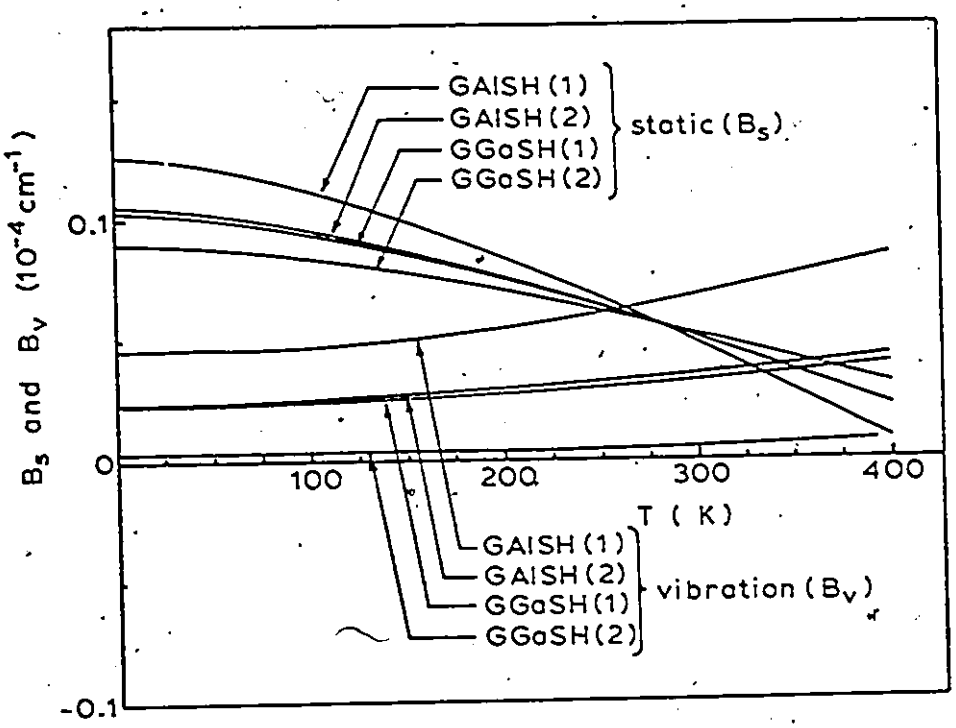

Fig. 6.27 Temperature Dependence of B_S and B_V for the Guanidinium Sulfate Salts.

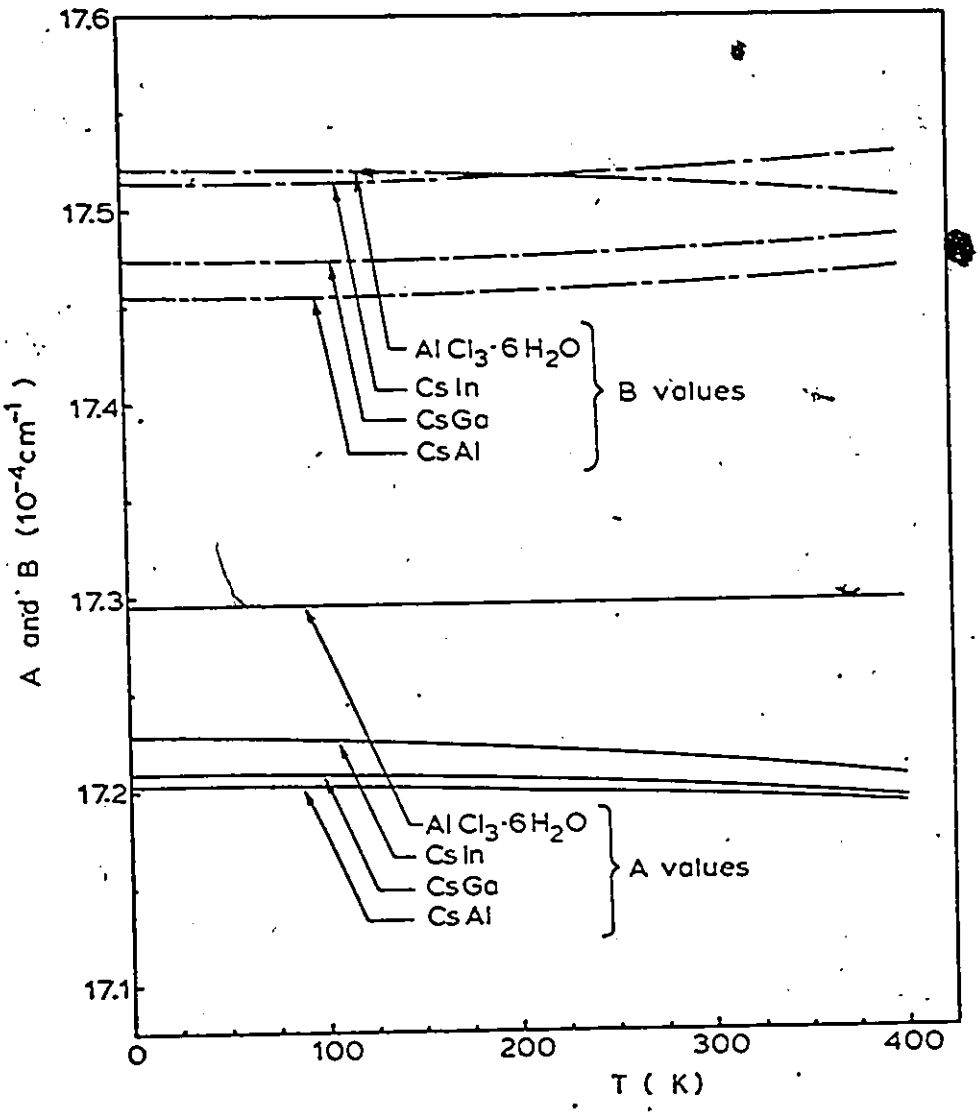

Fig. 6.28 Temperature Dependence of A and B for the Cs Sulfate Alums and for $AlCl_3.6H_2O$.

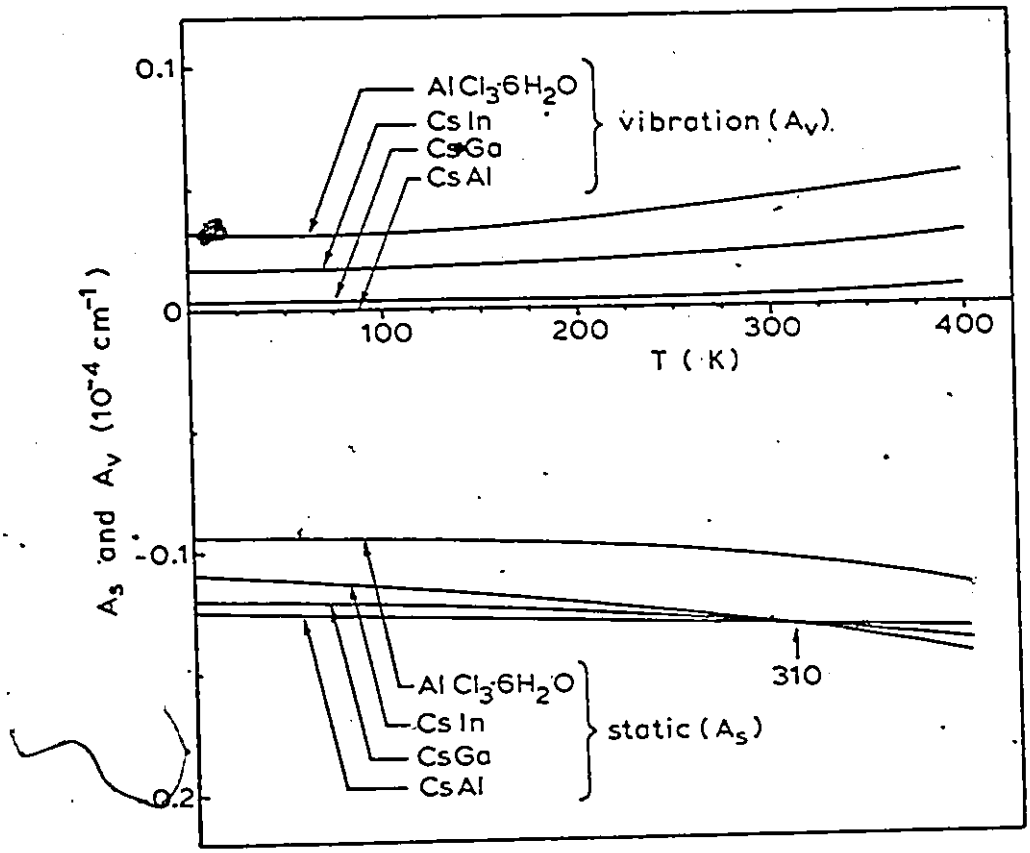

Fig. 6.29 Temperature Dependence of A_S and A_V for the Cs Sulfate Alums and for $AlCl_3.6H_2O$.

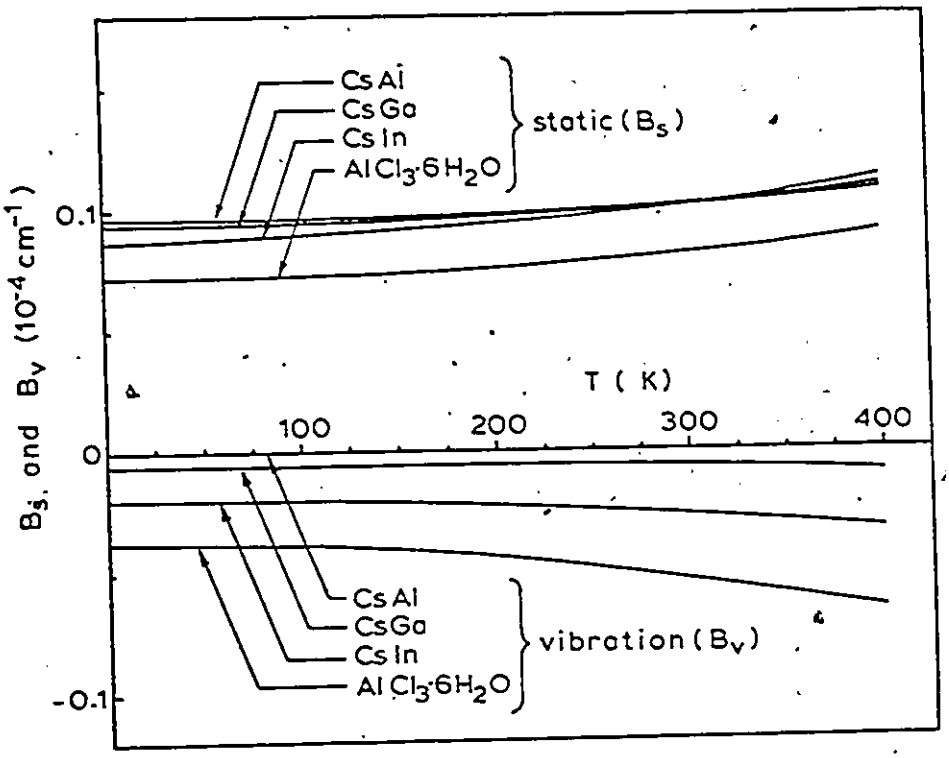

Fig. 6.30 Temperature Dependence of B_S and B_V for the Cs Sulfate Alums and for $AlCl_3.6H_2O$.

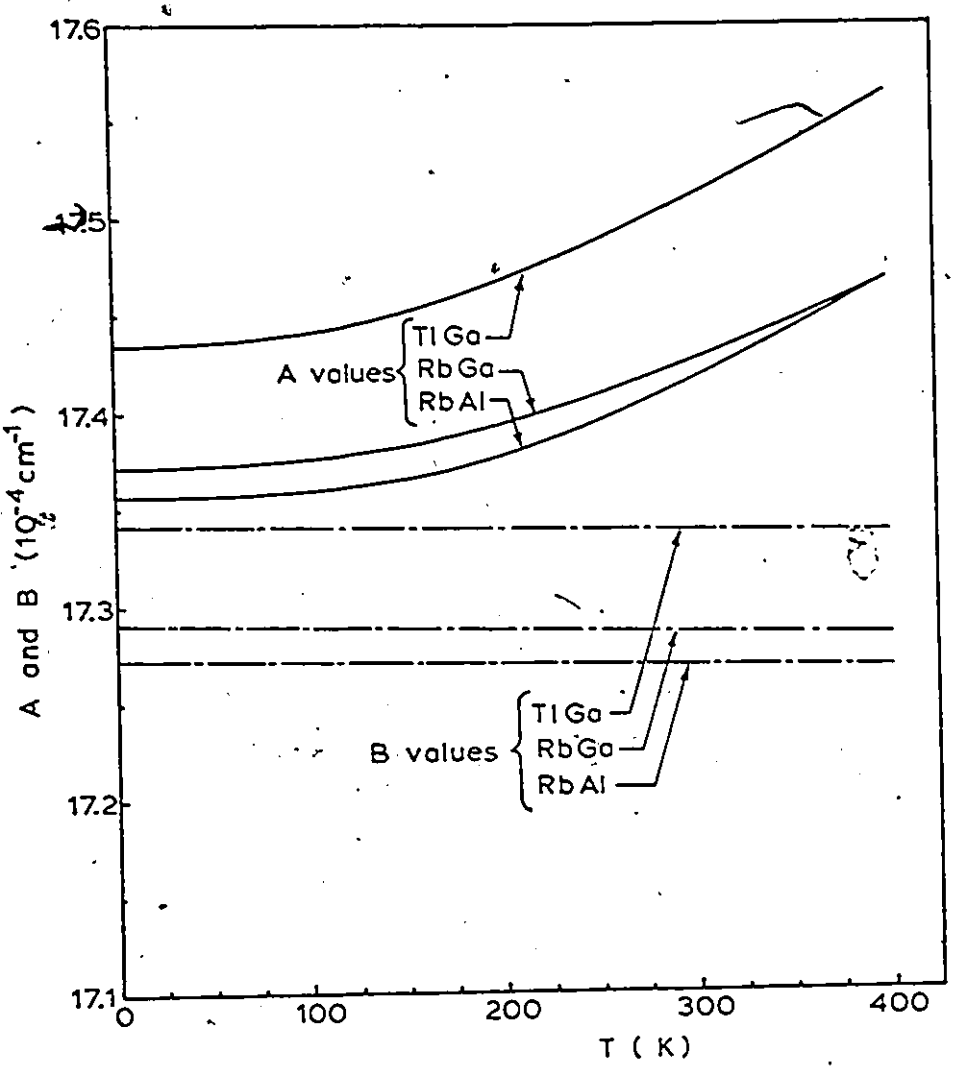

Fig. 6.31 Temperature Dependence of A and B for the Tl and Rb Alums.

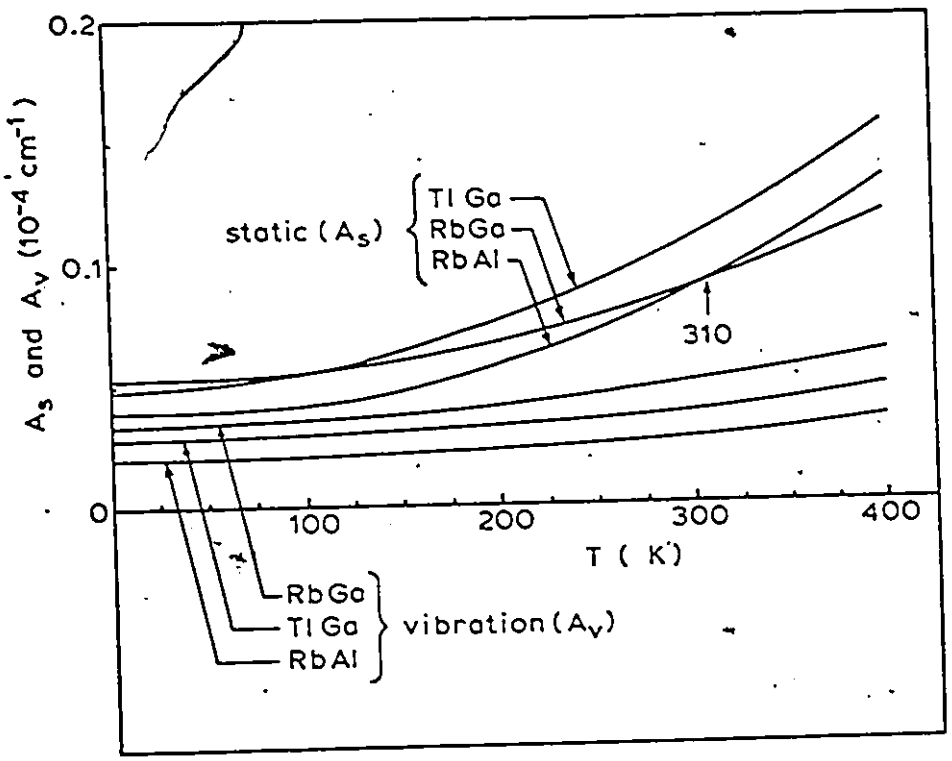

Fig. 6.32 Temperature Dependence of A_s and A_v for the Tl and Rb Alums.

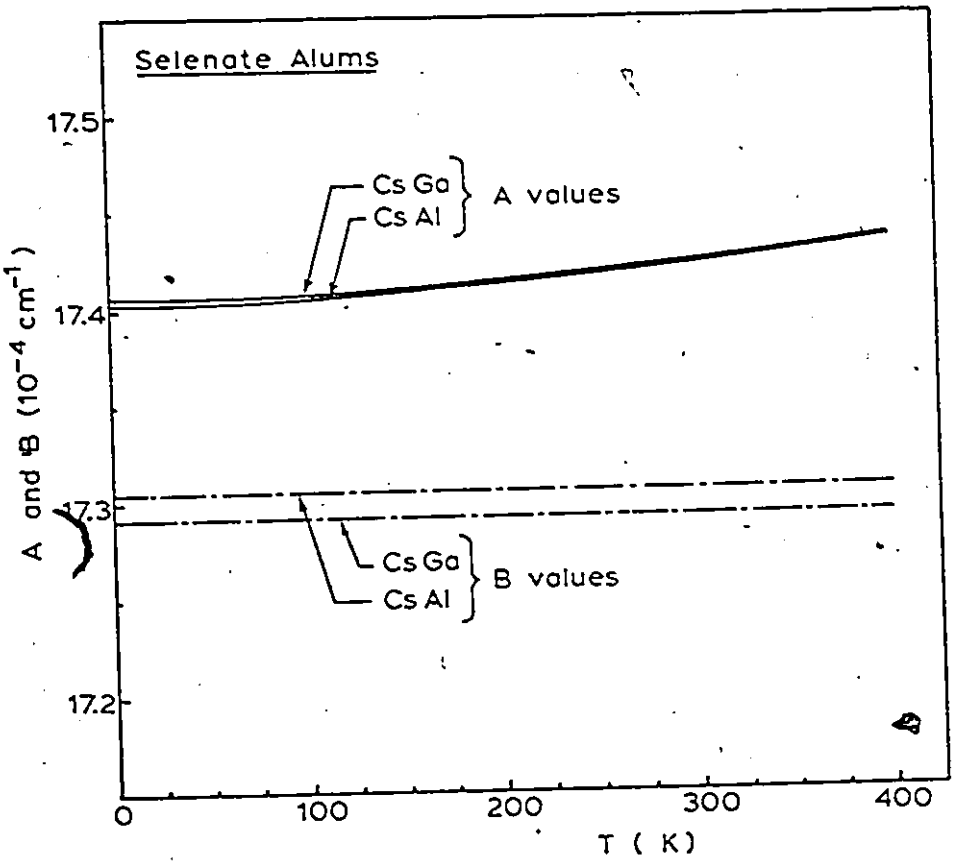

Fig. 6.33 Temperature Dependence of A and B for the Cs Selenate Alums.

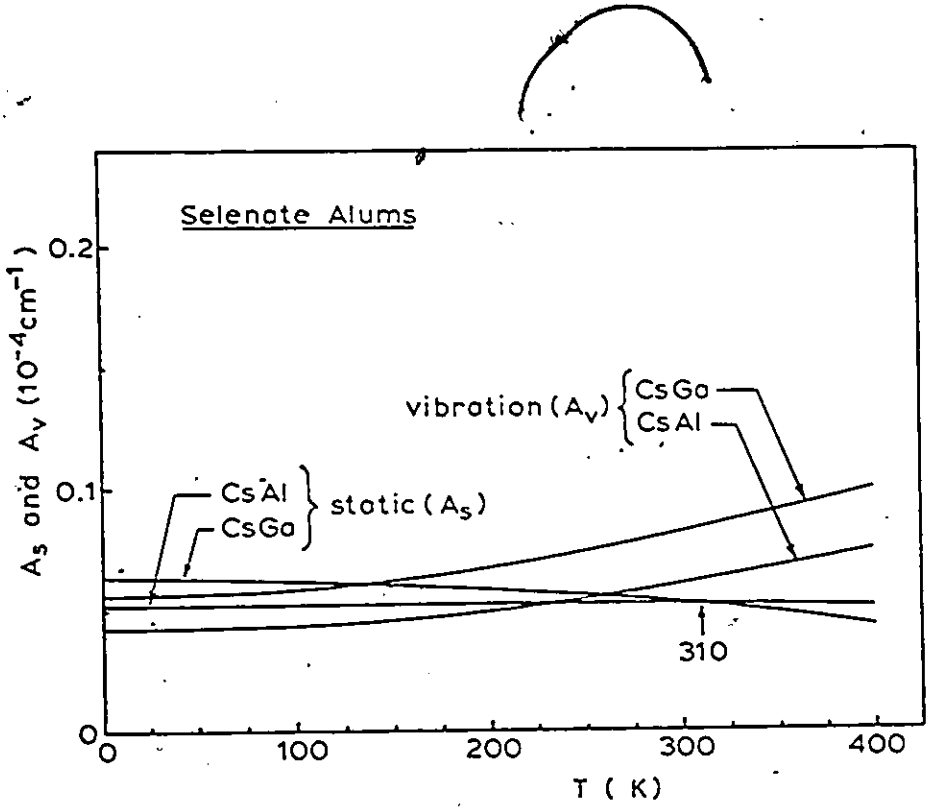

Fig. 6.34 Temperature Dependence of A_S and A_V for the Cs Selenate Alums.

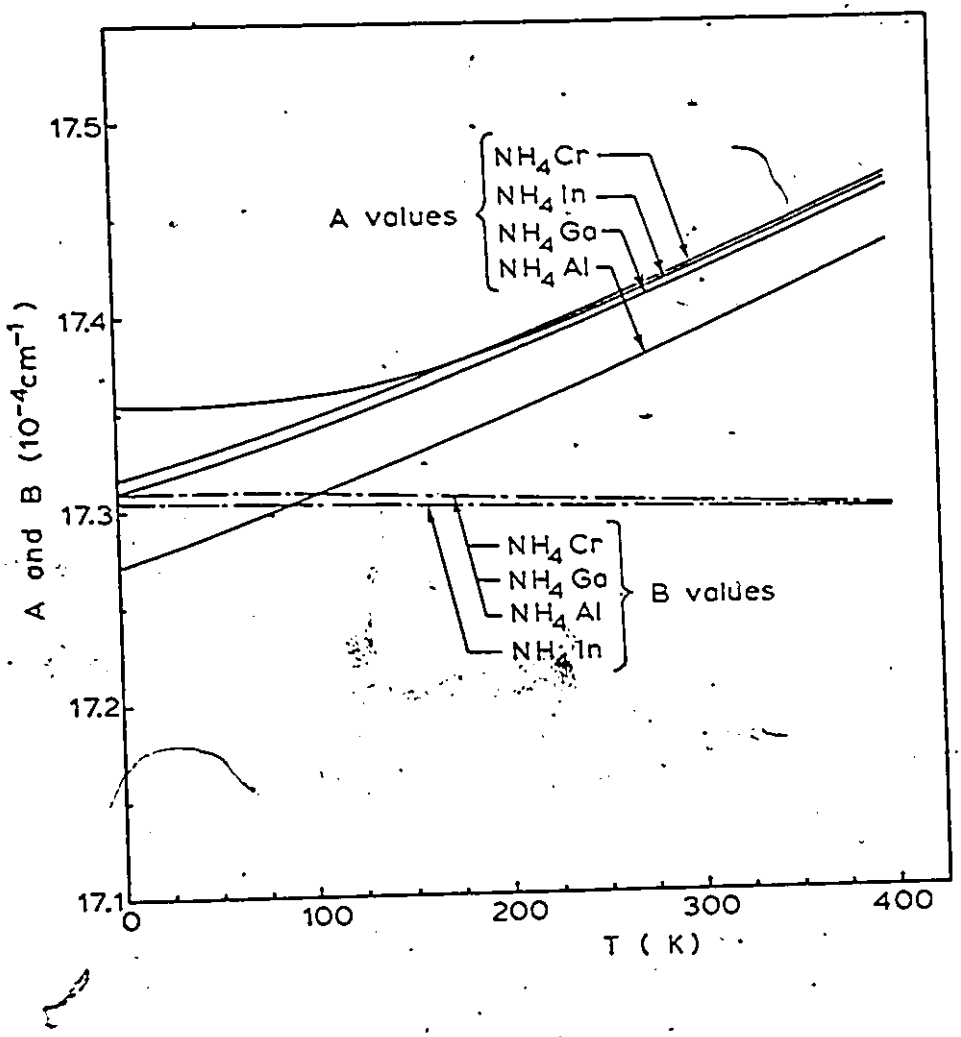

Fig. 6.35 Temperature Dependence of A and B for the NH_4 Alums.

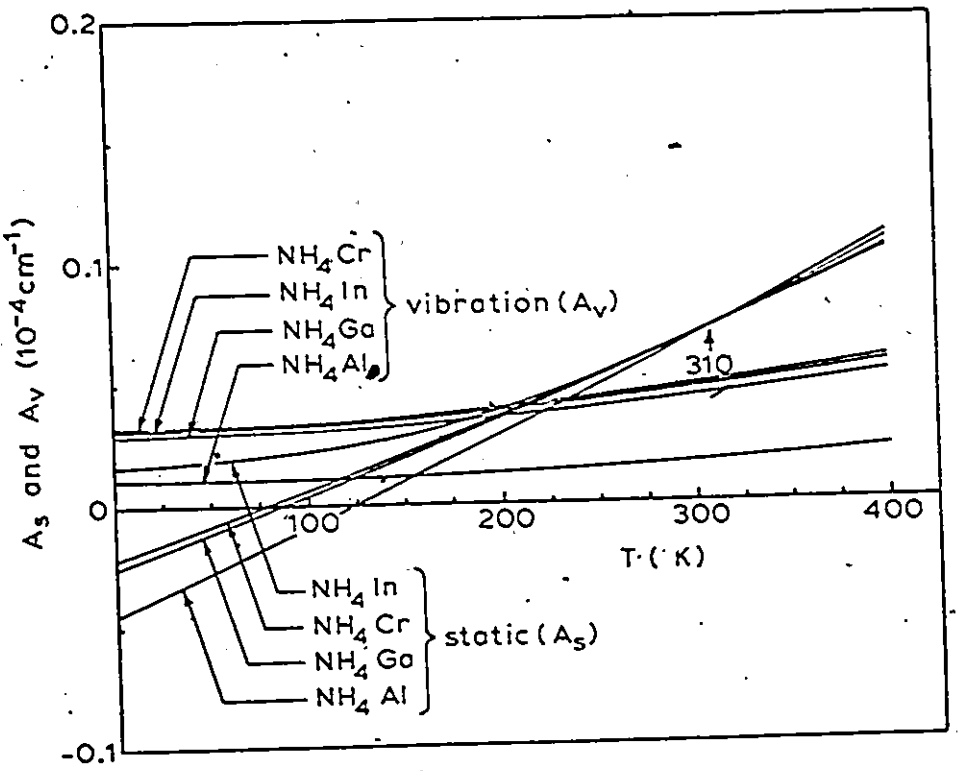

Fig. 6.36 Temperature Dependence of A_S and A_V for the NH_4 Alums.

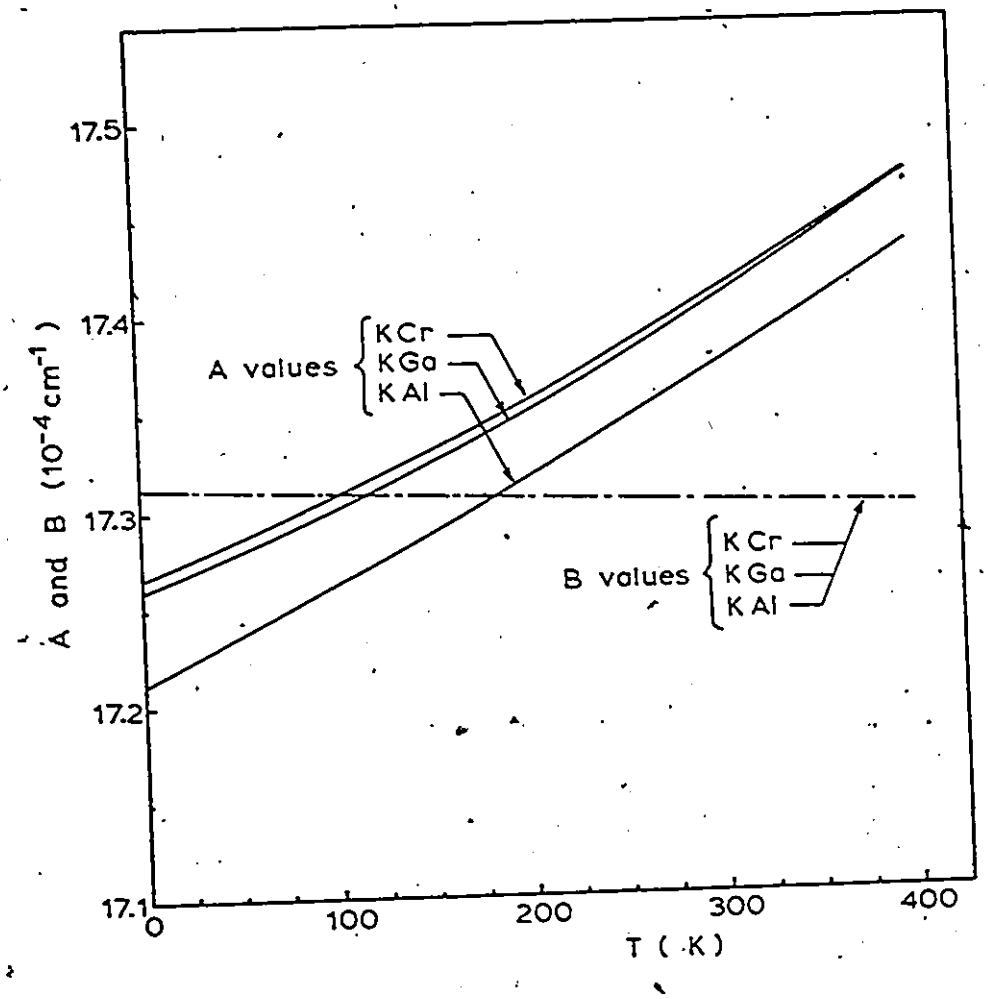

Fig. 6.37 Temperature Dependence of A and B for the K Alums.

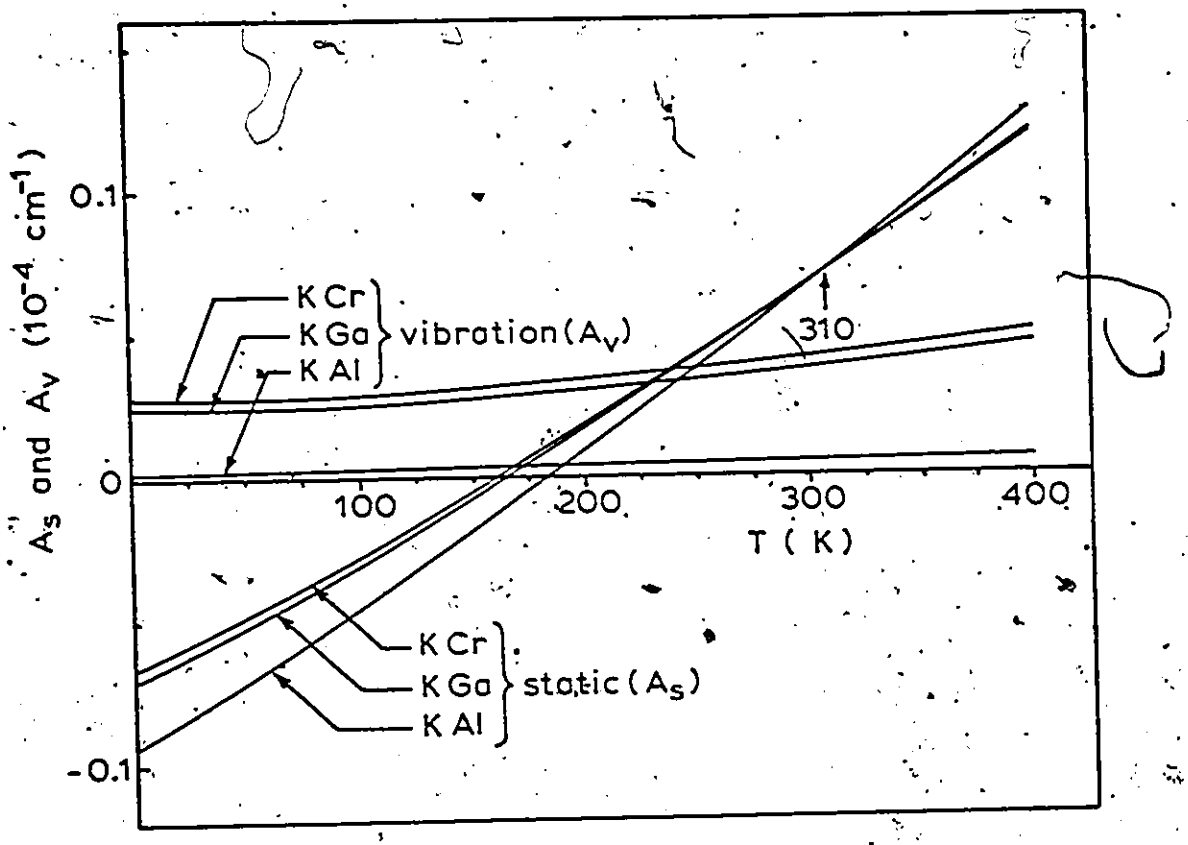

Fig. 6.38 Temperature Dependence of A_S and A_V for the K Alums.

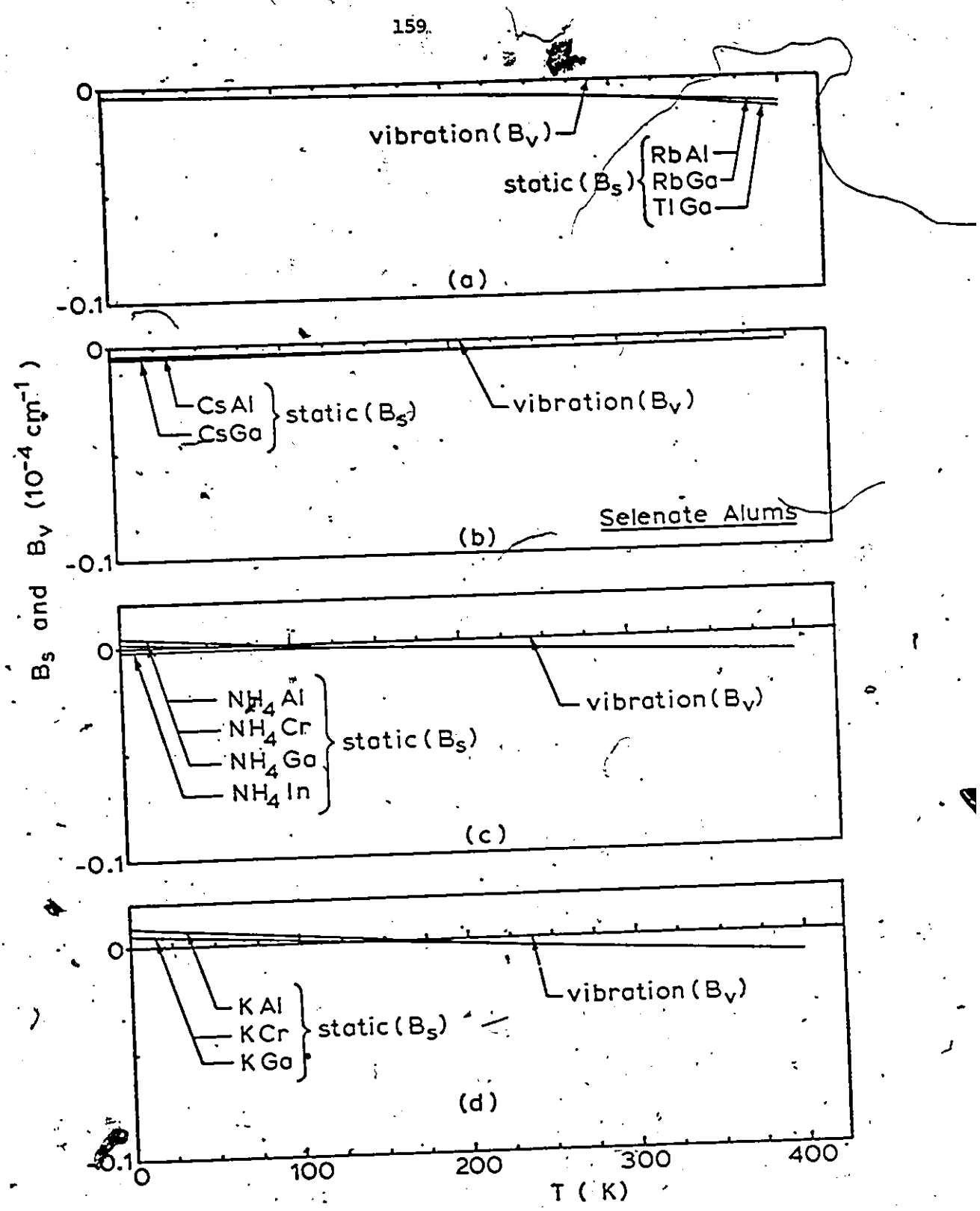

Fig. 6.39 Temperature Dependence of B_S and B_V for the Cs Selenate Alums and for the Rb, Tl, NH_4 and K Sulfate Alums.

the measured values at 4.2 K. This is because the points in the original graph, at the top of Fig. 6.21, do not fall exactly on the straight lines but are scattered about them. This effect is corrected for in Figs. 6.22, 6.25, 6.28, 6.31 and 6.33 by shifting each curve vertically up or down a small amount so that the predicted curves coincide at 4.2 K with the measured values. The effect of the shift is to slightly change the K' value of each complex. The average value of all the new K' values, however, still remains at 17.306(10^{-4} cm^{-1}). From the plots of Figs. 6.22 to 6.39 it is possible to read off the predicted room temperature values of A and B for all the magnetic complexes, and these are plotted at the bottom of Fig. 6.21. It is observed that the positions and slopes of the best fit lines at room temperature are nearly the same as at 4.2 K. Hence the effect of temperature is essentially to slide the points along the [redacted]

In Fig. 6.40 a plot is made of A_S vs B_S at 4.2 K so as to obtain a comparison with McGarvey's theory. It is seen in the figure that the points for the positive D salts plus NH_4 and K alums fall on one straight line, those for the negative D salts fall on another, while McGarvey's realtion $A_S = -2B_S$ falls between them. The effect of temperature is simply to slide the points along the respective lines.

In order to check the validity of the predicted room temperature values of A and B, the $^{53}Cr^{3+}$ hyperfine line spacings were measured using ordinary ESR on crystals which gave good hyperfine line resolution at room temperature. These measured values were listed in Table 5.19.

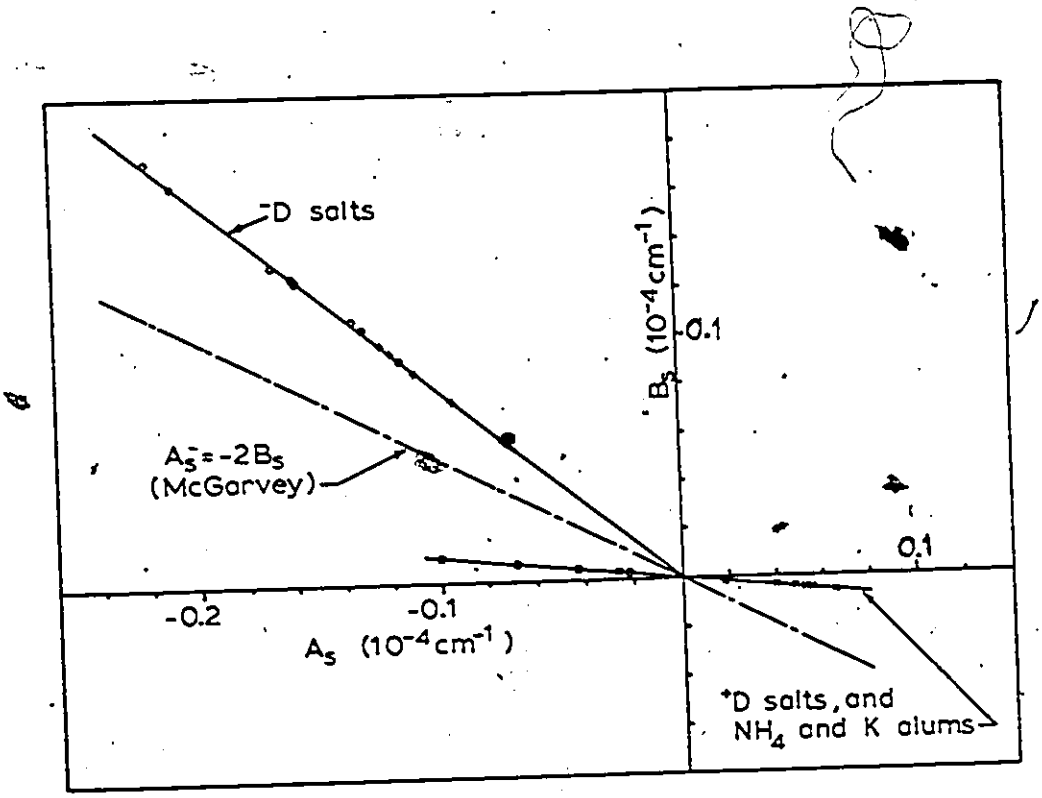

Fig. 6.40 Plots of B_S vs A_S for the Positive D Salts and for the Negative D Salts.

They are presented again in Table 6.3 along with the values predicted in this analysis. As seen in Table 6.3, the experimental measurements are in agreement with the predicted values to the accuracy of measurement, but the accuracy is not high. What the experimental measurements do is to confirm that the temperature dependence of A and B is small as predicted. Of more importance is whether or not the A and B curves increase or decrease with temperature, and the relationship of this effect to the covalent bonding existing in the $Cr^{3+}.6H_2O$ complexes. This aspect is discussed in Chapter 7.

6.6 Evaluation of the Quadrupole Moment of $^{53}Cr^{3+}$

It is possible to calculate an approximate value for the quadrupole moment of ^{53}Cr which is consistent with the theory, the ENDOR measurements, and the method of analysis described above. Since the theory given by Eqs. 3.13 and 3.14 is based on contributions due to a purely static crystalline electric field an approximate value of the quadrupole moment can be obtained by using the average value of $k_S = -0.24(10^{-3})$ obtained from Fig. 6.4 and substituting it into Eq. 3.14. In the calculation the values of $\lambda = 87\ cm^{-1}$, $\langle r^2 \rangle = 1.447$ a.u. [where 1 a.u. = 5.29172 $(10^{-9}$ cm)], $\Delta E = 17{,}600\ cm^{-1}$, and $1 - \gamma_\infty = 12$ for Cr^{3+}, were used. The calculation gives a value of $eQ = -0.034b$ for ^{53}Cr. This result can be compared to those obtained by others. Terhune et al[54] obtained a value of -0.03b in their ENDOR work of ruby, Rubinstein et al[55] obtained a value $|0.022|b$ in the magnetic resonance study of Cr_2O_3, and in the theoretical analysis

TABLE 6.3 $^{53}Cr^{3+}$ A and B Hyperfine Parameters at Room Temperature (297 K) (Unit is 10^{-4} cm^{-1}. Error of Measured Values is ±0.20 (10^{-4} cm^{-1})).

COMPLEX	A		B	
	Measured	Predicted	Measured	Predicted
GAℓSeH(1)	17.15	17.12	17.60	17.42
GAℓSeH(2)	17.24	17.14	17.49	17.48
CsAℓ(Se) alum	17.58	17.42	17.44	17.31
CsGa(Se) alum	17.60	17.42	17.45	17.29
CsAℓ(S) alum	17.15	17.20	17.50	17.46
$AℓCℓ_3.6H_2O$	17.32	17.30	17.52	17.51

of transition metal sesquioxides Artman[56] calculated a value of $|0.026b|$ and concluded further that the actual value should lie within the range 0.02 to 0.05b. While all the calculations must be regarded as approximate, the main uncertainty in our calculation lies in the value of the constant in front of Eq. 3.14. It has already been said in this work that the constant is expected to be different for the various magnetic complexes.

6.7 Evaluation of the Nuclear Magnetic Moment of ^{53}Cr

The effective nuclear g value, g'_N, of $^{53}Cr^{3+}$ was found to be isotropic in all the crystals for which ENDOR measurements were done, and these are listed in Table 5.18. Since the values listed are nearly the same, the average value $\overline{g'_N}$ is used in the following calculation. In Geshwind's phenomenological theory discussed in Chapter 3, the true nuclear g value, g_N, is related to g'_N as $g_N = g'_N/(1+\sigma)$, where σ is the shielding parameter. An approximate value of σ can be calculated from Eq. 3.15 using $\lambda = 87\ cm^{-1}$, $\langle r^{-3} \rangle = 3.959$ a.u., and $\Delta g = -0.024$, giving $\sigma = 0.00667$. Hence we find $g_N = -0.3145$. Since the nuclear magnetic moment is given by $\mu_N = g_N I$, where I is the nuclear spin, then we have $\mu_N = -0.4718\ \mu_n$. This is close to the handbook value of $-0.4744\mu_n$ obtained from NMR studies of $^{53}Cr^{3+}$ in solution.

CHAPTER 7

DISCUSSION AND CONCLUSIONS

7.1 The D vs T Curves

The varied behavior of the Cr^{3+} D vs T curves in the hydrated crystals is recognized as being of fundamental importance in obtaining a description of the physical behavior of the crystals. The philosophy behind the investigation was to obtain resonance data for many similar types of magnetic complexes, and then to see what laws of behavior the plotted results give. In this respect, an ESR and ENDOR study was made of trigonally distorted $Cr^{3+}.6H_2O$ magnetic complexes. Such chromium magnetic complexes are essentially unique in nature because a large number of them exist, and they possess a wide range of physical behaviors. That is to say, they exist with large and small trigonal distortions, with both positive and negative signs, and also some of their members undergo phase transitions at either high or low temperatures. Also of importance is the fact that enough theoretical and experimental work has been done previously by others on various aspects of the crystals or the chromium ion, that it is possible for our work to progress through stages and many of the results to be checked. The main achievement of the work was to present an empirical model for splitting the chromium spin Hamiltonian parameters into their constituent parts due to crystal vibrational and static distortion effects. While others have attempted such a separation they have run into difficulties because they considered only a few systems and were unable to "normalize" the two types of contributions. The use of many similar magnetic complexes enabled us to separate the spin

Hamiltonian parameters into two parts in a manner which was consistent for the wide range of behaviors exhibited by the magnetic complexes. This feature constitutes a normalization procedure because once the starting conditions are written down, then only one correct separation exists which will account for the plotted resonance data. The D_S vs T and D_V vs T curves shown in Chapter 6 represent the unique splitting which was achieved for the D vs T curves. The analysis produces features of crystal behavior not known before, and it gives a new way of "looking" at the crystals.

The physical behavior of the crystals, which lead to grouping of the D vs T curves into families, also shows up in other ways. Holden et al[21] measured the spontaneous polarization P_S in the guanidinium salts up to 363 K. They found that the P_S vs T curves fall into two groups depending on if S or Se is in the crystals, and that the polarizations increase with decreasing temperature. The selenates were found to have a larger value of P_S at all temperatures than did the sulfates. Hence the P_S vs T and D vs T curves follow similar trends. When Holden et al extrapolated their P_S curves to high temperatures they predicted an upper limit of about 575 K for the ferroelectric Curie temperature of the guanidinium sulfates. They state further that the selenates have either higher Curie temperatures or that their polarizations are higher up with Curie points comparable to the sulfates. It was noted during the present work that the existence of phase transitions in certain alums and the guanidinium salts was accompanied by the feature of the extended straight-line parts of the Cr^{3+} D vs T curves passing through zero. In the guanidinium salts this happens at high temperature, but as observed in

Fig. 6.1 the actual crossing points of the extended D vs T occur at much higher temperatures than estimated by Holden et al. The separated static D_S vs T curves of Figs. 6.8 and 6.9, however, do pass through the desired region. These results suggest that the phase transitions occur when the static trigonal distortion of the $Cr^{3+}.6H_2O$ complexes change sign. Since chromium is only a small dopant in these crystals then it is concluded that the phase transitions most likely occur when the trigonal distortion of the $Al^{3+}.6H_2O$ or $Ga^{3+}.6H_2O$ complexes change sign. The temperatures of such sign changes are expected to be fairly close together for the various types of complexes. This situation is more clearly shown in the case of NH_4 and K alums where D vs T curves exist for the concentrated chromic alums. Actually, concentrated chromic guanidinium crystals were grown in order to check this point but the ESR spectrum was not resolved. The behavior of the non-paramagnetic complexes such as $Al^{3+}.6H_2O$ can best be studied by measuring the temperature dependence of the Al^{3+} quadrupole interaction parameter Q' using ordinary NMR or pure quadrupole resonance. Such data has been obtained by others for NH_4 and K aluminum alums. Since the phase transition temperatures in these alums are also known, then the quadrupole data can be considered within the framework of the present analysis, and this is done below.

The Cs sulfate alums, guanidinium salts, and $AlCl_3.6H_2O$ have the common feature that their D values are negative. This is regarded as being due to a trigonal compression of the octahedron of waters surrounding the Cr^{3+} ion.[45] A positive D value as found in the Rb and Tl sulfate alums, and Cs selenate alums, represents a trigonal extension of the octahedron. The existence of high temperature crossing points in the

original D vs T curves shows up in the separated picture as crossing points in the static curves. These temperatures are 280 K in both the guanidinium sulfates and selenates, and 310 K in the Cs and Rb sulfate alums. In the D vs T curves of the Cs sulfate alums it was shown that the curve for CsIn alum did not share in the high temperature crossing point of the other Cs alums. This behavior can now be attributed to vibrational effects because, as shown in Fig. 6.10, the static curve for CsIn alum does share in the crossing point of the other Cs sulfate alums. In the room temperature X-ray crystallography of the guanidinium salts[16] it is seen that complex (2), which has the smaller D value, has in fact a slightly greater static distortion than does complex (1). It is seen in Figs. 6.8 and 6.9 that the static curves at room temperature (297 K) do indeed predict a slightly greater distortion for complex (2) in these salts. It would be interesting to perform X-ray studies at temperatures near 280 K to see if the two types of complexes in the guanidinium salts do in fact have the same percentage distortion from octahedral symmetry as predicted in this analysis.

Since a negative D_S is associated with a trigonally compressed water octahedron, this means that in the guanidinium crystals (Figs. 6.8 and 6.9) the water octahedra are under compression and the compression increases sharply with decreasing temperature. This is in agreement with what is expected when the anisotropic thermal expansion coefficients of Table 2.1 are considered, and if the water octahedra expand in a way similar to that of the unit cell. It is noted in Table 2.1 that the thermal

expansion coefficients are six to nine times larger along the crystal c axis (i.e. the trigonal direction of the water octahedra) than perpendicular to it. A picture can also be given for the relative magnitudes of distortion in the sulfate and selenate guanidinium salts. The sulfate and selenate ions form an octagonal ring around the water octahedra. Since the selenium ion is larger than sulfur, the selenium ring will be larger, with more room available for the water molecules to compress into. Hence a larger distortion, i.e. D_S, will exist in the selenates. The temperature dependence of D_S in the alums show a varied behavior. In the sulfate alums of Figs. 6.10 and 6.11 the water octahedra coordinated to the chromium ion show smaller distortions with decreasing temperature. The opposite is true for the Cs selenates of Fig. 6.12. The temperature dependence of D_S in the Cs sulfates and selenates is always small.

In spite of the varied behavior of the D_S curves in the alums, the D_V curves have a positive sign in all cases. This means that the alums all act the same insofar as their vibrational behavior is concerned. In the guanidinium salts D_V is always negative. The shape of the vibrational curve D_V as a function of temperature was taken to be that of a single hyperbolic cotangent. This functional behavior was suggested by the experimental and theoretical results of others as discussed in Chapter 1. The possible crystal vibrational mechanisms implied by the hyperbolic cotangent are as follows: (i) The vibrational mechanism in the crystal is due, as far as the D_V parameter is concerned, to the Einstein model of a crystal. In this case $\theta = h\nu/k$ gives the acting vibration,

with θ = 512 K and ν = 10.67 THz for the crystals studied. (ii) A localized resonant mode is principally responsible for the vibration of the $Cr^{3+}.6H_2O$ complex. Here again, $\theta = h\nu/k$ with ν being the frequency of the resonant mode. These kinds of resonant modes are known to exist around impurities in a crystal, and it could well apply to Cr^{3+} in the present studies. Actually the situation may be even more general in that the localized mode effect might be important even for the diamagnetic complexes such as $Al^{3+}.6H_2O$. The vibrational behavior of the trivalent ion as a function of temperature implied by the hyperbolic cotangent is that of a constant frequency but variable amplitude. Hence the vibrational energy will change with temperature because of the variable amplitude. (iii) There are many vibrational modes of different amplitudes and frequencies acting at the Cr^{3+} ion, and the distribution is such that the sum is nearly equal to a single hyperbolic cotangent. This type of situation is implied when more than one frequency of vibration is considered, e.g., in the work of Walsh[7,8] and Shrivastava.[13]

The existence of characteristic crossing points of the static lines, termed D_{SC} in Fig. 6.14, is an interesting feature and it represents a new result found in this work. The obtaining of this result is due to the fact that many crystals with the same type of magnetic complex were studied. While the result may be due to the method of analysis used, it might also be independently true and to represent a hitherto unknown order that exists in the crystals. The meaning of a given D_{SC} value is that the $Cr^{3+}.6H_2O$ complexes in the crystals have an identical value of

electric field gradient V_{zz} at the common crossing point. Moreover, as suggested by an example described below, it appears that the electric field gradient is the same at both the Cr^{3+} site and the diamagnetic trivalent ion site. For a given crystal it is logical that V_{zz} would be the same for the two types of sites at some temperature. It is not so obvious that it would be the same for different crystals, even though they are related as a family. If the electric field gradient at the trivalent ion site is due directly or indirectly to the coordinated octahedron of waters, then Fig. 6.14 suggests that certain octahedral shapes have special significance in the crystals. What the significance might be can only be speculated at the present time.

7.2 Phase Transitions in NH_4 and K Alums

The principal feature of the splitted D vs T curves for NH_4 and K alums (Figs. 6.17 and 6.18) is the fact that the static curves for NH_4Cr and KCr alums pass through zero D at 82 and 162 K, respectively. These temperatures are nearly identical to the values of 81 and 160 K reported by Bleaney[30] for the phase transitions in the chromic alums. Since all the trivalent ions in NH_4Cr and KCr alums are Cr^{3+}, it is concluded that these alums undergo phase transitions when the static distortion at the chromium sites change sign. If the strength and symmetry of the crystalline electric field at the chromium sites are due to the octahedron of waters surrounding the Cr^{3+} ions, then it can be said that the phase transitions occur when the trigonally distorted

octahedra change from extension to compression.

The Cr^{3+} dopant level in the Ga and Al isomorphs of the NH_4 and K alums are estimated to be about 1 Cr^{3+} ion per 100 Al or Ga. As shown in Figs. 6.17 and 6.18, the static curves obtained in the isomorphs pass through zero D at temperatures higher than in the chromic alums, and also higher than the known phase transition temperatures occurring in the crystals. For example, the phase transition temperature in NH_4Al alum is reported to be 71 K[32], while for KAl alum it is at 98 K.[33] Hence it is concluded that in the lightly doped crystals, the octahedron of waters surrounding the chromium ion can change from a trigonal extension to compression without affecting the crystal. This effect is established in the case of NH_4Al alum where it was seen that the D vs T curve passed through zero D (Fig. 6.15) at a temperature above the lowest measured point obtained at 77 K, without affecting the trigonal nature of the site. Figure 6.17 shows that the static curve of NH_4Al alum changes sign at 124 K. In view of these results it seems likely that the phase transitions in the lightly doped NH_4 and K alums are due to the octahedron of waters surrounding the Ga and Al ions changing from trigonal extension to compression. The changes occur at temperatures lower than in the chromic alums. This behavior puts the lightly doped or even undoped crystals on the same footing as the chromic alums, which is justified since the behavior of the crystals are closely related as indicated in Figs. 6.15 and 6.16. Below the phase transition temperature, the Cr^{3+} magnetic complexes change to rhombic symmetry, giving rise to 12 magnetic

complexes with the z axes making large angles with the crystal [111] directions. A chromium ESR spectrum obtained along a crystal [111] direction in the dilutely doped crystals shows the resonance lines to be scattered over the whole range between the highest and lowest lines.

NH_4In alum lightly doped with Cr^{3+} represents a special case in which the crystal undergoes a phase transition at 127 K[32], but the chromium static curve never passes through zero. If the phase transition in NH_4In alum is due to a change in sign of the trigonally distorted octahedron of waters surrounding the In^{3+} ion, then this effect has a relatively minor effect on the chromium sites when the latter do not change sign. The chromium ESR spectrum along a crystal [111] direction has the same overall appearance below the transition temperature as above, except that each fine structure spectral line appears as a group of three closely spaced lines. The chromium spectra below the transition temperature consist of 12 complexes with rhombic symmetry, but the z magnetic axes make small angles with the crystal [111] directions.

A similar type of effect was found to occur for Cr^{3+} doped in methylammonium alum,[32,57] but in this case the phase transition is said to be due to a 180° flip motion of the $CH_3NH_3^+$ ion. The D vs T curve in methylammonium alum does not pass through zero. D when the straight-line part between 195 and 297 K is extended linearly back to 0 K. This fact can be attributed to the different nature of the phase transition as compared to the NH_4 and K alums.

The described splitting of the D vs T curves in the NH_4 and K alums produced patterns of vibrational curves similar to that obtained in the Rb, Cs and Tl alums described above. That is, D_V is positive in all cases.

7.3 Analysis of the Q' vs T Curves for Al^{3+} in NH_4 and K Alums

The purpose of this section is to apply the theory and results of the splitting procedure developed in this thesis to an independent set of measurements obtained by others, in order to show the general validity of the method. The subject considered is the $^{27}Al^{3+}$ nuclear quadrupole interaction curves, Q' vs T, obtained by Burns[33] in undoped NH_4 and K sulfate alums using the technique of NMR. The points measured by Burns are shown as circles in Fig. 7.1. Before considering Burns' results it is desirable to obtain the quadrupole interaction curves predicted by the present theory for $^{53}Cr^{3+}$ impurities in the NH_4 and K aluminum sulfate alums. The chromium Q' values are given by $Q' = k_S D_S + k_V D_V$ with $k_S = -k_V$, and $k_S = -0.215(10^{-3})$ for the alums. The Cr^{3+} temperature dependence of D_S and D_V, as found above for all the hydrated crystals, is tabulated in Appendix A. Using the values for NH_4 and K alums, the static and vibrational contributions to the $^{53}Cr^{3+}$ Q' value (namely $Q'_S = k_S D_S$ and

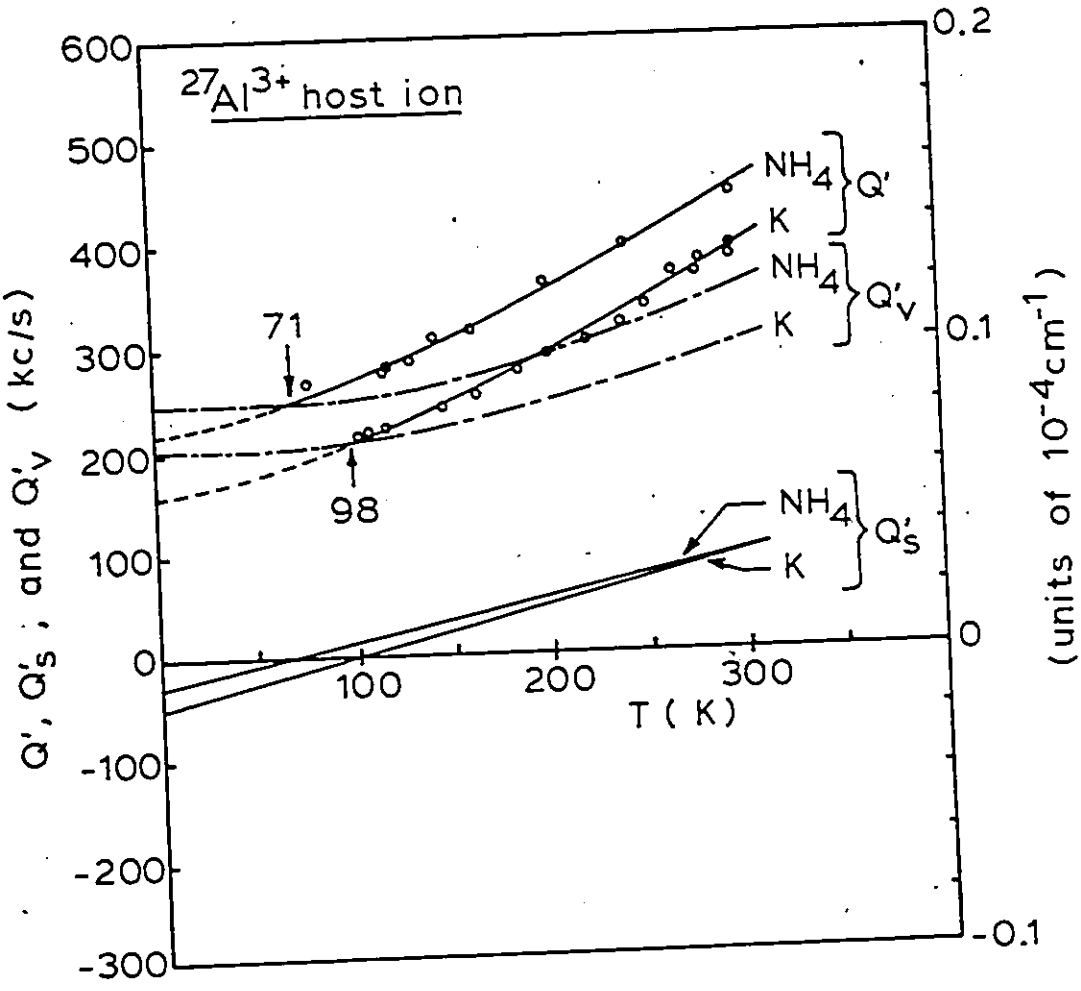

Fig. 7.1 Temperature Dependence of Q', Q'_S and Q'_V for $^{27}Al^{3+}$ in NH_4Al and KAl Alums: The Q' Points are Obtained by Burns from NMR.

$Q'_V = k_V D_V$) are calculated, and the results are plotted in Fig. 7.2. It is observed in this figure that the static curves are nearly straight lines, and that they intersect at 310 K. The low temperature parts of the Q'_S curves represent the predicted behavior if the $^{53}Cr^{3+}.6H_2O$ magnetic complexes were not affected by any phase transitions occuring in the crystals. The static curves cross at 310 K because they follow the behavior of the D_S curves. At 310 K it is observed that $Q'_S = -0.085$ $(10^{-4}cm^{-1})$, and $\Delta Q'_V = 0.018$ $(10^{-4}cm^{-1})$ where $\Delta Q'_V$ is the difference between the Q'_V values of the two salts.

The experimental results of Burns shown in Fig. 7.1 are now considered. The phase transition in NH_4Al alum is known to occur at 71 K[32] and in KAl alum at 98 K[33]. In the analysis procedure, curves are drawn through Burns' Q' values and they are extended continuously to 0 K. The parts below the phase transitions represent the expected behavior of the Q' curves if they were not affected by any phase transitions occuring in the crystals. It was postulated in Chapter 6 that phase transitions occur in the undoped or dilutely doped NH_4 and K aluminum alums when the static trigonal distortion at the Al^{3+} sites changes sign. This means that the Q'_S curves must pass through zero at 71 and 98 K in the NH_4 and K alums, respectively. It is in turn necessary for the Q'_V curves describing the vibrational behavior of the $Al^{3+}.6H_2O$ complex to cross the total Q' curves at the transition temperatures. In this way the relation $Q' = Q'_S + Q'_V$ will be satisfied at the transition temperatures. The vibrational behavior of the aluminum complexes, on the basis of our theory, is described by the function $Q'_V = Q^o_V \coth(\theta/2T)$, with $\theta = 512$ K for the alums, and Q^o_V is the

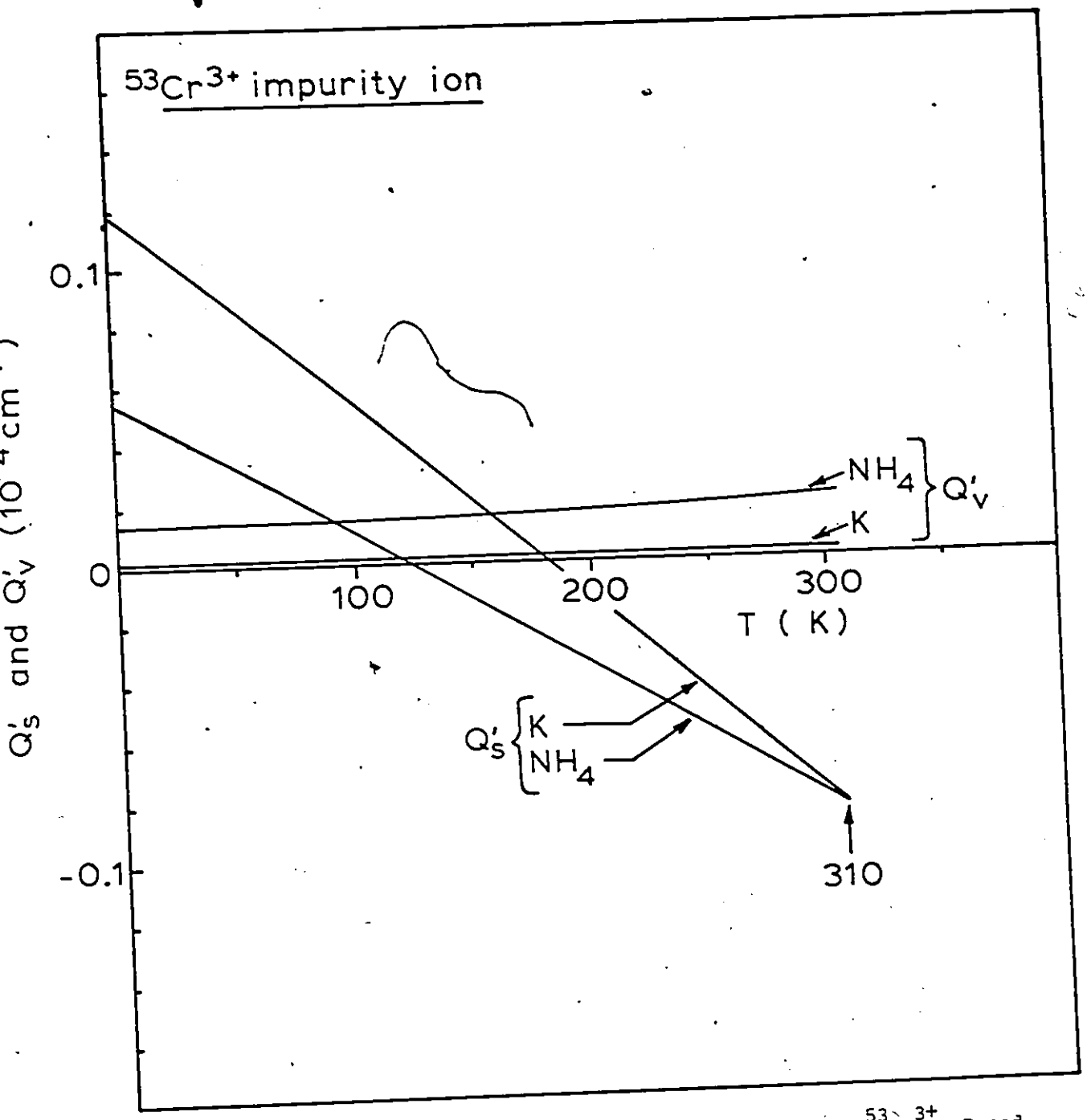

Fig. 7.2 Temperature Dependence of Q', Q'_s and Q'_v for $^{53}Cr^{3+}$ Doped in NH_4Al and KAl Alums.

value of Q'_V at 0 K. The Q'_V curves are drawn in Fig. 7.1. The static behavior of the aluminum complexes in the two types of alums is taken to be the same as that of the chromium impurity complexes, which are straight lines. Once the Q'_V lines are drawn in Fig. 7.1 then there is only a single choice on how to place the static Q'_S lines. For example, in the case of NH_4 alum, one point on the static line is at 71 K with zero Q'_S while the other is at 0 K at a distance below zero as the Q' line is below the Q'_V line. A straight line representing Q'_S is then drawn through the two points. The same procedure is followed for the case of K alum. It is observed that the two Q'_S lines intersect near 310 K. It is observed in Fig. 7.1 that the sum of the static and vibrational curves produces the original curves, and the relation $Q' = Q'_S + Q'_V$ is satisfied at all temperatures.

It is observed in Fig. 7.1 that the spacing between the measured Q' curves becomes smaller with increasing temperature, while that of the vibration curves becomes greater. The convergence of the Q' curves is accounted for by the greater slope of the potassium Q'_S line. The graphical solution in Fig. 7.1 is a unique solution from two points of view: If the transition temperature (71 or 98 K) of either crystal differed by more than 2 or 3 degrees, then the relation $Q' = Q'_S + Q'_V$ could not be satisfied as a function of temperature after repositioning of the Q'_S line and recalculating and positioning of the new Q'_V curve. The additive relationship would also not hold if the amount of separation between the two Q' curves was different than that shown in Fig. 7.1.

At 310 K it is observed in Fig. 7.1 that $Q_S' \doteq 0.033$ $(10^{-4} cm^{-1})$ and $\Delta Q_V' = 0.018$ $(10^{-4} cm^{-1})$, where $\Delta Q_V'$ is the difference between the Q_V' values of the two salts. This value of $\Delta Q_V'$ is the same as found above for the chromium complexes in the two salts. The following formula has been given to describe the nuclear quadrupole interaction of a trivalent ion with nuclear spin I interacting with the surrounding ligand atoms in the static theory[46].

$$Q_S' = \frac{3V_{zz}eQ}{4I(2I-1)} \cdot (1 - \gamma_\infty)$$

In this formula, V_{zz} is the electric field gradient due to charges and dipoles external to the trivalent ion, eQ is the quadrupole moment of the central ion, and $1 - \gamma_\infty$ is the Sternheimer antishielding factor. Sternheimer[58] has calculated $1 - \gamma_\infty$ to be equal to 12 for Cr^{3+} and 3.36 for Al^{3+}. The quadrupole moment for ^{27}Al is 0.149 b and for ^{53}Cr a value of - 0.034b was found above. Since $I = 5/2$ for ^{27}Al and $I = 3/2$ for ^{53}Cr, then the following ratio is found

$$(Q_S')_{Cr}/(Q_S')_{Al} = -0.102\ (V_{zz})_{Cr}/\ 0.372\ (V_{zz})_{Al}. \qquad (7.1)$$

In the discussion on static crossing points given above, it was speculated that at 310 K in the alums, the trivalent ions in all the crystals associated with a given D_{SC} point have the same value of electric field

gradient V_{ZZ}. Since the NH_4 and K aluminum alums have a common value of D_{SC}, and we put $[(V_{ZZ})_{Cr}/(V_{ZZ})_{Al}]_{310\ K} = 1$, Eq. 7.1 gives $(Q_S')_{Cr} = -2.7(Q_S')_{Al}$ at 310 K. The ratio obtained at 310 K from the graphs of Figs. 7.1 and 7.2 is $(Q_S')_{Cr} = (-2.6\pm0.2)(Q_S')_{Al}$, which is the same as the calculated value.

These results show that the model of parameter splitting developed in the thesis will account for the Q' vs T curves measured by Burns. The postulates, assumptions and results of the model all contribute to the obtaining of a quantitative fit. The analysis gives one insight into the behavior of the measured $^{27}Al^{3+}$ Q' curves of Fig. 7.1. For example, if the Q' curves in the two alums were placed higher up in the figure then it is expected they would diverge with increasing temperature because they would be controlled mostly by the Q_V' curves which diverge by a greater amount for higher positions in the figure. Conversely, if the Q' curves were placed lower in the figure, then it is expected that they would converge more sharply because they would be controlled mostly by the Q_S' curves. In both these cases it would be necessary, of course, for the transition temperatures to occur at values different than 71 and 98 K, otherwise the condition $Q' = Q_S' + Q_V'$ would not be satisfied.

7.4 The Hyperfine Parameters A and B

The plotted experimental values of A vs D at 4.2 K shown at the top of Fig. 6.21 can be described in terms of the distortion of the octahedron of waters coordinated to the chromium ion as follows: For a negative D value, an increase in the trigonal compression of the octahedron causes an increase in the magnitude of D. Because of the increased compression, more of the chromium electrons will be transferred to the oxygens of the water ligands in the [111] direction. This will cause a decrease in the magnitude of the hyperfine interaction energy, with a consequent decrease in A. For a positive D value, an increase in the trigonal extension of the octahedron also causes an increase in the magnitude of D. Because of the increased extension, less of the chromium electrons will be transferred to the oxygen ligands in the [111] direction. This will cause an increase in the magnitude of the hyperfine interaction energy, with a consequent increase in A.

In the temperature dependence of the A parameter, it is seen in Figs. 6.22, 6.25, 6.28, 6.31 and 6.33 that an increase in A with temperature is accompanied by a decrease in B, and vice versa. But the variation in B is usually not as great as that for A, especially for the complexes with positive D. Hence an increase or decrease in transferred chromium electrons in a [111] octahedral direction is accompanied by a decrease or increase, respectively, of electrons in the perpendicular direction.

The experimental graph at the top of Fig. 6.21 shows an interesting property. When the best fit lines through the B values are extended linearly to the y axis at zero D, it is seen that for positive D the line cuts the y axis near the value of K', while for negative D it is higher. In the first case the condition A = B is satisfied at zero D, while in the second it is not. The condition A = B = K' at zero D is accounted for in McGarvey's theory (Eqs. 6.9 and 6.10) by the requirement that $A_S = B_S = 0$. The condition B>A at zero D is untenable in McGarvey's theory. In the present analysis it is seen that the condition $A \doteq B \doteq K'$ is satisfied for the positive D branch at zero D due to the fact that $A_S \doteq -A_V$ and B_S and B_V are relatively small. This effect can be seen for the case of NH_4Ga alum in Figs. 6.36 and 6.39. When the negative D branch of B is extended to zero D, the condition $A_S \doteq -A_V$ still holds but B_S and B_V are now big enough to give an additional contribution to B. It is also noted in Fig. 6.39 that B_S and B_V are very small for the B branch with positive D.

In conclusion, the main features of this work are recapitulated: The predicted value of the ^{53}Cr nuclear quadrupole moment was found to be - 0.034b, which is in agreement within the range of values found by others. A larger static distortion is predicted at room temperature in the guanidinium salts for the complexes termed (2) than in those termed (1), which is in agreement with X-ray structure measurements. The nature of the phase transitions in the NH_4 and K alums were accounted for in a quantitative manner. The method of analysis was applied to an independent set of measurements obtained by others, and was found to

produce a unique graphical solution to the results. Other features such as the existence of characteristic static crossing points should be studied further, and the general applicability of the analysis method should be tried on other crystal or ion systems.

APPENDIX A

List of the values of the static vibrational and total zero-field splitting parameters D_S, D_V and D at different temperatures for the crystals studied in this work. The unit of D_S, D_V and D is $10^{-4}cm^{-1}$ and the temperature is in degree K. The computer program used, to obtain the values, is also given.

```
$JOB  ACCT-VUN,LECLERC,TIME=30,PAGES=28,LINES=66
      DIMENSION TEXT (6)
      N=24
      AS=1.
      AV=1.
      DO 7 I=1,N
      READ (5,1)(TEXT (J),J=1,6)
      READ (5,2) ALPHA,BETA,TETA,DS,DV
      WRITE (6,5)(TEXT (J),J=1,6)
      WRITE (6,6)
    9 FORMAT (6A4)
   10 1 FORMAT (2E12.5,F5.1, 2F8.1)
   11 5 FORMAT ('1',6A4)
   12 6 FORMAT (' ',13X,'STATIC D',21X,'VIBRATIONALI D',20X,'TOTAL D',24X,
     1'TEMPERATJRE')
      DO 7 I=20,420,20
      J=I-20
      XAS=AS*DS*(1.+ALPHA*FLOAT(J)+BETA*FLOAT(J)*FLOAT(J))
      IF (J.EQ.0) GO TO 3
      XAV=AV*DV/TANH(TETA/(2.*FLOAT(J)))
      GO TO 4
    3 XAV=AV*DV
    4 A=XAS+XAV
    7 WRITE (6,8) XAS,XAV,A,J
    8 FORMAT (' ',12X,F8.1,22X,F8.1,20X,F8.1,29X,I3)
      RETURN
      END
```

$ENTRY

R3ALI SULFATE ALJH STATIC D	VIBRATIONALI D	TOTAL D	TEMPERATJRE
225.0	124.0	349.0	0
221.0	124.0	345.0	20
220.4	124.0	344.4	40
223.1	124.0	347.2	60
229.1	124.5	353.5	80
238.5	125.5	364.0	100
251.2	127.5	378.7	120
267.2	130.5	397.7	140
286.6	134.4	421.0	160
309.3	139.2	448.4	180
335.3	144.6	479.9	200
364.6	150.6	515.2	220
397.3	157.1	554.4	240
433.3	164.0	597.3	260
472.7	171.2	643.8	280
515.4	178.6	694.0	300
561.4	186.4	747.7	320
610.7	194.3	805.0	340
663.4	202.4	865.8	360
719.4	210.6	930.0	380
778.7	219.0	997.7	400

R3GH SULFATE ALJH STATIC D	VIBRATIONALI D	TOTAL D	TEMPERATJRE
299.9	213.1	518.0	0
300.0	218.1	518.1	20
302.1	218.1	520.2	40
306.3	213.2	524.5	60
312.6	218.8	531.4	80
320.9	220.7	541.6	100
331.3	224.3	555.6	120
343.7	229.7	573.4	140

358.2	236.7	594.9	160
374.7	245.1	619.8	180
393.3	254.7	648.1	200
414.0	265.4	679.4	220
436.7	276.8	713.6	240
461.5	289.0	750.5	260
488.4	301.8	790.1	280
517.3	315.8	832.3	300
548.2	329.7	876.9	320
581.2	342.7	923.9	340
616.3	357.0	973.3	360
653.5	371.6	1025.0	380
692.7	385.4	1079.0	400

TLGA SULFATE ALUM

STATIC D	VIBRATIONAL D.	TOTAL D	TEMPERATURE
271.1	170.4	441.5	0
273.3	170.4	443.7	20
279.7	170.4	449.1	40
287.1	170.5	457.6	60
299.7	171.9	469.6	80
313.7	172.4	486.1	100
331.2	175.2	506.4	120
352.1	179.4	531.5	140
376.1	184.8	561.0	160
403.3	191.4	594.7	180
433.6	198.9	632.5	200
467.0	207.2	674.1	220
503.5	216.1	719.6	240
543.1	225.6	768.7	260
585.9	235.5	821.3	280
631.7	245.8	877.5	300
680.7	256.4	937.1	320
732.0	267.4	1000.2	340
786.0	278.5	1066.5	360
842.6	289.9	1136.2	380
901.8	301.4	1209.2	400

CSALI SELFVATE ALUM

STATIC D	VIBRATIONAL D	TOTAL D	TEMPERATURE
293.1	266.9	559.8	0
299.5	260.9	560.2	20
308.4	260.9	561.3	40
321.3	261.0	562.3	60
302.0	261.8	563.8	80
302.6	264.1	566.6	100
303.0	268.4	571.3	120
305.2	274.8	578.0	140
305.3	283.1	586.4	160
303.2	293.2	596.4	180
302.9	304.7	607.7	200
302.5	317.5	619.9	220
301.9	331.2	633.1	240
301.1	345.7	646.9	260
300.2	361.0	661.2	280
299.1	376.8	675.9	300
297.9	393.2	691.0	320
296.4	409.9	706.4	340
294.9	427.0	721.9	360
293.1	444.3	737.6	380
291.2	462.2	753.4	400

CSGA SELFVATE ALUM

STATIC D	VIBRATIONAL D	TOTAL D	TEMPERATURE
368.2	351.8	720.0	0
368.2	351.8	720.0	20
367.6	351.8	719.4	40
366.4	351.9	718.4	60
364.6	352.9	717.6	80
362.2	355.0	718.2	100
359.2	361.7	720.9	120
355.6	370.2	725.8	140
351.3	381.4	732.7	160
346.5	394.9	741.4	180
341.1	410.3	751.3	200
335.0	427.3	762.3	220
328.4	445.7	774.0	240
321.1	463.2	786.3	260
313.3	485.6	798.9	280
304.8	506.8	811.6	300
295.7	523.7	824.5	320
286.1	551.2	837.3	340
275.8	571.2	854.0	360
264.9	597.6	862.5	380
253.4	621.4	874.8	400

NITER SULFATE ALUM

STATIC D	VIBRATIONAL D	TOTAL D	TEMPERATURE
-127.8	206.1	78.3	0
-97.7	206.1	108.4	20
-66.9	206.1	139.2	40
-35.4	206.2	170.8	60
-3.2	206.8	203.5	80
29.6	208.6	238.2	100
63.1	212.9	275.1	120
97.3	217.0	314.3	140
132.1	223.6	355.7	160
167.7	231.6	399.2	180
203.9	240.6	444.5	200
240.8	250.7	491.4	220
278.3	261.5	539.8	240
316.6	273.0	589.5	260
355.5	285.8	640.5	280
395.1	297.5	692.6	300
435.3	314.4	745.7	320
476.3	323.6	799.9	340
517.9	337.1	855.2	360
560.2	354.9	911.1	380
603.2	364.8	968.0	400

NIACA SULFATE ALUM

STATIC D	VIBRATIONAL D	TOTAL D	TEMPERATURE
-150.6	185.3	35.3	0
-116.1	185.3	69.2	20
-81.9	185.4	103.4	40
-47.3	185.9	138.1	60
-12.3	187.5	173.6	80
23.5	191.6	210.5	100
60.6	195.1	249.2	120
99.7	201.0	289.8	140
131.0	209.2	332.1	160
167.7	216.3	375.9	180
204.8	225.4	421.2	200
242.2	235.1	467.6	220
280.0	245.4	515.1	240
318.2	256.2	563.6	260
356.6		612.9	280

395.5	267.5	662.9	320
434.7	279.1	713.7	320
474.2	290.9	765.2	340
514.1	303.1	817.2	360
554.4	315.5	869.8	380
595.0	328.0	923.0	400

NORMAL SULFATE ALUM

STATIC D	VIBRATIONAL D	TOTAL D	TEMPERATURE
-266.1	67.2	-198.9	0
-223.8	67.2	-156.6	20
-181.2	67.2	-114.0	40
-138.4	67.2	-71.2	60
-95.4	67.4	-28.0	80
-52.2	68.0	15.8	100
-8.7	69.1	60.4	120
34.9	70.8	105.7	140
78.8	72.9	151.7	160
122.9	75.5	198.4	180
167.2	78.5	245.7	200
211.8	81.7	293.5	220
256.5	85.3	341.8	240
301.5	89.0	390.5	260
346.7	92.9	439.6	280
392.1	97.0	489.1	300
437.7	101.2	538.9	320
483.6	105.5	589.1	340
529.6	109.9	639.6	360
575.9	114.4	690.3	380
622.4	119.0	741.4	400

MAIN SULFATE ALUM

STATIC D	VIBRATIONALI D	TOTAL D	TEMPERATURE
96.1	196.9	293.0	0
93.7	196.9	290.6	20
90.4	196.9	291.3	40
90.3	197.0	295.3	60
105.4	197.6	303.0	80
115.7	199.5	315.0	100
129.1	202.5	331.6	120
145.7	207.3	353.1	140
165.5	213.6	379.2	160
188.5	221.2	409.7	180
214.6	229.9	444.5	200
243.9	239.5	483.4	220
276.3	249.8	526.2	240
311.8	260.8	572.8	260
350.3	272.4	623.1	280
392.0	284.2	677.0	300
437.9	296.5	734.4	320
486.2	309.2	795.4	340
537.7	322.1	859.8	360
592.4	335.2	927.6	380
650.2	348.6	998.8	400

KCRI SULFATE ALUM

STATIC D	VIBRATIONALI D	TOTAL D	TEMPERATURE
-393.2	168.0	-225.2	0
-349.1	163.0	-186.1	20
-302.9	168.0	-134.8	40
-255.6	168.1	-86.9	60
-207.5	169.6	-38.4	80
-159.2	173.0	12.8	100

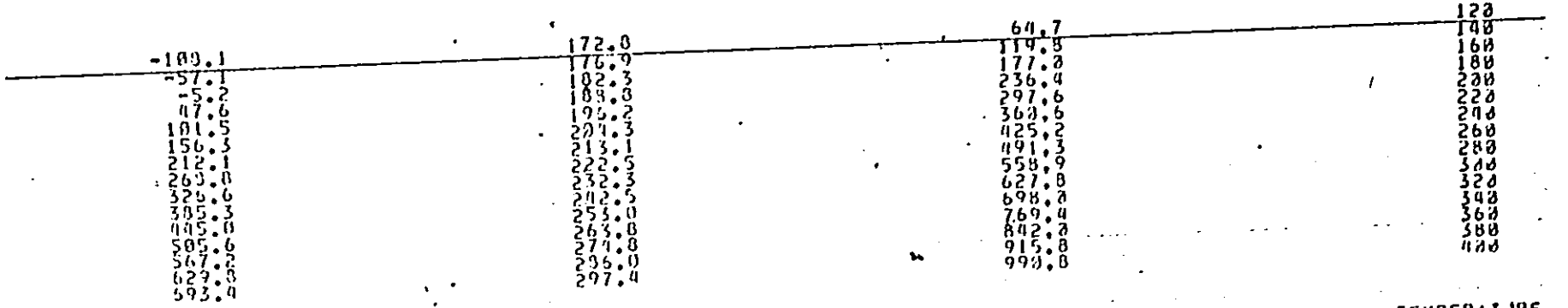

KGA SULFATE ALUM

STATIC D	VIBRATIONAL D	TOTAL D	TEMPERATURE
-410.6	151.1	-255.9	0
-365.8	154.1	-211.7	20
-320.3	154.1	-166.2	40
-273.6	154.2	-119.5	60
-225.7	154.6	-71.1	80
-176.5	153.8	-22.6	100
-126.1	153.5	32.4	120
-74.5	162.3	87.8	140
-21.5	167.2	145.7	160
32.6	173.1	205.8	180
88.6	179.9	268.5	200
144.7	187.4	332.1	220
202.7	195.5	398.1	240
261.7	204.1	465.8	260
322.1	213.1	535.2	280
383.7	222.4	606.1	300
446.6	232.1	678.6	320
510.7	242.0	752.6	340
576.0	252.1	828.1	360
642.6	262.3	904.9	380
710.4	272.8	983.2	400

KAL SULFATE ALUM

STATIC D	VIBRATIONAL D	TOTAL D	TEMPERATURE
-557.2	7.2	-550.0	0
-499.4	7.2	-492.2	20
-441.0	7.2	-433.8	40
-381.9	7.2	-374.7	60
-322.1	7.3	-314.8	80
-261.6	7.4	-254.3	100
-200.5	7.6	-193.0	120
-138.5	7.8	-130.9	140
-76.5	8.1	-68.2	160
-12.7	8.4	-4.6	180
51.2	8.8	59.6	200
115.3	9.1	124.5	220
181.1	9.5	190.2	240
247.8	10.0	256.6	260
315.7	10.4	323.7	280
381.3	10.8	391.4	300
447.1	11.3	459.9	320
517.8	11.8	529.1	340
587.2	12.3	598.9	360
657.2	12.7	669.5	380
728.0		740.7	400

CSALI SULFATE ALJH

STATIC D	VIBRATIONAL D	TOTAL D	TEMPERATURE
-714.5	0.0	-714.5	0
-716.8	0.0	-716.8	20
-719.3	0.0	-719.3	40
-721.9	0.0	-721.9	60
-724.6	0.0	-724.6	80
-727.5	0.0	-727.5	100
-730.4	0.0	-730.4	120
-733.5	0.0	-733.5	140
-736.7	0.0	-736.7	160
-740.0	0.0	-740.0	180
-743.5	0.0	-743.5	200
-747.1	0.0	-747.1	220
-750.8	0.0	-750.8	240
-754.6	0.0	-754.6	260
-758.5	0.0	-758.5	280
-762.6	0.0	-762.6	300
-766.8	0.0	-766.8	320
-771.1	0.0	-771.1	340
-775.5	0.0	-775.5	360
-780.0	0.0	-780.0	380
-784.7	0.0	-784.7	400

CSGR SULFATE ALJH

STATIC D	VIBRATIONAL D	TOTAL D	TEMPERATURE
-685.8	25.4	-660.8	0
-687.6	25.4	-662.2	20
-690.2	25.4	-664.8	40
-693.2	25.5	-667.9	60
-696.5	25.7	-671.2	80
-700.2	26.1	-674.5	100
-704.3	26.8	-678.2	120
-708.8	27.6	-682.2	140
-713.6	28.6	-686.8	160
-718.8	29.7	-690.2	180
-724.3	30.9	-693.6	200
-730.3	32.3	-699.3	220
-736.6	33.7	-702.5	240
-743.2	35.2	-709.5	260
-750.3	36.7	-715.1	280
-757.7	38.3	-721.8	300
-765.5	40.0	-727.1	320
-773.6	41.6	-733.7	340
-782.1	43.3	-740.5	360
-791.0	45.1	-747.7	380
-800.3		-755.2	400

CSIN SULFATE ALJH

STATIC D	VIBRATIONAL D	TOTAL D	TEMPERATURE
-633.1	102.1	-528.0	0
-633.1	102.1	-531.0	20
-636.0	102.1	-534.7	40
-641.3	102.4	-539.2	60
-646.6	103.3	-544.2	80
-652.7	105.0	-549.3	100
-659.4	107.5	-554.4	120
-667.0	110.8	-559.4	140
-675.3	114.8	-564.5	160
-684.4	119.3	-569.6	180
-694.2	124.3	-574.9	200
-704.8	129.7	-580.5	220
-716.2	135.4	-586.5	240
-728.3		-592.9	260

-741.2	141.3	-599.8	280
-758.8	147.6	-607.3	300
-769.2	154.0	-615.3	320
-784.4	160.5	-623.8	340
-799.3	167.2	-633.1	360
-817.0	174.1	-642.9	380
-934.4	181.0	-653.4	400

ALCL3.6H2O

STATIC D	VIBRATIONAL D	TOTAL D	TEMPERATURE
-539.5	192.6	-346.9	0
-538.8	192.6	-345.4	20
-537.4	192.6	-344.8	40
-537.7	192.7	-345.2	60
-538.0	193.2	-345.5	80
-540.7	194.9	-345.8	100
-543.5	198.0	-345.5	120
-547.2	202.7	-344.5	140
-551.7	208.8	-343.0	160
-557.1	216.1	-341.0	180
-563.3	224.5	-338.8	200
-570.4	233.8	-336.6	220
-578.4	243.9	-334.5	240
-587.2	254.5	-332.6	260
-596.8	265.7	-331.1	280
-607.3	277.3	-330.0	300
-618.7	289.3	-329.4	320
-630.9	301.6	-329.3	340
-644.0	314.1	-329.9	360
-657.9	326.9	-331.0	380
-672.7	339.9	-332.8	400

GALBH(1)

STATIC D	VIBRATIONAL D	TOTAL D	TEMPERATURE
-914.6	-242.4	-1157.0	0
-899.3	-242.4	-1141.7	20
-881.8	-242.5	-1123.4	40
-859.0	-243.2	-1102.3	60
-835.6	-243.4	-1078.9	80
-808.5	-249.4	-1053.9	100
-778.3	-255.5	-1027.8	120
-745.3	-265.8	-1010.7	140
-709.2	-272.8	-972.5	160
-670.2	-283.6	-943.0	180
-628.2	-295.3	-911.8	200
-583.3	-308.3	-878.7	220
-535.5	-321.9	-843.7	240
-484.5	-336.2	-806.9	260
-430.6	-351.0	-766.8	280
-373.8	-366.2	-724.8	300
-314.1	-381.9	-680.3	320
-251.3	-397.9	-633.2	340
-185.6	-414.2	-583.5	360
-117.9	-430.7	-531.2	380
-45.3		-476.1	400

GALBH(2)

STATIC D	VIBRATIONAL D	TOTAL D	TEMPERATURE
-764.4	-125.6	-890.8	0
-752.8	-125.6	-878.4	20
-739.2	-125.7	-864.8	40
-723.7	-126.0	-849.4	60
-706.4		-832.4	80

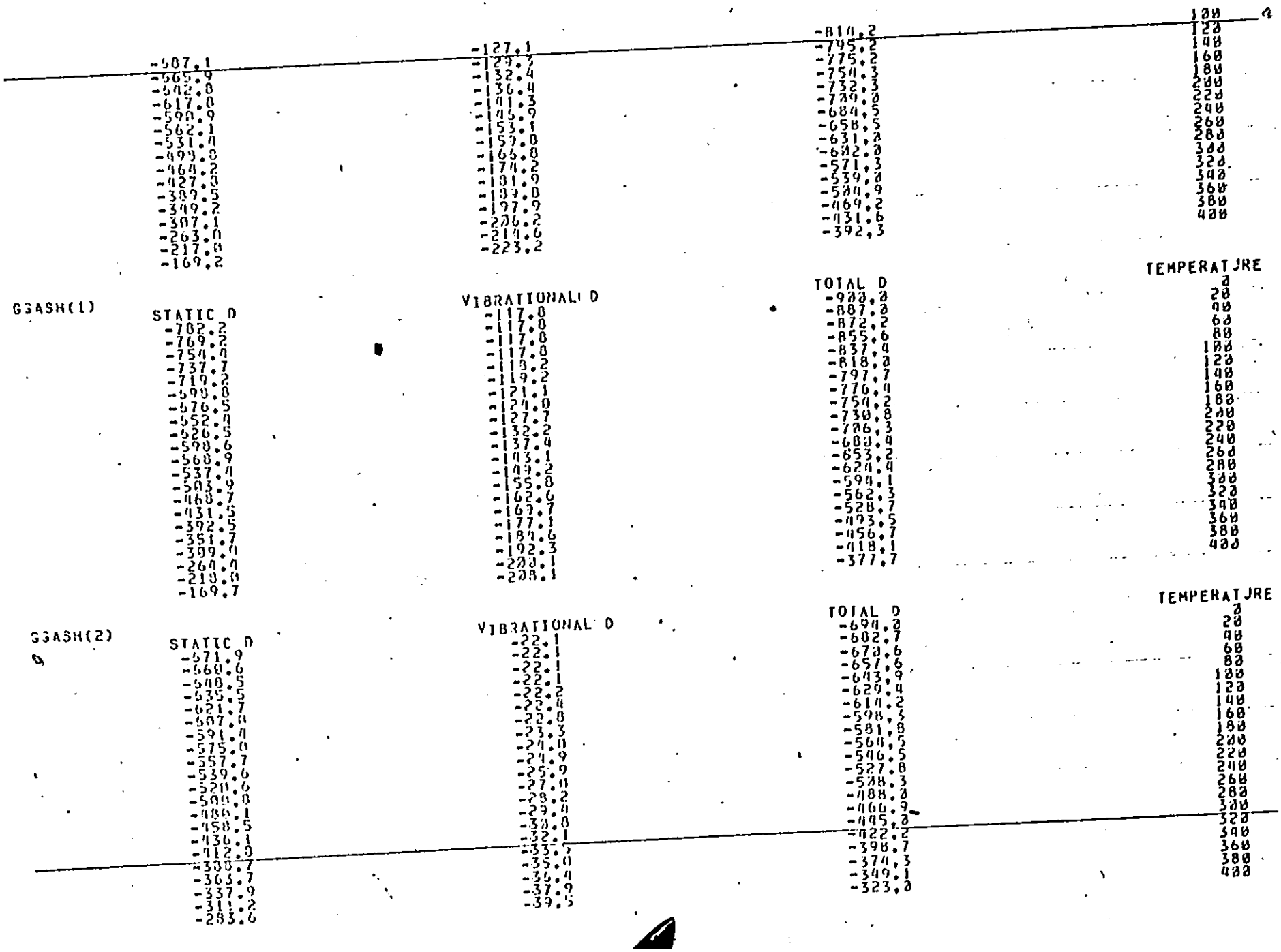
-507.1
-565.9
-542.8
-617.8
-590.9
-562.1
-531.4
-499.8
-464.2
-427.0
-389.5
-349.2
-307.1
-263.0
-217.0
-169.2
-127.1
-129.2
-132.4
-136.4
-141.3
-145.9
-153.1
-159.8
-166.8
-174.2
-181.9
-189.8
-197.9
-206.2
-214.6
-223.2
-814.2
-795.2
-775.2
-754.3
-732.3
-709.0
-684.5
-658.5
-631.0
-602.0
-571.3
-539.0
-504.9
-469.2
-431.6
-392.3
100
120
140
160
180
200
220
240
260
280
300
320
340
360
380
400
TEMPERATURE
0
20
40
60
80
100
120
140
160
180
200
220
240
260
280
300
320
340
360
380
400
GGASH(1)
STATIC D
-782.2
-769.2
-754.4
-737.7
-719.2
-698.8
-676.5
-652.5
-626.5
-598.6
-568.9
-537.4
-503.9
-468.7
-431.5
-392.5
-351.7
-309.0
-264.4
-219.0
-169.7
VIBRATIONALI D
-117.8
-117.8
-117.8
-118.2
-119.2
-121.1
-124.0
-127.7
-132.2
-137.4
-143.1
-149.2
-155.8
-162.6
-169.7
-177.1
-184.6
-192.3
-200.1
-208.1
TOTAL D
-900.0
-887.0
-872.2
-855.6
-837.4
-818.0
-797.7
-776.4
-754.2
-730.8
-706.3
-680.9
-653.2
-624.4
-594.1
-562.3
-528.7
-493.5
-456.7
-418.1
-377.7
TEMPERATURE
0
20
40
60
80
100
120
140
160
180
200
220
240
260
280
300
320
340
360
380
400
GGASH(2)
0
STATIC D
-571.9
-660.6
-648.5
-635.5
-621.7
-607.3
-591.4
-575.0
-557.7
-539.6
-520.8
-501.3
-480.1
-458.5
-436.1
-412.8
-388.7
-363.7
-337.9
-311.2
-283.6
VIBRATIONAL D
-22.1
-22.1
-22.1
-22.1
-22.2
-22.4
-22.8
-23.3
-24.0
-24.9
-25.9
-27.0
-28.2
-29.4
-30.8
-32.1
-33.5
-35.0
-36.4
-37.9
-39.5
TOTAL D
-690.0
-682.7
-670.6
-657.6
-643.9
-629.4
-610.2
-598.3
-581.8
-560.5
-546.5
-527.8
-508.3
-488.0
-466.9
-445.0
-422.2
-398.7
-374.3
-349.1
-323.0
TEMPERATURE
0
20
40
60
80
100
120
140
160
180
200
220
240
260
280
300
320
340
360
380
400

GALBEH(1)

STATIC D	VIBRATIONAL D	TOTAL D	TEMPERATURE
-1267.0	-515.0	-1882.0	0
-1251.6	-515.0	-1866.6	20
-1231.0	-515.0	-1846.0	40
-1205.3	-515.2	-1820.6	60
-1174.5	-517.1	-1791.6	80
-1138.6	-522.4	-1761.0	100
-1097.5	-532.6	-1730.1	120
-1051.3	-547.7	-1699.0	140
-1000.0	-567.4	-1667.4	160
-943.5	-591.2	-1634.7	180
-882.0	-719.3	-1600.3	200
-815.3	-748.3	-1563.6	220
-743.5	-780.6	-1524.1	240
-666.5	-815.0	-1481.5	260
-584.4	-854.9	-1435.3	280
-497.2	-898.2	-1385.5	300
-404.9	-926.8	-1331.7	320
-307.5	-966.3	-1273.8	340
-204.9	-1006.6	-1211.6	360
-97.2	-1047.8	-1145.8	380
15.6	-1089.5	-1073.9	400

GALBEH(2)

STATIC D	VIBRATIONAL D	TOTAL D	TEMPERATURE
-966.4	-363.6	-1330.0	0
-955.3	-363.6	-1318.9	20
-941.7	-363.7	-1305.3	40
-925.7	-364.8	-1289.5	60
-907.3	-367.8	-1272.1	80
-886.5	-373.6	-1254.1	100
-863.2	-382.4	-1236.9	120
-837.5	-393.8	-1219.9	140
-809.4	-407.6	-1203.2	160
-778.9	-423.4	-1186.5	180
-745.9	-440.8	-1169.3	200
-710.5	-459.7	-1151.4	220
-672.7	-479.7	-1132.4	240
-632.4	-500.7	-1112.2	260
-589.9	-522.5	-1090.5	280
-544.7	-545.1	-1067.2	300
-497.1	-568.2	-1042.2	320
-447.2	-591.8	-1015.3	340
-394.8	-615.8	-986.6	360
-339.9	-640.3	-955.9	380
-282.7		-923.9	400

GSASEH(1)

STATIC D	VIBRATIONAL D	TOTAL D	TEMPERATURE
-1202.0	-536.0	-1738.0	0
-1188.2	-536.0	-1724.2	20
-1170.2	-536.2	-1706.4	40
-1147.1	-537.8	-1683.3	60
-1119.9	-542.4	-1657.2	80
-1088.9	-551.2	-1629.3	100
-1049.7	-564.3	-1600.9	120
-1007.7	-581.4	-1572.3	140
-961.6	-602.0	-1542.4	160
-910.6	-625.6	-1511.6	180
-853.9	-651.6	-1479.8	200
-792.6	-679.7	-1448.2	220
-726.9	-709.5	-1416.6	240
-656.6		-1386.1	260

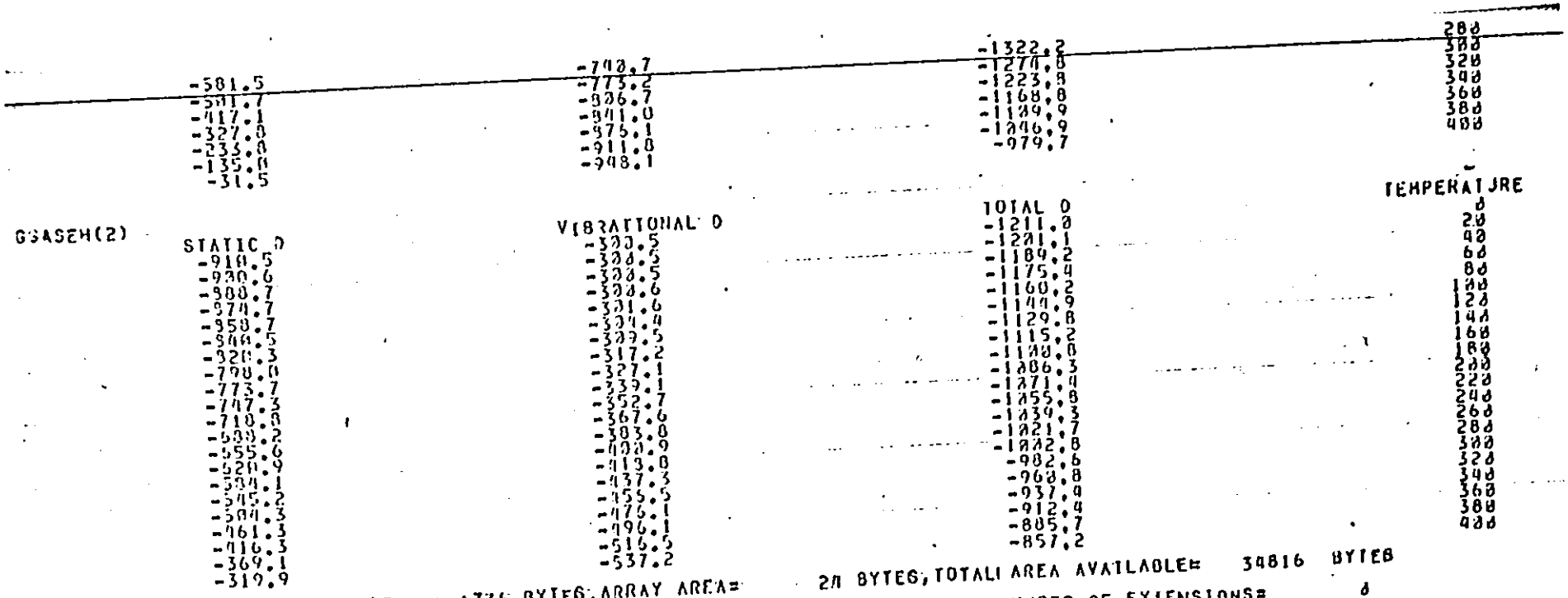

				TEMPERATURE
				0
				20
				40
				60
				80
				100
				120
				140
				160
				180
				200
				220
				240
				260
				280
				300
				320
				340
				360
				380
				400
-581.5	-798.7	-1322.2		
-511.7	-773.2	-1270.8		
-417.1	-806.7	-1223.8		
-327.8	-941.0	-1168.8		
-233.8	-976.1	-1149.9		
-135.8	-911.8	-1096.9		
-31.5	-948.1	-979.7		
GGASEH(2)				
	STATIC D	VIBRATIONAL D	TOTAL D	
	-910.5	-300.5	-1211.0	
	-930.6	-300.5	-1231.1	
	-880.7	-300.5	-1189.2	
	-874.7	-300.6	-1175.4	
	-858.7	-301.6	-1160.2	
	-808.5	-301.4	-1111.9	
	-820.3	-309.5	-1129.8	
	-798.0	-317.2	-1115.2	
	-773.7	-327.1	-1100.8	
	-747.3	-339.1	-1086.3	
	-718.8	-352.7	-1071.4	
	-688.2	-367.6	-1055.8	
	-655.6	-383.8	-1039.3	
	-620.9	-400.9	-1021.7	
	-584.1	-418.8	-1002.8	
	-545.2	-437.3	-982.6	
	-504.3	-456.5	-960.8	
	-461.3	-476.1	-937.4	
	-416.3	-496.1	-912.4	
	-369.1	-516.5	-885.7	
	-319.9	-537.2	-857.2	

CORE USAGE: OBJECT CODE= 1736 BYTES, ARRAY AREA= 28 BYTES, TOTAL AREA AVAILABLE= 34816 BYTES

DIAGNOSTICS NUMBER OF ERRORS= 0, NUMBER OF WARNINGS= 0, NUMBER OF EXTENSIONS= 0

COMPILE TIME= 0.19 SEC, EXECUTION TIME= 1.97 SEC, WATFIV - JUL 1973 V1L0 14.41.59 THURSDAY 23 SEP 76

RUN IN HSC SEPT 23, 1976

COST FOR THIS PROGRAM IS $ 1.07

APPENDIX B

Conversion factors from the units used in this work to the SI system of units.

1 $\mathring{A}$	=	0.1 nm
1 a.u.	=	52.917715 pm
1 a.m.u.	=	1.660531×10^{-27} kg
1 b	=	10^{-28} m^2
1 cm^{-1}	=	1.98648×10^{-23} J
1 e.V.	=	0.16021917 aJ
1 in.	=	2.54 cm
1 G	=	0.1 mT
1 kG	=	1 dT

REFERENCES

1. A.G. Danilov and A. Manoogian, Phys. Rev. B6, 4103 (1972).
2. A. Manoogian and B. Auger, Can. J. Phys. 52, 1731 (1974).
3. K. Pack and A. Manoogian, Can. J. Phys. 54, 217 (1976).
4. O.G. Holmes and D.S. McClure, J. Chem. Phys. 26, 1686 (1957).
5. R.L. Carlin and I.M. Walker, J. Chem. Phys. 46, 3921 (1967).
6. C.J. Ballhausen, Introduction to Ligand Field Theory (McGraw-Hill, New York, 1962).
7. W.M. Walsh, Phys. Rev. 114, 1473 (1959).
8. W.M. Walsh, Phys. Rev. 114, 1485 (1959).
9. W.M. Walsh, J. Jeener, and N. Bloembergen, Phys. Rev. 139, A1338 (1965).
10. K.N. Shrivastava, Phys. Rev. 187, 446 (1969).
11. K.N. Shrivastava, Chem. Phys. Lett. 6, 545 (1970).
12. K.N. Shrivastava, Phys. Lett. A42, 385 (1973).
13. K.N. Shrivastava, Chem. Phys. Lett. 22, 622 (1973).
14. R.L. Hartman, J.S. Bennett and J.G. Castle, Jr., Phys. Rev. 5, 1946 (1970).
15. S. Geller and D.P. Booth, Z. Kristallogr. 111, 117 (1959).
16. B.J.B. Schein, E.C. Lingafelter and J.M. Stewart, J. Chem. Phys. 47, 5183 (1967).

17. B.J.B. Schein and E.C. Lingafelter, J. Chem. Phys. 47, 5190 (1967).

18. E.C. Lingafelter, P.L. Orioli, B.J.B. Schein, and J.M. Stewart, Acta Cryst. 20, 451 (1966).

19. A.N. Holden, B.T. Matthais, W.J. Mertz, and J.P. Remeika, Phys. Rev. 98, 546 (1955).

20. E.A. Wood, Acta Cryst. 9, 618 (1956).

21. A.N. Holden, W.J. Mertz, J.P. Remeika, and B.T. Matthais, Phys. Rev. 101, 962 (1956).

22. G.S. Bogle, J.R. Gabriel and G.A. Bottomley, Trans. Faraday Soc. 53, 1058 (1957).

23. J.M. Daniels and H. Wesemeyer, Can. J. Phys. 36, 144 (1958).

24. G. Burns, Phys. Rev. 123, 1634 (1961).

25. R.W. Schwartz and R.L. Carlin, J. Am. Chem. Soc. 92, 6763 (1970).

26. H. Lipson and C.A. Beevers, Proc. R. Soc. (London) A148, 664 (1935).

27. H. Lipson, Proc. R. Soc. (London) A151, 347 (1935).

28. H.P. Klug and G.L. Kieffer, J. Am. Chem. Soc. 62, 2071 (1940).

29. A.C. Larson and D.T. Cromer, Acta Cryst. 22, 793 (1967).

30. B. Bleaney, Proc. R. Soc. (London) A204, 203 (1950).

31. R. Chicault, XVIII Congress Ampere, 202 (1973).

32. D.E. O'Reilly and T. Tsang, Phys. Rev. 157, 417 (1967).

33. G. Burns, J. Chem. Phys. 32, 1585 (1960).

34. K.R. Andress and C. Carpenter, Z. Kristallogr. 87, 446 (1934).

35. D.R. Buchanan and P.M. Harris, Acta. Cryst. B24, 954 (1968).

36. G. Feher, Phys. Rev. 103, 500 (1956).

37. G. Feher and E.A. Gere, Phys. Rev. 103, 834 (1956).

38. W. Low, Paramagnetic Resonance in Solids (Academic Press, New York, 1960).

39. M.H.L. Pryce, Proc. Phys. Soc. (London) A63, 25 (1950).

40. A. Abragam and M.H.L. Pryce, Proc. R. Soc. (London) A205, 135 (1951).

41. N. Laurance and J. Lambe, Phys. Rev. 132, 1026 (1963).

42. K.N. Shrivastava, Phys. Lett. 31A, 454 (1970).

43. K.N. Shrivastava, Phys. Lett. 42A, 385 (1973).

44. B.R. McGarvey, J. Chem. Phys. 40, 809 (1964).

45. B.R. McGarvey, J. Chem. Phys. 41, 3743 (1964).

46. R. Bershon, J. Chem. Phys. 29, 326 (1958).

47. R.M. Sternheimer (private communication).

48. S. Geschwind, Hyperfine Interactions, edited by A.J. Freeman and R.B. Frankel (Academic, New York, 1967).

49. J.H. Van Vleck, Phys. Rev. 57, 426 (1940).

50. A.G. Danilov, Ph.D. Thesis, University of Ottawa (1971).

51. B. Milsch and W. Brunner, Colloque Ampere, Bucharest, p. 748 (1970).

52. C.A. Bates and P.B. Sczaniecki, XVII Congress Ampere, p. 527 (1973).

53. D.M.S. Bagguley and J.H.E. Griffiths, Proc. R. Soc. (London) A204, 188 (1950).

54. R.W. Terhune, J. Lambe, C. Kikuchi, and J. Baker, Phys. Rev. 123, 1265 (1961).

55. M. Rubinstein, G.H. Strauss, and J.J. Krebs, Phys. Lett. 12, 302 (1964).

56. J.O. Artman, Phys. Rev. 143, 541 (1966).

57. J.M. Baker, Proc. Phys. Soc. B69, 633 (1956).

58. R.M. Sternheimer (Private communication).